THE UNIVERSITY *of* EDINBURGH

POPULATION CODING IN PRIMARY MOTOR CORTEX

Premchand Brian

Doctor of Philosophy

Centre for Discovery Brain Sciences

Edinburgh Medical School: Biomedical Sciences

University of Edinburgh

2018

Premchand Brian:

Population coding in primary motor cortex

Doctor of Philosophy, 2018

Supervisors:

Prof. Ian Duguid

Dr. Nathalie Rochefort

Abstract

The mammalian primary motor cortex (M1) is positioned upstream of spinal motor circuits, and its output drives movement execution. While traditional electrophysiological techniques have developed our understanding of neural coding in motor cortex, they lack the ability to resolve fine-grained spatiotemporal patterns of neuronal ensemble activity. Here, we investigated how two diametrically opposite movements are encoded in the main output layer of M1 – Layer 5B (L5B) - by performing *in vivo* population calcium imaging while mice repeatedly performed a cued forelimb push-pull task.

A prerequisite for recording the neural correlates of behaviour in M1 L5B is knowing the exact depth of L5B from the pial surface and development of a robust behavioural paradigm to assess cortical control of skilled movements. To achieve these aims, we first defined the upper boundary of L5B in forelimb M1 ($M1_{FL}$) of male C57BL/6JCrl mice by using conventional retrograde tracing techniques and post hoc histological analysis. Second, we designed and implemented a novel cued forelimb behavioural paradigm where water-controlled mice were trained to alternate push and pull lever actions upon presentation of a 6 kHz auditory cue. Mice rapidly learned to perform the task with ~84% of mice achieving 'expert' status within 10 ± 3 days (SD).

To characterise the spatiotemporal activity patterns of L5B neurons in $M1_{FL}$ during task engagement, we expressed GCaMP6s in deep layer neurons and recorded population activity during bidirectional movements. We found that subpopulations of L5B neurons displayed task-related fluorescence changes consistent with roles in motor control. Moreover, ~20% of L5B neurons displayed differences in peak fluorescence changes during movements in one direction over the other (i.e. push trial vs pull trial). To quantify these changes, we created a dissimilarity index (DI) to investigate how neuronal DI was distributed across our imaging fields of view.

Parallel calcium imaging experiments were conducted in layer 2/3 (L2/3) of $M1_{FL}$ which provides significant feedforward excitatory input to L5B. We found that ~20% of L2/3 neurons also exhibited significant differences between push- and pull-related activity,

indicating that direction-specific motor activity is not only present in L5B but is present in upper layers of M1.

To investigate if we could decode movement direction from population activity recorded during task execution, we trained linear support vector machines (LSVMs) using the movement-related population data, then evaluated them via *k*-fold cross-validation. We found that LSVMs could successfully decode action type (i.e. push or pull trial) when applied to both L5B and L2/3 fields of view, validating our hypothesis that different movement types are encoded at the level of $M1_{FL}$ population activity. Moreover, LSVMs trained using a subpopulation of neurons with significant DIs were able to decode movement direction more effectively, indicating that movement type can be readout from the activity of relatively few neurons in $M1_{FL}$.

In summary, we performed population calcium imaging in mouse $M1_{FL}$, and found subpopulations of neurons, both in L2/3 and L5B, which encode movement direction by differentially modulating their activity levels during the execution of diametrically opposing forelimb movements. This activity could be successfully decoded to predict movement direction via machine learning, suggesting that mice are suitable models for studying the decoding of directional motor control.

Lay summary

Sir Charles Sherrington described motor neurons as the “final common pathway”, because nearly all neural processing in the brain must converge into motor output before it can influence the physical world. The motor system of the brain lies upstream of lower motor neurons in the spinal cord, and understanding how it encodes movement (that is, how the activity patterns of its neurons relates to movement) has many real-world implications, from understanding and assisting the recovery of stroke patients, to developing brain-computer interfaces.

For the purposes of this thesis we focused on the primary motor cortex (M1) which is a part of the cerebral cortex that sends motor output directly to the spinal cord in addition to other motor-related brain regions. The cortex is divided into layers 1 to 6, and this study focused on layer 5B (L5B), since it is the main source of M1 output. Neurons in L5B can project directly to lower motor neurons (in humans and other higher order mammals), and to local spinal motor circuits (in all mammals including mice), thus L5B constitutes an important input to the “final common pathway” of movement.

The main question we sought to address was whether individual movements are differentially represented in L5B of M1, and if so, how each movement is encoded. Therefore, we designed a forelimb motor task for mice which required them to perform two diametrically opposed movements: pushing and pulling of a lever. To ensure that their posture and positioning with respect to the lever was consistent, and to facilitate imaging of neural activity, mice were surgically implanted with a lightweight headplate, and head-restrained during task execution. Mice were placed on a water control paradigm and trained to perform repeated sequences of push and pull movements in response to an auditory cue.

We sought to characterise the activity of L5B neurons in M1 as mice performed the task and to achieve this we employed high-resolution 2-photon population calcium imaging. This entailed labelling neurons in M1 with a genetically-encoded calcium indicating protein, GCaMP6s, which becomes more fluorescent when calcium levels within neurons increases. Since calcium levels increase with neuronal activity, changes in fluorescence can be used as a proxy for changes in neuronal activity. We recorded population activity in forelimb M1

($M1_{FL}$), the part of M1 that drives forelimb movements, as mice performed push and pull trials. The majority of neurons in L5B displayed task-related fluorescence changes, and ~20% displayed significantly higher fluorescence changes when mice moved in one of the two movement directions (i.e. push or pull). We also performed calcium imaging in layer 2/3 (L2/3), an important source of neural input to L5B, and similarly found that ~20% of L2/3 neurons exhibited direction-specific patterns of activity, indicating that such specificity is not only present in L5B but is measurable further upstream as well.

We then trained linear support vector machines (LSVMs), a type of algorithm used in machine learning, to decode movement direction from population activity. If population activity can be decoded to predict movement direction, it implies that direction-specific information was encoded in the population activity. The LSVMs were successfully able to decode movement direction in both L2/3 and L5B. Moreover, we were able to successfully train LSVMs using only a subset of neurons in each population, indicating that relatively few neurons from each population sample are required to decode the action type.

In summary, we recorded the activity of neurons in mouse $M1_{FL}$, and found groups of neurons, both in L2/3 and L5B, which encode movement direction by modulating their activity levels during the execution of forelimb movements. Movement direction could be decoded by analysing neuronal activity with machine learning techniques, suggesting that mice are suitable models for studying the decoding of directional motor control.

Acknowledgements

I would like to express my sincerest gratitude to all those who made the completion of this thesis possible.

First and foremost, I would like to thank my supervisor Prof Ian Duguid, who has patiently and wisely guided me throughout my PhD programme. He has consistently encouraged me through my project despite the many setbacks we encountered, and I can only hope to one day attain the clarity of scientific thought he possesses.

I would also like to thank the rest of my thesis committee, Dr Nathalie Rochefort and Mike Ludwig, for their valuable advice and comments.

Many thanks to my labmates at the Duguid Lab and Rochefort Lab, especially Dr Julian Ammer, Dr Stephen Currie, Dr Joshua Dacre, Dr Julia Schiemann, Dr Janelle Pakan, and Dr Evelyn Dylda, for their considerable technical expertise and irreplaceable camaraderie. And to our collaborators at Imperial College London, Dr Aldo Faisal and Wu Yufei, for significantly advancing our understanding of neural decoding.

I am very grateful to my family and friends who have provided indispensable love and support over the years, and to my patron, the Agency for Science, Technology and Research (A*STAR), which granted me a scholarship that has funded my tertiary education for many years.

Last but not least, I would like to thank my loving and beautiful wife, Xu Zhuo'er. This step in my journey as a scientist has been arduous and trying at times, but even on the worst of days, when I think of your smile my troubles melt away.

Declaration

I declare that this thesis was composed by myself, that the work contained herein is my own except where explicitly stated otherwise in the text, and that this work has not been submitted for any other degree or professional qualification except as specified.

Edinburgh, 2018

Premchand Brian, November 19th, 2018

Abbreviations

AAV	Adeno-associated virus
AIC	Akaike information criterion
ALM	Anterior lateral motor cortex
ANOVA	Analysis of variance
CFA	Caudal forelimb region
CT	Corticothalamic
d.f.	Degrees of freedom
DI	Dissimilarity index
DNA	Deoxyribonucleic acid
FISSA	Fast Image Signal Separation Analysis
FOV	Field of view
GECI	Genetically-encoded calcium indicator
GFP	Green fluorescent protein
HEPES	4-(2-hydroxyethyl)-1-piperazineethanesulfonic acid
ICMS	Intra-cortical microstimulation
IT	Intratelencephalic
L2/3	Layer 2/3
L4	Layer 4
L5A	Layer 5A
L5B	Layer 5B
LME	Linear mixed-effects model
LOTOS	Low-power temporal oversampling
LSVM	Linear support vector machine
M1	Primary motor cortex
$M1_{FL}$	Forelimb region of M1
M2	Secondary motor cortex

MI	Motion index
PBS	Phosphate-buffered saline
PFA	Paraformaldehyde
PMT	Photomultiplier tube
PT	Pyramidal tract
RFA	Rostral forelimb region
RFP	Red fluorescent protein
ROI	Region of interest
SIMA	Sequential IMage Analysis
SD	Standard deviation
s.e.m.	Standard error of the mean
$t_{1/2}$	Half-life
V1	Primary visual cortex

Contents

Chapter 1: General introduction

All man can do is to move things, and his muscular contraction is his sole means thereto. (Sherrington, 1949)

For mammals such as humans, nearly all interactions between an organism and its environment are executed via the motor system. We walk, eat, speak, manipulate tools, and write theses using our motor systems, and it is quite possible that it is the development of tool-making and language (i.e. advanced motor skills) that drove the evolution of early hominins into modern humans (Ko, 2016; Morgan et al., 2015). Understanding how the motor system controls movement and generates behaviour has been vital in the treatment of disorders such as Parkinson's disease, and the development of brain-computer interfaces. In addition, medical interventions that improve the motor system can potentially lead to enormous benefits in terms of quality of life. However, despite over a century of research, the means by which the motor system encodes movement still remains largely unknown. This doctoral research project aims to investigate how different movements are represented in the neuronal population activity of primary motor cortex in mice.

1.1 Neuroanatomy of the primary motor cortex (M1)

The mammalian motor system consists of many interconnected areas including the motor cortex, motor thalamus, brainstem nuclei, and spinal circuits (Figure 1.1), which converge on the "final common pathway" of motor neurons (Lawrence and Kuypers, 1968; Otten, 2001; Sherrington, 1906). This thesis focuses on the primary motor cortex (M1), and its population activity during the generation of skilled movements.

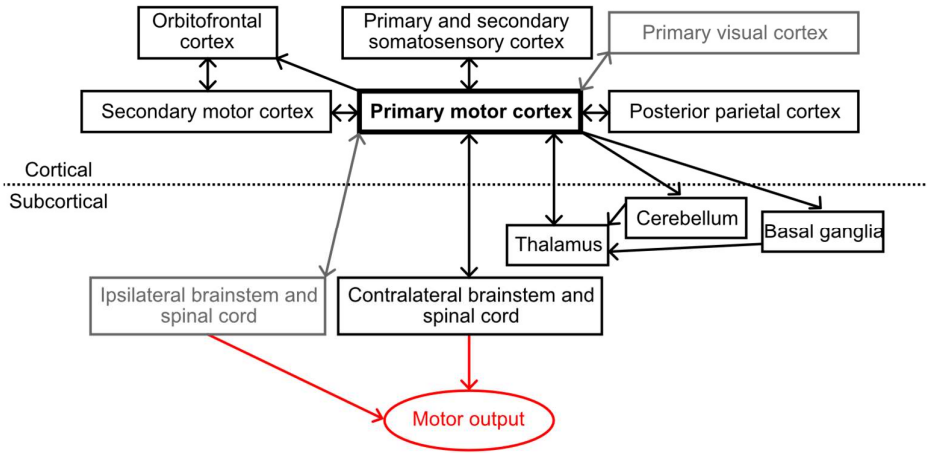

Figure 1.1: Major cortical and subcortical inputs to M1. Strong connections are depicted in black, while weak connections are depicted in grey. The primary motor cortex has strong recurrent connections within itself, and with contralateral primary motor cortex. The final motor output is depicted in red. (Adapted from Watson et al., 2012).

M1 is a key node of the central nervous system, connected in a manner that allows it to receive multiple sensory modalities and integrate them to generate appropriate motor responses (Hatsopoulos and Suminski, 2011). Like other cortical regions, it is organised into histologically and electrophysiologically distinct layers, with extracortical output arising from the deeper layers. However, unlike most other regions of cortex, M1 lacks a distinct layer 4 (L4), also known as the internal granular layer (Beul and Hilgetag, 2015; Brodmann, 2006; Shepherd, 2009). This is why M1 has also been named “agranular cortex”, as opposed to granular cortex, which contains a distinct L4 (Figure 1.2).

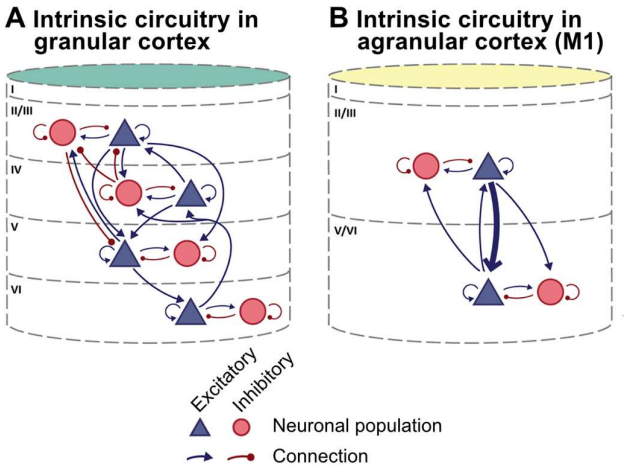

*Figure 1.2: Intrinsic circuitry in **A)** granular and **B)** agranular cortex. The strongest interlaminar connection in M1, L2/3 → L5, is depicted as a thick blue arrow. Adapted from Beul and Hilgetag (2015).*

In sensory cortical areas, the "canonical" microcircuit entails thalamic input arriving in L4, which has strong projections to L2/3, which in turn project to L5, where extracortical projections arise (Beul and Hilgetag, 2015; Douglas et al., 1989; Shepherd, 2009). Lacking a distinct L4, the dominant interlaminar connection in M1 is L2/3 → L5 (Shepherd, 2009). Nonetheless, M1 does receive thalamic input, and more recent evidence suggests that there may be a thin L4 between L2/3 and L5A, which receives dense projections from motor thalamus and may play a similar role as L4 in granular cortex, albeit with weaker L4 → L2/3 connections (Dacre, 2016; Yamawaki et al., 2014).

In addition to inhibitory interneurons which exist in all cortical layers, M1 contains three major classes of excitatory neurons: corticothalamic (CT), intratelencephalic (IT), and pyramidal tract (PT) neurons (Hattox and Nelson, 2007; Shepherd, 2014; Shepherd and Rowe, 2017). IT neurons send projections within the cerebrum, and are present in layers 2-6. PT neurons are present exclusively in L5B, and have a variety of projection targets including the thalamus, pons, medulla, and spinal cord. CT neurons are present in lower L5B and L6, and project to the thalamus. While there are recurrent extracortical circuits that connect all three neuronal classes, within M1 there is a hierarchal connection pattern of IT → PT → CT, with each neuronal class projecting within the same class and to the next class (Shepherd and Rowe, 2017; Yamawaki et al., 2014). Since this thesis is focused on recording $M1_{FL}$ activity in L2/3 and upper L5B, we will not discuss CT neurons further. The excitatory neurons recorded in L2/3 are exclusively IT neurons, while those in L5B are a mixture of IT and PT neurons, with the two classes contributing to 44% and 56% of the L5B excitatory population, respectively (Schiemann et al., 2015).

1.2 The role of M1 in skilled behaviour

What is the role of M1 in the generation and control of motor output? In 1870, Fritsch and Hitzig found that electrically simulating certain regions of a dog's cerebrum, now defined as M1, resulted in the generation of discrete movements (Fritsch and Hitzig, 2009). Now, it is

broadly accepted that neural activity in M1 is associated with almost all motor behaviour, and that it undergoes functional reorganisation as animals learn new motor task/skills (Classen et al., 1998; Gandolfo et al., 2000; Rioult-Pedotti et al., 1998; Wang et al., 2011).

For this thesis, we have chosen the mouse as a model to investigate cortical motor control for a multitude of reasons. Firstly, mice can be bred quickly and inexpensively, trained relatively easily, can be stably head-restrained for *in vivo* electrophysiological or imaging protocols, and their smooth and relatively thin cerebral cortices enables population calcium imaging (Dombeck et al., 2007; Kim et al., 2016; Ohki et al., 2005; Svoboda et al., 1997). Secondly, mice are provide genetic tractability, and transgenic mice (from modified lines and/or after postnatal viral transformation) have been successfully used to probe neural circuit function *in vivo* (Doyle et al., 2012; Passini et al., 2004).

However, it should be noted that M1 lesions in humans, non-human primates and mice produce different effects, suggesting that M1 may play different roles in motor control across mammalian species. In human stroke patients, damage to M1 can result in gross motor deficits up to and including paralysis contralateral to the stroke, a condition known as hemiplegia (Hallett, 2001). This suggests that M1 is necessary for all, or nearly all, motor output in humans. In contrast, nonhuman primates often display gross motor deficits such as hemiplegia shortly after M1 lesions are made, but after rehabilitation, can regain much of their original motor capabilities (Darling et al., 2011; Lashley, 1924; Ogden and Franz, 1917). In rodents, M1 lesions do not lead to outright paralysis: affected animals instead demonstrate transient mild ataxia, but display subtle and prolonged motor deficits, such as gait impairment, increased foot slips when locomoting on a grid, and difficulty grasping food pellets (Castro, 1972; Neumann et al., 2009; Stroemer et al., 1995). Where then is the common ground between M1 function in mice and higher order mammals?

One possible explanation is that cortical lesions in mice can lead to increased plasticity and other compensatory mechanisms, and it is possible that the deficits observed after lesioning M1 have been attenuated by homeostatic compensatory mechanisms during recovery (Nudo, 2013; Otchy et al., 2015). Mice have relatively well-developed extrapyramidal tracts compared to humans, and these may adopt corticospinal functions in response to an M1 lesion (Takase et al., 2017; Watson and Harrison, 2012). However, there are aspects of mouse behaviour that do not fully recover after M1 lesions: the acquisition of skilled, or dexterous, motor behaviour, defined as “task-specific learned motor sequences” (Kawai et al., 2015).

Mice with M1 lesions exhibited impaired learning of a cued lever-press task (Peters et al., 2014), and displayed deficits in the learning but not execution of a non-dextrous timed lever-press task (Kawai et al., 2015). In addition, transient disruption of M1 activity in rodents results in impaired motor performance, where optogenetic inhibition of M1 output significantly impacts on skilled pellet-reaching, directional joystick control and cued lever-pressing (Guo et al., 2015; Morandell and Huber, 2017; Peters et al., 2014). Indeed, transient M1 inactivation can cause more disruption to motor output than a chronic M1 lesion in the same region, suggesting that lesion studies in rodent M1 may underestimate its necessity in generating movements (Otchy et al., 2015). In sum, while mouse M1 is not as vital as higher order mammalian M1 for the production of gross motor output, M1 performs a somewhat similar role in the preparation and execution skilled movements across both species. Given the stated advantages of using mice I am of the opinion that is serves as a robust model for investigating cortical motor control.

1.3 Population neural coding in $M1_{FL}$

This thesis will focus on studying neural population coding in $M1_{FL}$. What is the meaning of the term 'neural coding'? Fundamentally, the mammalian central nervous system receives information from sensory inputs, and provides outputs via the motor system. Ignoring glia for the sake of simplicity (Möller et al., 2007), the information corresponding to these inputs and outputs is transmitted by neurons in the form of action potentials. A population of neurons may represent information in terms of their firing rate (temporal code), the time at which their firing rate changes (temporal code), which neuron in the population is firing at a given time (local code), which neurons are firing at any given time (population code) or any combination of the above (Averbeck et al., 2006; Borst and Theunissen, 1999). This representation of information in terms of neuron firing patterns is known as neural encoding.

The reverse of neural encoding is extracting the represented information from neuronal firing patterns, that is, neural decoding. However, the term "neural decoding" can have two rather different meanings. If a neuron or population of neurons encodes information relevant to a behaviour (be it a stimulus or a motor response), "decoding" can refer to 1) how downstream neurons process those activity patterns, or 2) how human neuroscientists correlate activity patterns to the known information (Borst and Theunissen, 1999; Knierim, 2014). While these

two concepts are linked, they are not identical in mammals. For animals with simple nervous systems like *C. elegans* and *Aplysia*, individual neurons and synapses can be counted and recorded, so a physiological recording may reveal both decoding types. However, in the mammalian motor system, which contains a far greater number of neurons and synapses, it has thus far been impossible to fully map information transfer and storage in and across different brain areas. For example, a typical mouse cortical neuron generates approximately 8200 synapses within cortex alone, and this figure is on the same order of magnitude as the number of neurons in the entire central nervous system of an *Aplysia* (Moroz, 2011; Schüz and Palm, 1989). Therefore, it is currently beyond our reach to simultaneously record from a given mammalian neuronal population and all its downstream targets in order to know how the downstream targets responds to activity patterns in that neuronal population. Instead, we are left with the second definition of "decoding", which is to find correlations between neuronal activity and features of incoming stimuli or outgoing motor behaviour. For example, features of visual stimuli have been successfully decoded from population activity recorded from visual cortex in a variety of mammalian species (Benucci et al., 2009; Berens et al., 2012; Montijn et al., 2015).

When it comes to motor systems as opposed to sensory systems, even the search for correlations suffers from additional complications. The scientific method is rooted in repeatable observations and experimentations, and the neural codes underpinning many sensory modalities and reflex arcs have been elucidated by repeatedly exposing laboratory animals to precisely tuned stimuli, while simultaneously recording neuronal activity. This method has been successfully employed in many neural circuits, from Kandel's studies on sensitisation and classical conditioning in *Aplysia*, to Hubel and Wiesel's work on the cortical coding of visual gratings in cats (Hubel and Wiesel, 1959; Kandel and Tauc, 1965).

However, when it comes to decoding motor systems, neuronal population activity must be correlated with self-generated physical movements, not with a stimulus which can be repeatedly delivered to the experimental subject in a controlled manner. Whether in trained laboratory animals or human subjects, such motor outputs are never perfectly repeated across trials (Bernshteĭn, 1967). Even apparently simple movements such as moving a limb from one point to another generates considerable trial-to-trial variability (Figure 1.3), in terms of movement path, timing and velocity (Churchland et al., 2006; Georgopoulos et al., 1982). This inconsistency can be reduced with training, but never completely eliminated.

Therefore, studies which attempt to decode the mammalian motor system have to embrace not only the variability inherent in neural activity, but also the variability in behaviour.

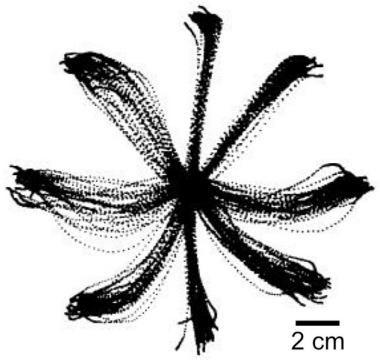

Figure 1.3: Variable trajectories recorded during a primate directional reaching task. A non-human primate was trained to reach for one of 8 targets during each trial in this directional reaching task. The targets were positioned on a plane and arranged in a circle, separated by 22.5°. Each black trace represents one trial, with 30 trials plotted for each target. Even though this non-human primate was well-trained, movement trajectories were variable between trials. (Adapted from Georgopoulos et al., 1982.)

1.4 Directional preference and population vector coding

The mouse forelimb is an interesting model of motor control as it is homologous to the human forearm and hand, and like humans, mice use their forelimbs to perform dextrous motor tasks such as object manipulation and food consumption. Even though mice do not possess the fine motor control of humans, their forelimbs are relatively complex, each containing 21 muscles that can generate a wide range of physical movements (Watson et al., 2009). While approaching M1 neural coding in mice, it is useful to examine existing theories of M1 neural coding in other species.

According to Georgopoulos, neurons in the motor cortex display directional preference in terms of limb movements (Georgopoulos and Carpenter, 2015; Georgopoulos et al., 1982, 2007). During trials where the limb moves, neurons fire at higher frequencies if the movement is in their preferred direction, and at lower frequencies if the movement is in another direction. Such directional tuning is observed whether the movement targets are arranged in a plane or in three-dimensional space. This model of neuronal directional

preference also predicts that by observing a population of neurons with known preferred directions, a population vector can be obtained by summing their individual preferred directions weighted by their firing rates during movement, and that this population vector should reflect the direction of the movement (Georgopoulos and Carpenter, 2015; Schwartz, 1994). The population vector model been successfully used to predict movement direction in many studies involving humans, non-human primates, and even invertebrates (Collinger et al., 2013; Levi and Camhi, 2000; Lewis and Jr, 1998; Taylor et al., 2002).

Nonetheless, there are also opposing views, which state that the appearance of population vector coding is merely an epiphenomenon; a shadow cast on a cave wall by deeper, hitherto unseen forms of neural coding (Sanger, 1994; Scott, 2000). According to this argument, if there is any form of correlation between movement direction and neuronal activity in a sufficient population of neurons, and these correlations are approximately uniformly distributed in space, then it becomes a trivial mathematical result that neurons will coincidentally appear to have preferred directions and that there will be an appearance of population vector coding even if the neurons themselves are actually encoding something else (e.g. joint angles or muscle tension). Ultimately, the decision of whether one should decode population neuronal activity on the basis of population vector coding depends on what definition of "neural decoding" one uses, as described earlier. If using definition 2) (i.e. human neuroscientists correlating neural activity with known information) population vector coding is empirically correct. On the other hand, if one were to adhere to definition 1) (i.e. how downstream neurons interpret information from M1), then the population vector hypothesis is currently unfalsifiable, because it is not fully known how downstream neurons process feedforward information from M1. Regardless of whether the population vector model describes an epiphenomenon or not, it is capable of decoding motor output from population activity, so I will use it as the basis for predicting the presence of direction-specific activity in mouse $M1_{FL}$ during the execution of two diametrically opposed movements.

To investigate how such movements are encoded in $M1_{FL}$, I will employ a novel forelimb push/pull behavioural paradigm. According to the population vector coding hypothesis, diametrically opposed movements are expected to have the largest differences in population neuronal activity. By training mice to perform repeated push and pull trials, and performing neuronal population calcium imaging during behaviour, I aim to generate new insights into population coding in $M1_{FL}$.

This thesis is focused on studying the neural correlates of push and pull actions in layer 5B (L5B) of mouse $M1_{FL}$ by measuring population calcium dynamics using 2-photon imaging *in vivo* (Chapter 5). The first results chapter (Chapter 2) will describe the role L5B and how I determined its depth in mouse $M1_{FL}$. Next, I will detail the development and implementation of a cued forelimb lever push-pull task for mice (Chapter 3), and how some potential pitfalls of our experimental paradigm were identified and addressed (Chapter 4). Then, I will examine population activity in L2/3 of $M1_{FL}$, which provides an important feedforward input to L5B (Chapter 6). Finally, I will show how machine learning algorithms can be used to decode population activity in L2/3 and L5B to confirm the presence of direction-specific encoding of movement in M1 (Chapter 7).

This page was intentionally left blank.

Chapter 2: Defining layer 5B in mouse forelimb motor cortex

2.1 Introduction

The cortex of a mouse contains approximately 5 million cortical neurons, and of these about 500,000 reside in the 7 mm^3 which have been assigned as 'motor-related areas' (Herculano-Houzel et al., 2013). How is motor output during behaviour encoded in these half-million neurons? Even in a relatively small animal like a mouse, attempting to record from all these neurons and then make sense of the recordings would be a Sisyphean task. This thesis will instead primarily focus on a layer-specific subset of cortical neurons: layer 5B (L5B) of the primary forelimb motor cortex ($M1_{FL}$).

M1 is defined as the cortical area that is responsible for the planning, initiation, and control of skilled voluntary movement. In the context of mice, $M1_{FL}$ is the sub-region of M1 that drives forelimb movements. L5B was chosen because there is a general consensus that L5B is the only layer of M1 which contains corticospinal neurons which are a subset of pyramidal tract-type (PT-type) neurons that provide a direct pathway to the spinal cord to drive forelimb motor output (Anderson et al., 2010; Hooks et al., 2013; Oswald et al., 2013; Schiemann et al., 2015).

$M1_{FL}$ has been mapped in many studies by intracortical microstimulation (ICMS) (Puggioni, 2015; Tennant et al., 2011), and optogenetic stimulation experiments (Hira et al., 2013a) where stimuli are delivered to the cortical surface, and the areas that evoke forelimb movement are considered to be part of $M1_{FL}$. Such studies have revealed that $M1_{FL}$ is separated into two regions, a smaller rostral forelimb area (RFA) and a larger caudal forelimb area (CFA) (Hira et al., 2015; Morandell and Huber, 2017; Tennant et al., 2011). The RFA is thought to be homologous to primate premotor cortex, while the CFA is homologous to primate primary motor cortex (Hira et al., 2013b). In addition, L5B in the RFA projects to the CFA while L5B of the CFA does not project to the RFA, therefore the CFA lies downstream of the RFA in the mouse motor system, and it is easier to correlate CFA activity with the final motor output (Hira et al., 2013b). In order to record from the area of the cortex most proximal to motor output, and most relevant to understanding primate (including human)

primary motor cortex, this thesis will focus on the CFA of $M1_{FL}$. After examining measurements of $M1_{FL}$ boundaries in multiple published sources (Figure 2.1), we defined the coordinates of the centre of CFA to be 1.6 mm lateral and 0.6 mm rostral from bregma (Hira et al., 2013a; Schiemann et al., 2015; Tennant et al., 2011).

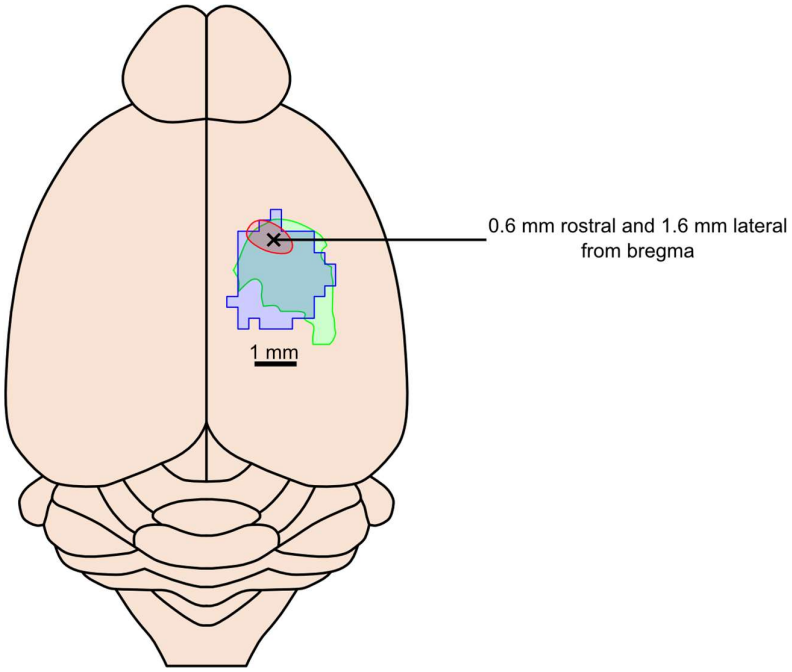

Figure 2.1: A *schematic of the mouse brain, with red (Puggioni, 2015), green (Tennant et al., 2011) and blue* (Hira et al., 2013a) *shaded areas indicating the boundaries of $M1_{FL}$ (caudal forelimb area only), as defined by ICMS (Puggioni, 2015), ICMS (Tennant et al., 2011) and optogenetic stimulation (Hira et al., 2013) experiments, respectively. From previous ICMS mapping experiments in the Duguid lab, we defined the centre of $M1_{FL}$ as 1.6 mm lateral 0.6 mm rostral from bregma (black cross), maximising the overlap from the 3 independent measurements of $M1_{FL}$ coordinates.*

But at what depth is L5B located in $M1_{FL}$? This is essential information necessary for ensuring that functional population imaging experiments are targeted to the correct cortical sublayer in $M1_{FL}$. The widely accepted definition of L5B is the layer in $M1_{FL}$ which contains PT-type neurons (Hay et al., 2011; Schiemann et al., 2015). However, this definition has recently been challenged with reports of the existence of corticospinal neurons in layer 5A (L5A), albeit at a lower density than observed in L5B (Masamizu et al., 2014). In terms of the depth of L5B from the pial surface, descriptions range from 570 µm to 620 µm (Hooks et al., 2011;

Schiemann et al., 2015), with one report stating that corticospinal cells can even be found at 519 µm (Masamizu et al., 2014). In contrast, some studies recognise that the depth of cortical layers can vary between mice and within each mouse depending on the location, and prefer to define layer depths in terms of a normalised ratio, where layer boundaries are defined as fractions of the distance between pia and white matter (Anderson et al., 2010; Hooks et al., 2013). While this method accounts for differences in overall brain size and is useful when using slide-mounted coronal sections or brain slices *in vitro*, this method cannot be used when performing 2-photon imaging *in vivo*, as the depth of cerebral white matter is not directly observable using conventional optics.

In summary, there appears to be no general consensus on the depth of L5B within $M1_{FL}$. Therefore, this chapter will describe how we employed retrograde tracing and histological methods to define the upper border of L5B in $M1_{FL}$ in the same breed, age group and sex of mice used for behavioural training (see Chapter 3) and 2-photon population calcium imaging experiments (see Chapters 4, 5 and 6).

2.2 Materials and methods

2.2.1 Overview

All experiments and procedures involving animals were approved by the University of Edinburgh local ethical review committee and performed under license from the UK Home Office in accordance with the Animal (Scientific Procedures) Act 1986. Male 8-12 week-old C57BL/6JCrl (20-30 g) were group housed (2-4 littermates per cage) with enrichment in the form of running wheels, cardboard tubes and/or boxes. Mice were maintained on a reversed 12:12 hour light:dark cycle. All experimental animals had *ad libitum* access to food and water. All surgical procedures were performed using aseptic techniques appropriate for mouse recovery surgery. In total, 16 mice were used for histological procedures.

2.2.2 Retrograde tracer injection surgery

We aimed to identify the upper boundary of L5B by labelling PT-type neurons and quantifying the depth from the pial surface at which they first appeared. Most neurons in M1 have axons confined to the telencephalon; only PT-type neurons project beyond, to areas including the thalamus, midbrain, brainstem, and spinal cord (Shepherd, 2013). To selectively label PT-type neurons, red RetroBeads (Lumafluor, Inc.) – fluorescent latex microspheres that are retrogradely transported by neurons but display minimal passive diffusion from the injection site (Katz et al., 1984; Schofield, 2001) – were injected into the pons. Injections were targeted to the ipsilateral pyramidal tract and pontine nuclei, so PT-type neurons which had axonal projections and synaptic terminals in that region would uptake the RetroBeads transporting them to the soma in forelimb motor cortex (Figure 2.2). By measuring how laminar fluorescence levels varied with depth in $M1_{FL}$, the upper boundary of L5B could be anatomically defined.

For pontine injections, mice were anaesthetised with 4% isoflurane (Abbott Pharmaceuticals) in air and their scalp shaved prior to being placed in a stereotactic frame (Just for Mouse Stereotaxic Instrument, Stoelting Co.). The isoflurane concentration was reduced to 1-2% for the remainder of surgery and adjusted as necessary to ensure an adequate depth of general anaesthesia (target respiration rate of approximately 2 breaths per second, no pedal pinch

reflex). After anaesthetic induction, viscous eye drops (Viscotears, Dr. Winzer Pharma GmbH, Germany or Bepanthen Ointment, Bepanthen) were applied to avoid corneal drying during surgery. The core temperature of mice was maintained at 37 °C throughout surgery using an isothermal heating blanket and rectal thermocouple probe. Saline (0.7 ml sterile Ringer's Solution, for perianaesthetic fluid support), an analgesic (4 mg/kg Carprofen, Carprieve, Norbrook Laboratories Limited), to reduce post-operative pain and inflammation) and an anti-inflammatory (0.2 mg/kg Dexamethasone, Rapidexon, Dechra Veterinary Products, to reduce cerebral oedema and inflammation) were injected subcutaneously.

Incisions were made in the scalp using a pair of sterilised #3 forceps (Dumont) and surgical scissors, and skin pushed aside to expose both lambda and bregma. A three-axis stereotactic micromanipulator was used to measure the spatial coordinates for bregma and lambda, and the orientation of the skull was adjusted until bregma and lambda lay on the same frontal and sagittal planes. To access the injection target at the pyramidal tract/pontine nuclei, a craniotomy was made directly above it. Assuming the distance between bregma and lambda was "BL" in millimetres, the injection target at the cranial surface was identified (BL*4.0/4.2)+0.3 mm caudal from bregma, and 0.4 mm lateral (coordinates from(Schiemann et al., 2015). A small craniotomy was produced directly at the target location with a handheld dental drill (0.5 mm diameter drill burr). During drilling, the craniotomy was periodically cleared using compressed air and washed with external saline solution (150 mM NaCl, 2.5 mM KCl, 10 mM HEPES, 1 mM $CaCl_2$, and 1 mM $MgCl_2$, adjusted to pH 7.3 with NaOH) to remove swarf and minimise thermal changes in the skull. The bone was thinned to the point at which the bone depressed slightly when gently pressed with a pair of #5 forceps (Dumont), then the central portion of bone ~200 µm wide was removed.

A calibrated injection pipette (pulled glass pipette, 5 µl Calibrated Micropipette, Drummond Scientific Company) was pre-filled with ~500 nl of tracer (undiluted red RetroBeads). The injection pipette was slowly driven vertically into the brain, until it made contact with the floor of the cranium. From that point, tracer injections were made at 4 sites, located 200 µm, 400 µm, 600µm, and 800 µm dorsal from the cranial floor. For each injection site, a Picospritzer III (Intracel) driven by compressed air was used to slowly inject 100 nl of the tracer (20-40 ms pulse duration, 10-40 psi, 2 s inter-pulse interval with a target flow rate of 40 nl/min). The pipette was left in situ for 5 mins at each injection site to ensure adequate stabilisation of pressure in the target zone before being slowly withdrawn. After the last

injection, the pipette was fully withdrawn and the injection craniotomy was sealed with a small volume of platinum-cure silicone (Body Double Fast Set, Smooth-On). The surgical incisions were then closed by bonding the cut skin edges together with Vetbond Tissue Adhesive (3M).

After surgery, mice were moved to a temperature-controlled recovery cage (air temperature set at 28 °C) until fully recovered from the effects of general anaesthesia, after which they were returned to the home cage. To reduce post-operative pain and inflammation, mice were subcutaneously injected with 4 mg/kg Carprofen (Carprieve, Norbrook Laboratories Limited) at 1, 2 and 3 days post-surgery.

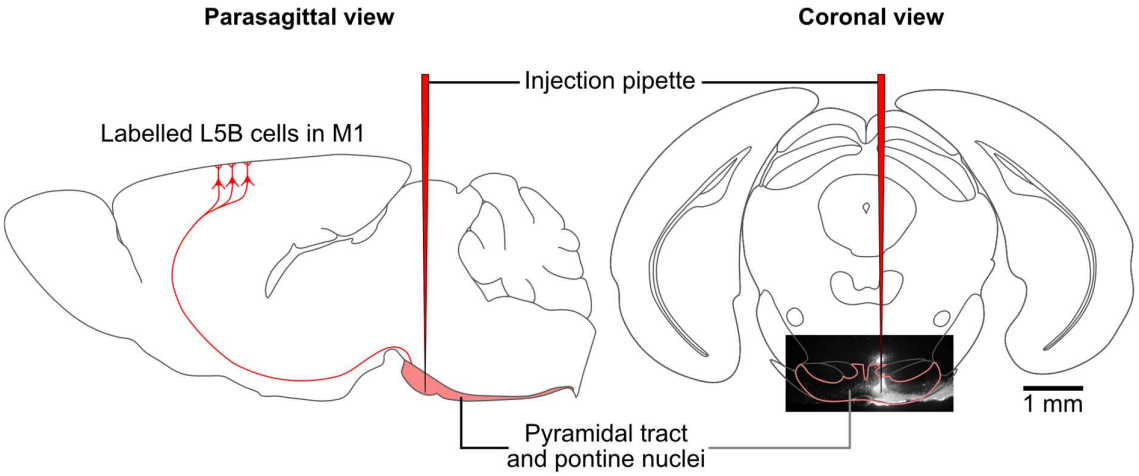

Figure 2.2: Overview of pontine injection strategy, as viewed from parasagittal (left) and coronal (right) planes. In both views the pyramidal tract and pontine nuclei are highlighted in light red, and the injection pipette in red. A monochrome fluorescent image of a pontine section from an injected mouse is underlaid on the coronal view, with the injected RetroBeads in the section appearing in white. Images adapted from the Paxinos Mouse Brain Atlas (Paxinos and Franklin, 2001).

2.2.3 Perfusion and histology

After at least 14 days post-injection, mice were terminally anaesthetised using an intraperitoneal injection of a ketamine/domitor mixture (75 mg/kg ketamine (Vetalar TMV, Zoetis), 1 mg/kg domitor (OrionPharma)). After testing for the lack of a pedal reflex, mice were transcardially perfused with 30 ml of phosphate-buffered saline (PBS, containing 64.6

mM Na_2HPO_4, 19.7 mM $NaH_2PO_4 \cdot H_2O$, 15.4 mM NaCl in distilled water, with pH adjusted to 7.4) followed by 30 ml of 4% paraformaldehyde (Paraformaldehyde, prilled, 95%, Sigma-Aldrich), dissolved in PBS and adjusted to pH 7.4. After extraction, each brain was post-fixed at 4 °C for 1-3 days in the same 4% PFA solution, then transferred to PBS solution until sectioning. Individual brains were sectioned into 60 µm coronal slices using a vibrating microtome (Leica VT1200 S, Leica Biosystems). Sections were directly mounted onto glass slides, briefly air-dried, covered with VECTASHIELD Antifade Mounting Medium (Vector Laboratories) and sealed with a glass coverslip.

Images were taken with a Leica DM R epifluorescence microscope and image analysis was performed using ImageJ and MATLAB. Given that $M1_{FL}$ is centred at approximately 0.6 mm rostral and 1.6 mm lateral from bregma (see Figure 2.1), images were taken from sections 0.3-0.9 mm rostral of bregma to cover the full extent of $M1_{FL}$ (Schiemann et al., 2015).

To obtain estimates of the depth of L5B in $M1_{FL}$, 3 coronal sections from each brain were imaged (0.54 mm, 0.6 mm and 0.66 mm rostral from bregma, i.e. central $M1_{FL}$ and a section immediately rostral and caudal). Regions of interest (ROIs) centred at 1.6 mm lateral from bregma were selected from each image, approximately 0.5 mm wide and at least 1.4 mm deep. ROIs were oriented such that the cortical surface was horizontal. Image processing in the form of brightness/contrast adjustments and background subtraction (rolling ball, 30 pixels wide at 1.28 µm/pixel) functions was performed to reduce the contribution of background autofluorescence. Each ROI was then divided into 25-µm-deep bins, and all the bins within a rectangle normalised to a value between 0 and 1, with 0 being the darkest bin and 1 being the brightest bin (Figure 2.3). The bin at 250 µm from the surface was taken as the baseline, as autofluorescence at the cortical surface was high. A paired Student's *t*-test was conducted between the baseline bin and each bin after it to determine the range of depths at which fluorescence was significantly higher than the baseline, indicating the presence of RetroBeads and therefore PT-type neurons in L5B.

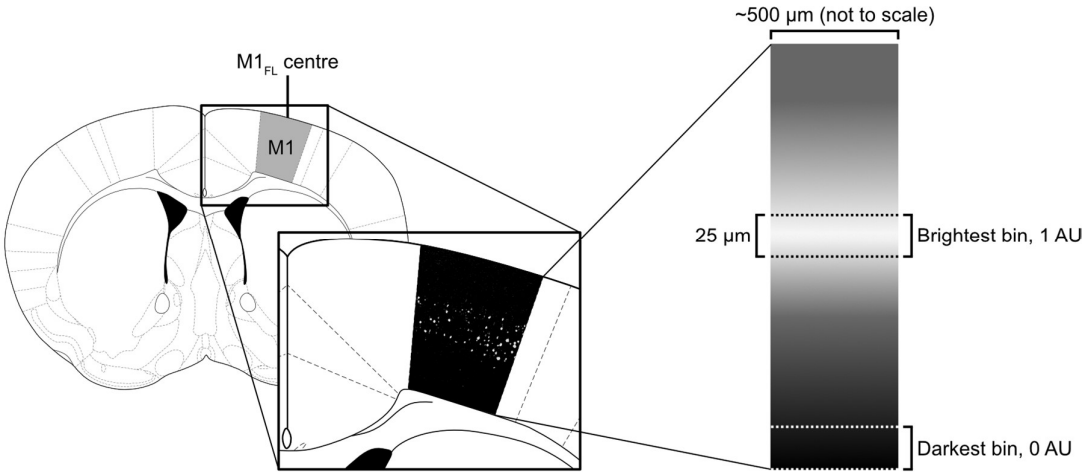

Figure 2.3: Quantification of RetroBeads labelling in $M1_{FL}$. Rectangular regions of $M1_{FL}$ were cropped from coronal images, and each region divided into 25-µm-deep bins, with the shallowest bin centred at 0 µm and the deepest bin at -1000 µm from the pial surface. The fluorescence of each bin was quantified by measuring mean pixel intensity. Fluorescence values for each section were then normalised to values between 0 (the darkest bin) and 1 (the brightest bin).

2.3 Results

2.3.1 Retrograde labelling in central $M1_{FL}$

Of the 16 brains sectioned, 5 displayed visible bands of tracer labelling in $M1_{FL}$, providing a total of 15 labelled sections for analysis. Many of the brains without visible bands of tracer had injections that were too rostromedial and failed to target the pyramidal tract, which lies more laterally as one goes rostral from the injection target. Mouse brains without visible $M1_{FL}$ labelling were excluded from further analysis.

After quantifying changes in fluorescence across different depths, it was found that fluorescence intensity significantly increased around 500 µm, with all bins from 500 µm to 975 µm displaying significantly increased fluorescence levels when compared to baseline (Figure 2.4). The laminar fluorescence changes depict the presence of PT-type neurons, providing us with anatomical coordinates of the upper and lower boundaries of L5B in $M1_{FL}$.

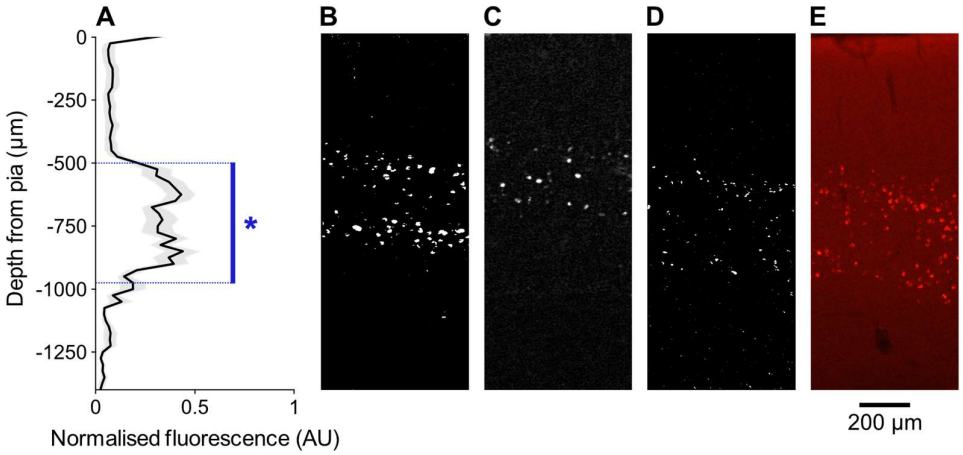

Figure 2.4: ***A)*** *The relationship between depth from pia and normalised fluorescence. The black line depicts the mean normalised fluorescence ± s.e.m. The blue vertical bar marked with (*) depicts bins that are significantly brighter than the baseline (paired* t*-test, d.f. = 28, p < 0.05).* ***B-D)*** *Representative images of the centre of* $M1_{FL}$ *from 3 different mice labelled with RetroBeads. The scale and position of the images match the y-axis in A. E) A raw image without rolling ball background subtraction, exhibiting the higher surface autoflorescence and uneven background.*

2.3.2 L5B depth at different cortical coordinates

In addition to characterising the depth profile of L5B it became apparent that the depth of L5B in $M1_{FL}$ changed with position on the cortical surface, both along the mediolateral and rostrocaudal axes. This is an important consideration given that the aim of this thesis was to record population calcium dynamics in the main output layer in $M1_{FL}$ – L5B. The maximum field of view (FOV) for our calcium imaging experiments in Chapter 4 is approximately 300 µm x 300 µm in diameter, so we first needed to measure whether the depth of L5B varied within a FOV.

In two tracer injected mice labelling was limited to the coronal section directly at the centre of $M1_{FL}$, but the remaining three mice displayed strong fluorescence labelling across multiple coronal sections, providing an opportunity to measure L5B depths at different rostrocaudal and mediolateral coordinates within $M1_{FL}$ (Figure 2.5). In each section, the depth of L5B was determined by manually measuring the distance from L5B (i.e. top-most neurons labelled with RetroBeads) to the cortical surface, at positions ranging from 1.3 mm to 1.9 mm lateral from the midline. These measurements were repeated in 5 coronal sections for each brain, the first and last sections corresponding to 0.36 mm and 0.84 mm rostral from the centre of $M1_{FL}$, respectively. Depth measurements were performed along an axis geometrically normal to the cortical surface, to maintain consistency with the angle used during calcium imaging experiments (described in more detail in Chapter 4), and cortical depth measurements in the published literature (Hooks et al., 2011). For each mouse, the depth of L5B at the centre of $M1_{FL}$ (1.6 mm lateral, 0.6 mm rostral from bregma) was taken as the reference depth, and the depth of L5B at other anatomical locations was expressed in terms of the difference from the reference depth.

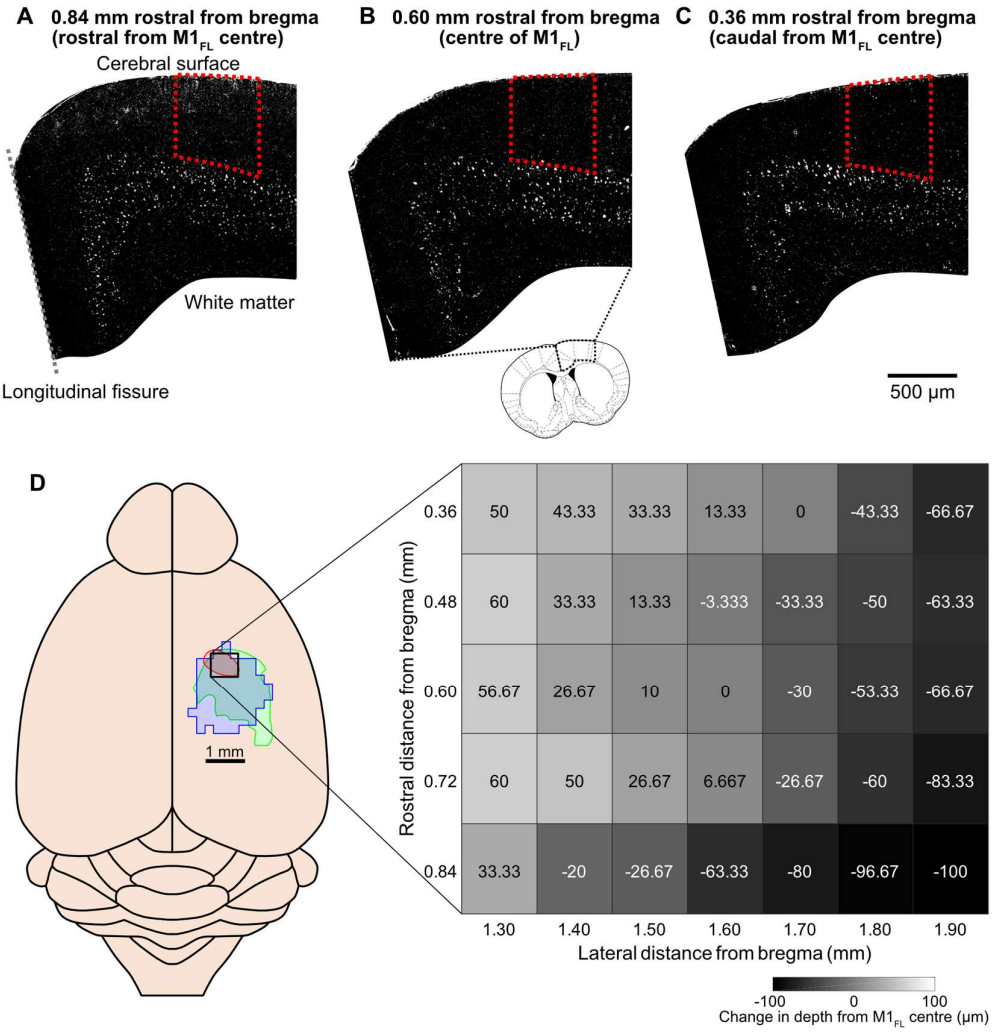

Figure 2.5: Variability of the upper boundary of L5B along the mediolateral and rostrocaudal axes, as defined by RetroBeads labelling.

A-C) *coronal images of cortex at 3 different rostral distances from bregma. The dotted red lines depict an area 1.3 mm to 1.9 mm lateral from the mid-line, corresponding to the left and right boundaries shown in the table below.*

D) *Left-hand side, schematic mouse brain outline as shown in Figure 2.1. Right-hand side, greyscale heat map indicating changes in L5B depth across mediolateral and rostrocaudal cortical coordinates. The horizontal axis represents lateral distance while the vertical axis represents rostral distance from bregma, and the edges of the heat map correspond to the black rectangle depicted in the schematic on the left. Elements in the heat map represent the mean values measured from 3 different mice, with '0' defined as the depth of L5B at the centre of $M1_{FL}$. Positive values indicate that L5B is shallower than the centre of $M1_{FL}$ while negative values indicate that L5B is deeper.*

In the central 9 elements of the heat map, the depth of L5B was relatively consistent (-4 ± 31 µm from central $M1_{FL}$, mean ± SD, n = 27, N = 3) but as one moves further from central $M1_{FL}$, the upper boundary of L5B becomes shallower in the rostromedial direction, and deeper in the caudolateral direction.

2.4 Discussion

2.4.1 Depth of L5B in forelimb M1

In this chapter, we describe the coordinates of $M1_{FL}$ on the cortical surface and provide comprehensive anatomical measurements of the depth of the upper and lower boundaries of layer 5B from the pial surface. Generating an anatomical map of L5B boundaries in the C57BL6 mouse provides a depth profile which will be used to guide the acquisition and analysis of calcium imaging experiments discussed in Chapter 5. However, as mentioned in the introduction of this chapter, previous publications have defined the depth of L5B in mouse M1 using different methods, which have resulted in inconsistent estimates of its upper bound. How can these contradictory results be reconciled?

It must be noted that while most cortical layers are functionally and anatomically distinct, their boundaries are nonetheless continuous. The density of PT-type cells increases with depth from the upper boundary of L5B (Anderson et al., 2010), while the position of the boundary itself varies with anatomical location within and across mice. Previous work in the Duguid lab defined the upper boundary of L5B to be 620 µm from the pial surface, as an intentionally conservative estimate to ensure that all electrophysiological recordings were performed within L5B (Schiemann et al., 2015). This is because there is no limitation on the depth of electrophysiological recordings, but depth readings can be imprecise due to the recording electrode compressing brain tissue as it descends from the pial surface. Thus, it is essential to target electrophysiological recordings to the central portion of L5B where there is the maximum probability of recording from L5B cells. Therefore, the boundary of L5B as defined by Schiemann et al. (2015) remains a conservative estimate of L5B depth. Using similar retrograde tracing and immunohistochemical techniques, we demonstrate that the boundary of L5B at the centre of $M1_{FL}$ is consistently shallower at ~500 µm from the pial surface.

The upper boundary of L5B has also been described as beginning at 570 ± 38 µm from the pial surface (Hooks et al., 2011), which is considerably deeper than our result. However, this measurement was made in the vibrissal area of the primary motor cortex (vM1) instead of $M1_{FL}$, and the depths of layer boundaries change markedly across different cortical areas (Hooks et al., 2013). The depth measurement of 570 µm was generated using an alternative

analysis methods where bright-field micrographs of unlabelled cortical slices were acquired and layer boundaries defined by visual landmarks. While such analyses have the advantage of being applicable to all layers of the cortex, we believe that the layer-specific retrograde labelling techniques we employed here provide a more precise measurement of L5B boundaries and depth.

2.4.2 Variability in L5B depth at different cortical coordinates

While it has been acknowledged that the laminar boundaries of L5B change with distance to the midline (Hooks et al., 2013), quantitative details of these changes have not been described in the literature. Here, we present a comprehensive map of the upper boundary of L5B in $M1_{FL}$ and how this depth changes across the rostrocaudal mediolateral extent of $M1_{FL}$.

Given the gross morphology of the mouse brain, this increase in depth in the lateral and caudal directions is to be expected, as the cortex of a mouse becomes narrower as you near the longitudinal fissure. This is also true in the rostral direction as the entire brain narrows towards the olfactory bulbs. Surprisingly, this consistent change in cortical thickness is rarely referred to in the literature. Since mouse cortex is smooth, changes in cortical thickness must necessarily lead to proportional changes in the total volume of brain tissue, and when comparing the relative size of somatotopic representations (or other forms of mapping), it would be advantageous to describe the three-dimensional cortical volumes of such representations, instead of two-dimensional areas mapped onto the brain surface.

The changes in layer boundaries should also be accounted for when targeting different areas of the cortex with recording electrodes, injections or imaging techniques. Existing wide-field calcium imaging techniques can record from planar fields of view in the cortex, ranging from about half a millimetre to several millimetres wide (Chen et al., 2017; Makino et al., 2017). In such recordings, layer boundaries will almost certainly change within the imaging field and as such, experiments investigating layer-specific activity should ensure that they account for the changing laminar boundaries across mouse cortex.

Chapter 3: A novel cued push/pull lever task for head-restrained mice

3.1 Introduction

There is a rich tradition in neuroscience of recording the neural correlates of movement in the motor cortex and other brain regions, in order to elucidate how motor actions are encoded (Georgopoulos and Carpenter, 2015; Sherrington, 1906). To understand animal behaviour, early ethologists such as Konrad Lorenz preferred to observe it outdoors *in situ*, as the constraints of a laboratory could potentially affect animal behaviour and introduce experimental artefacts (Lorenz, 1961). However, even a single mammalian limb has multiple degrees of freedom, and there are often countless ways to complete even a single given task, frequently leading to "repetition without repetition" across trials (Bernshteĭn, 1967). If every individual motor action is unique, and an animal is allowed to move freely, it can be difficult to objectively separate actions from each other and classify them into categories, while still obtaining sufficient numbers of actions in each category to meaningfully correlate with neural activity. That is why experimental animals in the field of neuroscience are often trained to perform constrained, well-defined movements of levers or manipulanda, with relatively restricted parameter spaces (Evarts, 1974, Georgopoulos et al., 1982, Saiki et al., 2014). Such behavioural paradigms have been used to explore motor circuits in many species, from primates to rodents (Evarts, 1974, Isomura et al., 2009). Due to the homologies in neural organisation across mammalian species, findings from rodent models can be used to advance our understanding human motor control, as well as addressing human motor pathologies (Balleine and O'Doherty, 2010, Karl and Whishaw, 2011).

The overarching aim of my doctoral thesis was to decipher how different movements are encoded at the single cell and network level in the primary motor cortex, by observing the neural correlates of 'directional' animal behaviour using two-photon calcium imaging *in vivo*. The long-term vision is to study the neural underpinnings of multi-directional movement control, so as a starting point we aimed to develop a task involving limb movements with as much difference as possible,: movements in two diametrically opposing directions. A forelimb lever push/pull task was chosen because extending and retracting a forelimb are

both actions that lie within the movement repertoires of untrained, freely-moving mice (Farr and Whishaw, 2002). In addition, mice have been successfully trained to perform forelimb lever push and pull tasks to examine neural circuits in the context of skilled motor behaviour (Isomura et al., 2009; Masamizu et al., 2014).

Therefore, my initial aim was to design and implement a forelimb behavioural paradigm where mice are trained to perform repeated push and pull actions to a user defined level of success. To ensure that any differences in neural activity were related to the difference between push and pull actions (and not other factors), the task was controlled to be directionally symmetrical, with the trial timings, cues, rewards, and trial frequency identical for both push and pull trials. After successful implementation of the task, two-photon population calcium imaging would be performed on trained mice to investigate the neural underpinnings of forelimb motor behaviour (see Chapter 4).

3.2 Materials and methods

3.2.1 Overview

All experiments and procedures involving animals were approved by the University of Edinburgh local ethical review committee and performed under license from the UK Home Office in accordance with the Animal (Scientific Procedures) Act 1986. Male 8-12 week old C57BL/6JCrl mice (20-30g) were group housed (2-4 littermates per cage) with enrichment in the form of running wheels, cardboard tubes and/or boxes. Mice were maintained on a reversed 12:12 hour light:dark cycle, and all experimental procedures were performed during the day. All experimental animals had *ad libitum* access to food and water, until the implementation of a water control protocol (details in Section 2.2.4). All surgical procedures were performed using aseptic techniques appropriate for mouse recovery surgery.

The basic design of the push/pull lever task was based on a push-only lever task developed by Dr. Joshua Dacre for his doctoral thesis, and the overall development of the training paradigm was conducted in close collaboration with current lab members Drs. Joshua Dacre, Julian Ammer, Stephen Currie and Julia Schiemann. Of the 26 mice which underwent behavioural training, data from 5 mice were generated by Dr. Stephen Currie.

3.2.2 Headplate implantation surgery

To facilitate stable two-photon population calcium imaging during behaviour (described in Chapter 4), mice were head-restrained using a custom-designed stainless steel headplate (Figure 3.1). Headplates were designed using Autodesk Inventor (Autodesk), and laser cut from 316L stainless steel by CRDM (3D Systems Europe). The main headplate design features were: 1) a central 6 mm hole to provide access to the skull of the mouse; 2) dual “wings” on the left and right hand side that could be clamped with fixing screws during training and imaging to provide a high degree of physical stability; 3) a large surface area to maximise contact with the skull while avoiding covering of the eyes at the rostral end of the headplate or the muscles surrounding the occipital bone at the caudal end; 4) a reasonably low mass to avoid excessively burdening the mouse; 5) sufficient stiffness to keep the headplate and brain physically immobile during the active motor task; and 6) a low profile design to accommodate

the large footprint of current 2-photon microscope objectives. Headplate implantation surgery was performed prior to all behavioural training.

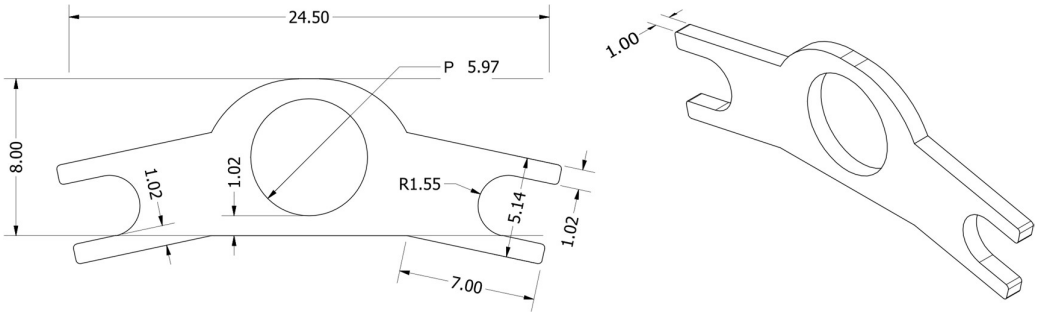

Figure 3.1: Schematic diagram of the head plate design used for mouse head restraint. Left – top-down view of the head plate with rostral portion at the front and caudal portion depicted by the flat back section. Right – isometric view of the head plate design. Head plates were laser cut from 316L stainless steel, and all values are in millimetres.

Prior to each surgery, mice were anaesthetised with 4% isoflurane (Abbott Pharmaceuticals, UK) in air before their scalps were shaved with an electric shaver. Mice were then placed in a stereotactic frame (Just for Mouse Stereotaxic Instrument, Stoelting Co.) for surgery. The isoflurane concentration was reduced to 1-2% for the remainder of surgery, and adjusted as necessary to ensure an adequate depth of general anaesthesia (target respiration rate of approximately 2 breaths per second, no pedal pinch reflex). After anaesthetic induction, viscous eye drops (Viscotears, Dr. Winzer Pharma GmbH, Germany or Bepanthen Ointment, Bepanthen) were applied to avoid corneal drying during surgery. The core temperature of mice was maintained at 37°C throughout surgery using an isothermal heating blanket and rectal thermocouple probe. Saline (0.7 ml sterile Ringer's Solution, for perianaesthetic fluid support), an analgesic (4 mg/kg Carprofen, Carprieve, Norbrook Laboratories Limited, to reduce post-operative pain and inflammation) and an anti-inflammatory (0.2 mg/kg Dexamethasone, Rapidexon, Dechra Veterinary Products, to reduce cerebral oedema and inflammation) were injected subcutaneously.

Surgeries were performed under a binocular surgical microscope. Incisions were made in the scalp and excess skin removed using a pair of sterilised surgical forceps and surgical scissors, until a sufficient area of the cranium was exposed (i.e. from between the eyes rostrally to slightly behind lambda caudally). The muscles lateral and caudal of lambda, as well as the

muscles around the eyes, were not exposed. The edges of the skin were glued to the skull with Vetbond Tissue Adhesive (3M) to seal off any exposed soft tissue. A sterilised surgical scalpel was used to scrape the skull clean of any remaining soft tissue, and then used to repeatedly score the skull to increase the surface area in contact with adhesive and dental acrylic (see below).

The headplate was then attached to the skull with cyanoacrylate adhesive (RS Pro Super Glue, RS Components Ltd.), such that forelimb M1 (1.6 mm lateral and 0.6 mm rostral of bregma) was positioned centrally in the headplate well. Once attached, additional cyanoacrylate adhesive was added to cover the remaining exposed skull within the head plate well. As a final step, dental acrylic (Jet Denture Repair Acrylic, Lang Dental Manufacturing Co., Inc.) was applied to the outer rim of the head plate to strengthen the bond between metal and skull, and additional cyanoacrylate used to fill the centre well.

After surgery, mice were moved to a temperature-controlled recovery cage (air temperature set at 28°C) until fully recovered from the effects of general anaesthesia, after which they were returned to their home cage. To reduce post-operative pain and inflammation, mice were subcutaneously injected with 4 mg/kg Carprofen (Carprieve, Norbrook Laboratories Limited) at 1, 2 and 3 days post-surgery. The total mass of the headplate, adhesives and acrylic was approximately 1.2 g, and mice did not display any difficulties moving nor show any other signs of distress related to headplate attachment post-surgery.

3.2.3 Description of the forelimb lever push/pull setup

Mice performed all stages of the behavioural training paradigm while restrained in the lever push-pull setup. This section will describe the physical hardware involved, while the following section will describe the steps involved in habituation, water control and behavioural training.

Mice were seated prone in a stainless steel tube, 35 mm in diameter (Figure 3.2), with the head fixed in position by independently movable clamps that attached to the headplate. The tube was lined with bench protector paper to absorb any urine produced during the task, allowing mice to rest comfortably in the tube for 30-60 min during training or recording sessions. The mouse was positioned such that the right forepaw could rest on a fixed rod

while the left forepaw rested on a moveable lever. The lever was designed to move 4 mm in a linear trajectory parallel to the rostral-caudal axis of the mouse, constrained by a low-friction nylon bush (i.e. providing minimal resistance to horizontal lever movement). Infrared sensors in the form of custom-designed light gates detected the start and end of the lever movement.

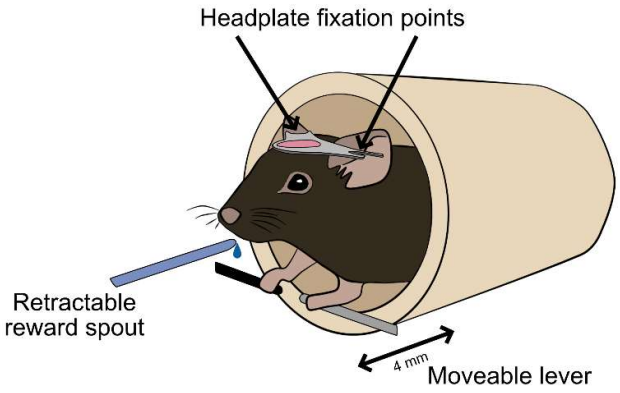

Figure 3.2: Schematic diagram of a head-restrained mouse in the lever setup. For behavioural training, each mouse was inserted into a stainless steel tube, with its left forepaw resting on a moveable lever and its right forepaw on a fixed rod. A servo-controlled retractable reward delivery spout dispensed a 5 µl water droplet upon successful completion of a trial, while a second servo resets/locks the lever at either the front or back position during inter-trial intervals or timeouts (full details of behavioural task in section 2.2.4).

An Arduino Uno (Arduino) microcontroller board, programmed to implement the behavioural tasks (described in Section 2.2.4), receives input from infrared sensors upon lever movement and sends output to the reward spout / lever servos (HXT900 Micro Servo, Hextronik Limited HK), a loudspeaker and a solenoid valve that controls water delivery to the spout. Upon successful task completion reward delivery is controlled by a solenoid valve that briefly opens (200 ms) to allow gravity-driven water to flow into the delivery spout. The volume of water dispensed depends upon the height of the water reservoir above the mouse and can thus easily be adjusted to regulate reward size. The Arduino output signals were acquired at 10 kHz using a Digidata 1440a Data Acquisition System (Molecular Devices), digitised and stored on a PC running Axon pCLAMP software (Clampex version 10.3.1.5, Molecular Devices). This provides records (.abf files) of task engagement and success during training and recording sessions (which were then used in Chapters 4 and 5). In addition, a

digital video of mouse behaviour was recorded using an infrared camera (Prosilica GC, Allied Vision Technologies GmbH) at 60 frames per second, and streamed/viewed real-time using a behaviour acquisition computer running StreamPix 6.5.0.0 (NorPix).

To reduce stress, behavioural training was performed in the dark using infrared cameras and illumination, and the entire experimental setup was surrounded by a box lined with sound reducing foam. A full schematic of the lever push-pull setup is shown below (Figure 3.3).

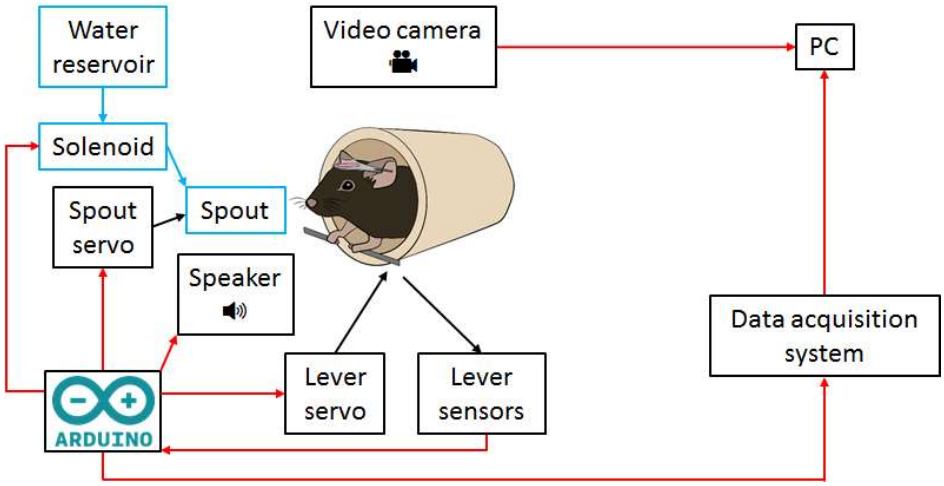

Figure 3.3: Schematic of the forelimb lever setup. Physical connections are drawn in black, reward delivery components in blue, and electronic connections are shown in red.

3.2.4 Behavioural training paradigm

For this chapter, days with respect to time from headplate implantation surgery will be referred to with a capital D, with Day 1 defined as the day of headplate implantation. Lower-case "day" refers to a standard calendar day. On Day 2, mice were allowed to recover from surgery. On Days 3 and 4, mice were handled twice daily for 5-10 mins per session to familiarise the mice with the experimenter.

To enhance rodent motivation it is frequently necessary to restrict *ad libitum* access to food or water, providing small amounts of food/water upon successful task completion (Guo et al., 2014; Tucci et al., 2006). For our training paradigm, mice were placed on a water control programme from Day 5 onwards. Water restriction was chosen over food restriction, because

it provides sufficient motivation for high performance, while causing less welfare concerns when compared to food restriction (Guo et al., 2014; Tucci et al., 2006). Also, chronic water restriction control is less likely to produce adverse health effects than chronic food control in mice, likely due to their evolutionary adaptations to dry environments (Fertig and Edmonds, 1969; Guo et al., 2014; Schwarz et al., 2010). On Day 5, *ad libitum* water supply was removed from the home cage, whereupon each mouse received a maximum of 1 ml of water per day, including water received as reward during successful behavioural training trails. Mice were weighed daily, with the body weight at the start of Day 5 taken to be 100%. Throughout training, mice were maintained at ≥85% body weight. Although rare, mice that dropped to 80-85% body weight were supplemented with an additional 0.2-0.5 ml water per day, while mice that dropped below 80% were returned to *ad libitum* water.

After behavioural training mice were placed temporarily in a separate cage to allow supplemental water to be consumed (i.e. total volume of water reward during training + supplement water volume = 1 ml of water per day). This ensured that each mouse received its appropriate daily water allowance while still being group housed with its littermates. Once training had started, the water supplement was given ~1 hour after training, so mice which received few rewards during a training session would not associate their poor performance with an immediate large post-training water reward. The water supplement was dispensed into a small custom-made bowl placed on the floor of the cage. Once mice had consumed all the water (within ~5 mins for well-trained mice) they were returned to their home cage.

On Days 5 and 6, mice were habituated twice daily to the head restraint apparatus for increasing periods of time (i.e. 10 mins during 1st session, 15 mins during 2nd session, 20 mins during 3rd session and 30 mins during 4th session). The timeline below summarises the behavioural training paradigm (Figure 3.4).

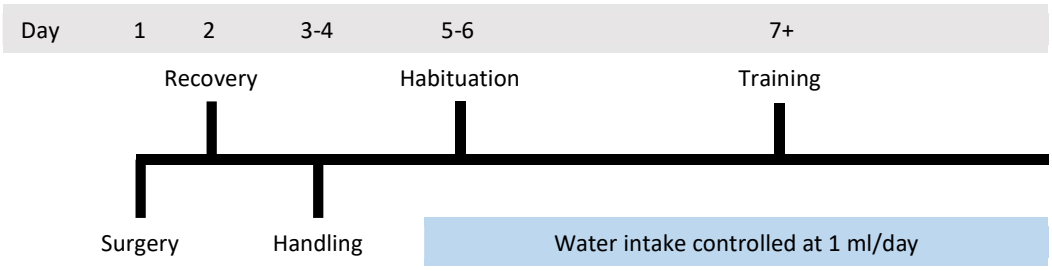

Figure 3.4: Timeline of mouse behavioural training. After headplate implantation surgery and 24 hours of recovery, mice were handled for two days, and then habituated to the head restraint apparatus for two days. Water control was initiated on Day 5.

From Day 7 onwards, mice were trained for 30 mins per day in a multi-stage training regime. At the beginning of each training session, mice were head restrained with the lever in the locked position for 5 mins to allow the mice to settle into the behavioural apparatus. After 5 mins, the lever was unlocked, and the lever was manually moved by the experimenter until 5 rewards were dispensed, as a demonstration of task completion. The 5 demonstration rewards were not included in analyses.

For Stage 1 of training, mice were required to push a lever from the back position to the front position (i.e. 4 mm of travel) to receive a 5 µl water reward. After each successful push and a delay of 500 ms, a retractable water spout would move toward the mouth of the mouse and dispense a 5 µl droplet of water, before retracting 2 seconds later. The spout was designed to be retractable in order to minimise exploratory licking and potential whisker/olfactory stimulation from the spout itself.

After each successful push trial, the servo returned the lever to the back position, whereupon the mouse received a second 5 µl water reward, 8 s after the first reward. If the mouse moved the lever away from the back position before 8 s had elapsed, the reward would not be administered until the point the mouse returned the lever to the back position. The task was designed in this manner so that both the front and back lever positions were equally rewarded to prevent the mice from associating only one direction with reward.

Following delivery of the reward in the rear position, there was a minimum interval of 8 s before the system would register and reward another push (Figure 3.5). Before the 8 s inter-reward interval was implemented, mice would rapidly push the lever back and forth in quick succession to try and maximise the rate at which they received rewards, making it difficult to cleanly separate and analyse push and pull actions.

Upon successfully achieving a user-defined performance target of >50 rewards per session for two consecutive sessions, mice were transferred to the next phase of training. In Stage 1 (and all subsequent stages), a target of 50 rewards per session was chosen to ensure that mice would perform at least 20 push and 20 pull trials during calcium imaging sessions (see Chapters 5,6 and 7) and the sample size of push and pull trials would be large enough to

conduct statistical tests based on resampling. Mice were advanced to the next stage of training when they reached their own performance target, as opposed to deriving the maximum number of days required for a training stage and subjecting all mice to that number of training days (Guo et al., 2014).

The aim of Stage 1 was to reinforce the association between lever push movements and water reward (Skinner, 1951). Stage 1 was designed so that the innate behaviour of naïve untrained mice (i.e. repositioning their paws on the lever) would occasionally lead to lever movements and rewards being dispensed. This 'random' completion of the task provided the opportunity for mice to begin to learn the association. After successful completion of Stage 1, mice could then be trained to perform increasingly complicated behavioural tasks, through Skinnerian shaping.

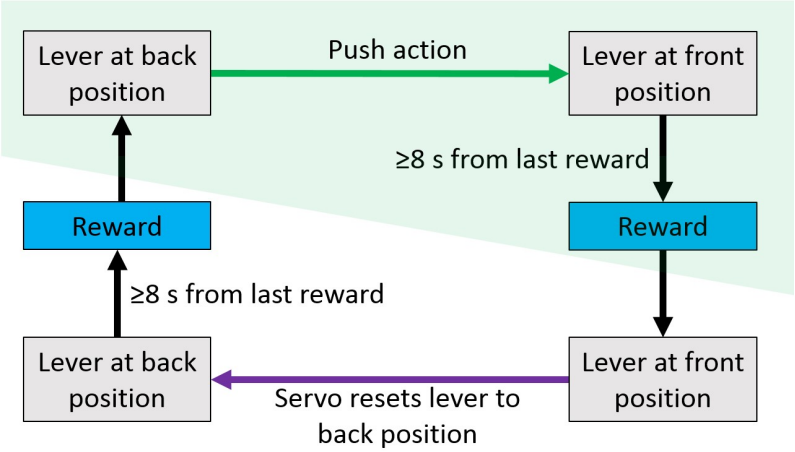

Figure 3.5: Flowchart describing Stage 1 of the behavioural task. The push portion of the task is shaded green, the mouse push is depicted as a green arrow, and servo movement is depicted as a purple arrow. Blue boxes represent rewards.

Stage 2 was structured in a similar way to Stage 1, except that the servo did not return the lever to the back position after each push so mice had to alternate between performing lever push and pull actions (Figure 3.6). After receiving >50 rewards per session for two consecutive sessions on Stage 2, mice would be transferred to the final phase of training, Stage 3.

The aim of Stage 2 was for mice to associate both push and pull actions with rewards, to prepare them for Stage 3, which required them to perform push and pull actions upon presentation of an auditory cue. Stage 1 and 2 were relatively simple tasks designed to reward increased engagement with the lever, so that mice would be sufficiently motivated to attempt the more complex cued paradigm (Stage 3).

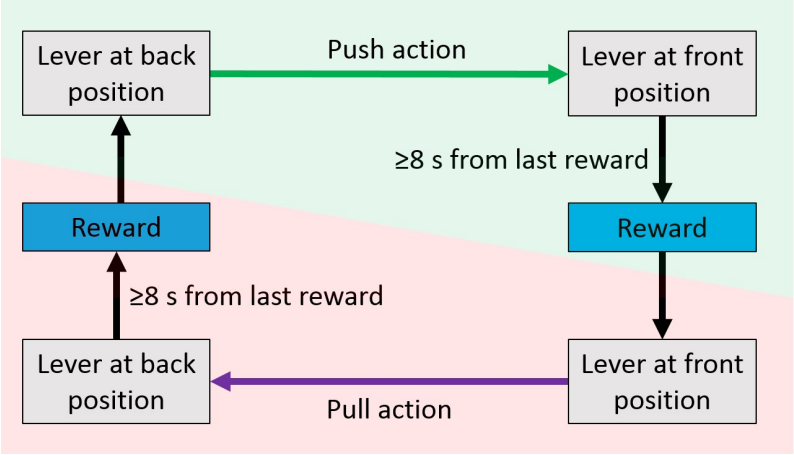

Figure 3.6: Flowchart describing Stage 2 of the behavioural task. The push section of the task is shaded green, while the pull section is shaded red.

Stage 3 involved training mice to perform repeated push/pull sequences (Figure 3.7)**Error! Reference source not found.**. Initially, the behaviour would begin with the lever in the back position and mice had to learn to remain stationary for 6-8 s until the presentation of a 'Go' cue in the form of a 10 s 6 kHz tone. If mice did not remain stationary during this period and the lever moved from the back position, the lever servo would be engaged and the lever would be returned to the back position and locked for 2 s (i.e. a 2 s timeout). After completion of the timeout a subsequent trial would be initiated. During the cue presentation mice were free to engage in a lever push action and if successful the lever would be locked in the forward position for 2 s whereupon a water reward would be dispensed. The cue presentation terminated 2 s after the mouse performed a successful action. However, if the mouse failed to move within the 10 second cue presentation period, the lever servo would reset and lock for 2 s (i.e. 2 s timeout), before a subsequent trial was initiated. After successful completion of a push trial, mice would then perform a lever pull trial after presentation of a second 'Go' cue (i.e. symmetrical but opposite to a push trial).

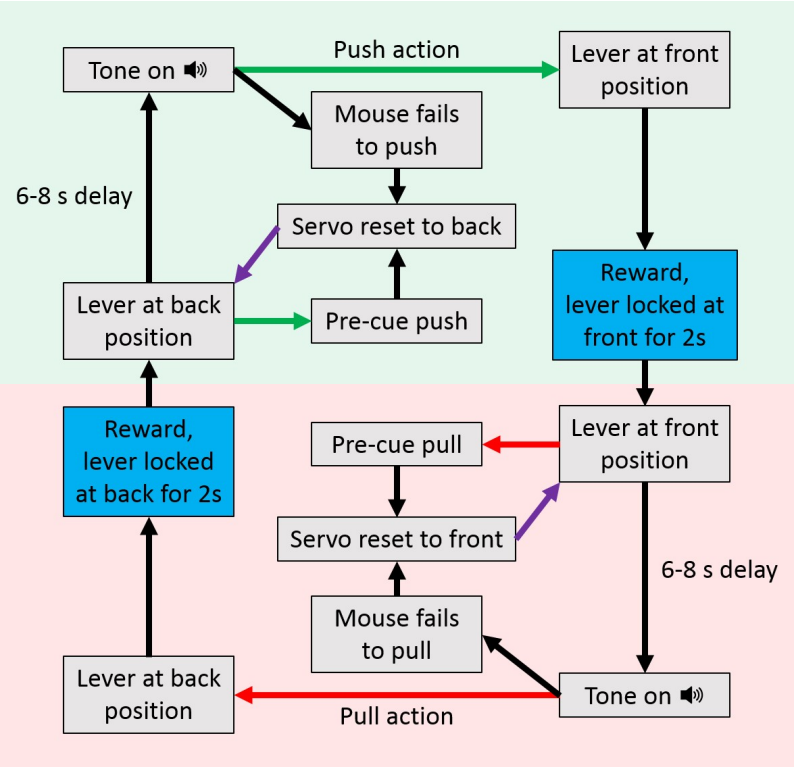

Figure 3.7: Flowchart describing Stage 3 of the behavioural task. The outermost clockwise loop represents the desired behaviour. The central portions indicate failed trials, which could occur if 1) the mouse moved the lever before cue presentation (pre-cue movement), or 2) if the mouse failed to push/pull the lever during cue presentation. In both situations, the lever will be reset to its original position and locked for 2 s (i.e. 2 s timeout) before initiating the next trial.

In some mice (8/26 mice), the 10 s tone was gradually reduced from 10 s to 2 s during Stage 3 of training. All other training parameters remained constant.

The 'Go' cue was implemented in Stage 3 to enforce a 6-8 s period of inactivity preceding push or pull actions, a necessary prerequisite for isolating movement-related changes in fluorescence when performing population calcium imaging during behaviour (see Chapter 4) (Andermann et al., 2010). A pseudo-randomised delay period of 6-8 s was selected to avoid mice predicting the timing of the tone onset. The structure of the task was designed to ensure that mice executed repeated push-pull sequences, resulting in the number of successful push versus pull trials being equal.

As with Stages 1 and 2, mice that achieved >50 rewards per session for 2 consecutive training days were considered 'expert'. Given that mice learn the task at different rates, attaining the

expert level threshold required a different number of training sessions per individual mouse. Mice which were unable to reach the final threshold of Stage 3 within 7+ days were considered to have significantly reduced motivation for the task (Chen et al., 2014) and excluded from all further analyses.

3.3 Results

3.3.1 Task performance of mice across training stages

The objectives of the training paradigm were to:

1) Teach mice to rapidly achieve a user defined 'expert' level in a cued push-pull behavioural paradigm
2) Demonstrate that 'expert' performance at Stage 3 requires associative learning.

To address objective 1), many methods can be used to quantify the performance of mice during behavioural tasks, and one such method is to count the number of successful trials per training session (Chen et al., 2014). Since each training session was conducted over a fixed time period of 30 minutes, the number of rewards obtained per training session provides a robust measure of behavioural performance (Figure 3.8).

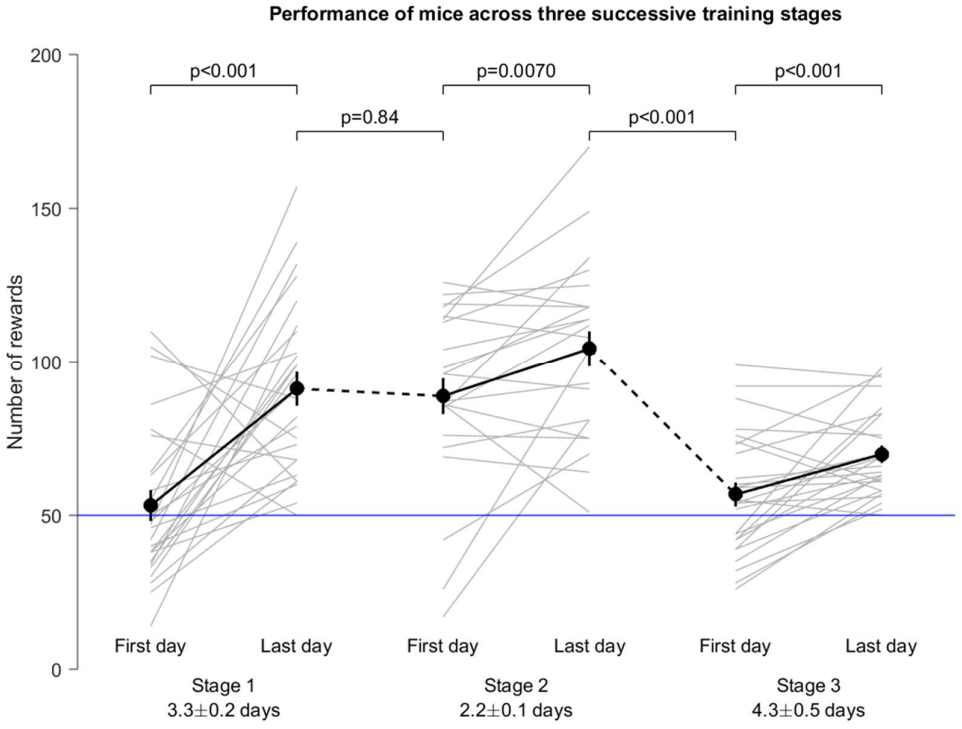

Figure 3.8: Performance of mice (N = 26) trained over the three successive training stages. 5 mice failed to reach the final threshold of Stage 3 and were excluded. The performance of

each mouse, measured by the number of rewards obtained in a training session, is represented by a thin grey line. The mean population performance and s.e.m. are represented by thick black lines. The blue horizontal line indicates the performance threshold for each stage (i.e. 50 rewards). Due to different mice spending differing amounts of time on each stage, only the first (left) and last (right) training days of each stage are presented. Dashed lines indicate the mean change in performance between stages. 5 mice were only trained for 1 day at Stage 2 (>100 rewards for all 5 mice), so they were omitted from the Stage 2 graph and statistics. The upper set of p-values indicate the significance of performance within each training stage (one-tailed t*-test), while the lower set of p-values indicate the significance of performance between stages (two-tailed* t*-test).*

Over the course of behavioural training, mice significantly improved their performance across all 3 stages (Figure 3.8). Stage 1 and Stage 2 were completed in 3.3 ± 0.2 days and 2.2 ± 0.1 days, respectively, while Stage 3 was completed in 4.3 ± 0.5 days. The significant increase in performance within each training stage indicates that mice underwent associative learning.

Stage 2 entailed an increase in the task complexity compared to Stage 1, and when comparing the last day of Stage 1 against the first day of Stage 2, there was a small but insignificant decease in the mean number of rewards obtained. In contrast, the reduction in task success between the last day of Stage 2 and the first day of Stage 3 was far greater and statistically significant, likely due to the increase in task complexity.

The endpoint of behavioural training was to be able to perform *in vivo* population calcium imaging during behaviour to record the neural correlates of push and pull actions. Since the action type (push or pull) was the only independent variable, other variables across and within each recording session should be held constant wherever possible. However, it is known that mice can become progressively sated and/or fatigued during the course of a behavioural training session, resulting in decreased performance over time (Guo et al., 2014). The decrease in performance could reflect changes in their internal physiological states that can potentially influence neural activity.

Therefore, behavioural performance was used as a proxy for the internal state of mice, under the assumption that sated and/or fatigued mice would perform worse when compared to mice that had just started a training session. To examine this, I divided the first and last Stage 3 sessions into three 10 minute bins, and the number of rewarded trials was compared across bins (Figure 3.9).

Figure 3.9: Performance of mice (N = 26) during the first (left) and last (right) training days of Stage 3. Performance per session was divided into three equal 10 min epochs. The performance of each mouse is represented by a thin grey line, while the thick black lines indicate the population mean and s.e.m.

Whether at the start or end of Stage 3 training, mice were consistent in the rate at which they acquired rewards. When training sessions were split into 10 min bins, reward count per bin was consistent, with the number of rewards remaining consistent across each 10 min bin for both the first day (d.f. = 2, F = 0.27 , p = 0.77, repeated measures ANOVA) and last day (d.f. = 2, F = 1.96 , p = 0.15, repeated measures ANOVA). Therefore, it can be concluded that mice did not experience significant changes in their levels of water satiation and fatigue within their 30 min training sessions, at least not to the point of causing changes in performance.

3.3.2 Sample lever traces

Infrared sensors in the lever setup enabled constant tracking of the lever position, while other task features such as tone onset/offset, time of lever reset and completion of successful trials were also continuously recorded with pCLAMP 10 acquisition software. These elements can be plotted over time to visualise how mice performed during typical behavioural training sessions and to examine the relationship between behavioural elements and neural activity (see Chapters 4-7). Below are two representative lever output traces from a mouse on the first and last day of Stage 3 training (Figure 3.10).

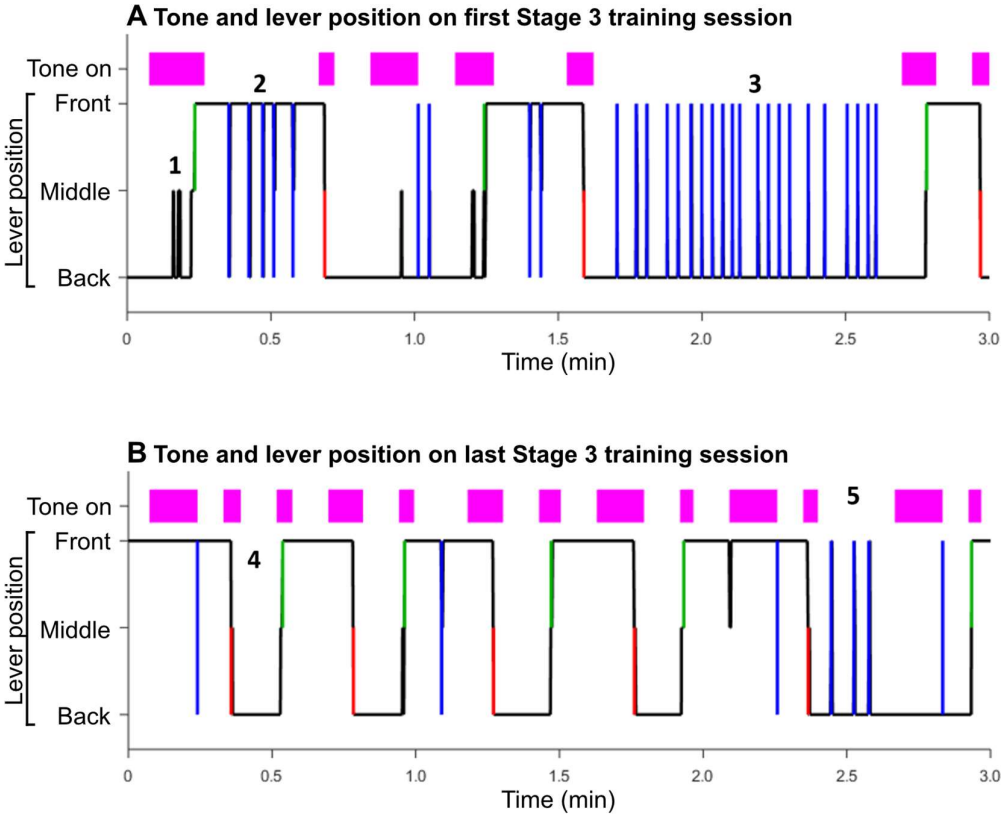

*Figure 3.10: Representative lever movement trajectories performed by a single mouse on the **A)** first and **B)** last session of Stage 3 training, truncated to the first 3 minutes. The magenta bars above each lever trace indicate cue presentation. The black line indicates the position of the lever, which could either be at the front, back or middle position. Blue lines indicate when the mouse made a pre-cue movement, leading to the lever being reset back to the initial lever position. Green lines indicate successful rewarded pushes, and red lines indicate successful rewarded pulls.*

Mice tended to become more proficient at performing the task after training. Figure 3.10 depicts a mouse which visibly improved its performance after Stage 3 training. The mouse successfully completed more trials and produced fewer pre-cue movements during the last Stage 3 training day when compared to the first Stage 3 training day. At time point **1**, on the first Stage 3 training day, the mouse pushed the lever to the middle position and returned it to the back position multiple times before successfully pushing it all the way to the front whereupon it received a reward. This back-and-forth 'rowing' motion was repeated again around 1.2 minutes into the recording. This particular mouse also performed long sequences of pre-cue pulls (**2**) and pushes (**3**), most likely due to its unfamiliarity with the cued aspect of the Stage 3 task.

On last day of Stage 3 training, overall performance had significantly improved. The behaviour now incorporated repeated cue-evoked lever push-pull sequences (**4**), and although pre-cue movements still occurred (**5**), they occurred infrequently. The reduced number of pre-cue movements allowed the mouse to experience more cue presentations (magenta), due to each pre-cue movement resulting in a lever reset and timeout before the next trial begins.

3.3.3 Necessity of a multi-stage behavioural training paradigm for enhanced task success

In order to determine whether Stage 1 and Stage 2 were important for shaping mouse behaviour prior to Stage 3, and to test whether lever push and pull actions are innate motor behaviours, 3 naive mice were trained directly on Stage 3 without first being promoted through Stages 1 and 2 (Figure 3.11). These mice underwent the same headplate surgery, handling, habituation and water-restriction procedures, except that instead of starting their training at Stage 1 on Day 7, the lever setup was programmed to challenge mice with Stage 3 from the outset.

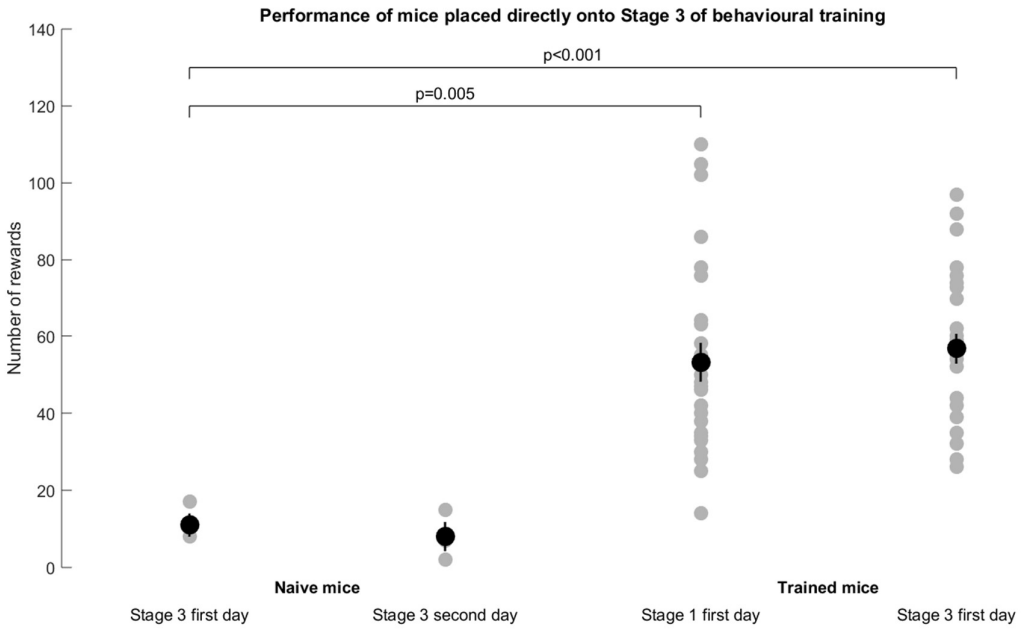

Figure 3.11: Performance of naive mice placed directly onto Stage 3. Grey circles depict the performance of Individual mice, while black circles depict the mean and s.e.m. From left to right, the first two columns indicate the performance of naïve mice across two days of Stage

3 training. The third and fourth columns indicate the performance of regularly trained mice, on the first day of Stage 1 and the first day of Stage 3, respectively. Naïve mice N = 3, regular mice N = 26.

The performance of naïve mice was significantly worse on the first day of Stage 1 (d.f. = 27, $p = 0.005$) and the first day of Stage 3 (d.f. = 27, $p < 0.001$), than mice which were trained sequentially on all 3 stages (Figure 3.11), indicating that the initial two stages were important for shaping mouse behaviour (one-tailed unpaired *t*-test).

In addition, the stark difference in performance between trained mice on the first day of Stage 3 and naïve mice on the first day of Stage 3 indicates that objective 2) was satisfied. The innate behaviour of naïve mice cannot account for the level of performance observed in trained mice at Stage 3, therefore performance in Stage 3 results from associative learning over the multiday training paradigm.

In contrast, the relatively high level of task success observed in naïve mice on Stage 1 suggests that Stage 1 performance can be attributed to either innate behaviour or rapidly acquired learnt behaviour, a necessary prerequisite for the first phase of a multi-stage behavioural shaping paradigm.

3.4 Discussion

In this chapter, we present a training paradigm in which head-restrained mice learn to perform a cued push/pull lever task. After training mice generated stereotyped and reproducible learned movements, which provided a behavioural platform from which to investigate the cortical control of skilled forelimb movements using 2-photon population calcium imaging.

3.4.1 Ethological relevance of forelimb behaviour

Like most mammals, mice possess a large repertoire of motor behaviours. When designing behavioural tasks that require mice to reproducibly generate motor output, many options are available, such as self-paced locomotion, nose-pokes, licking and or forelimb object manipulation (Beloozerova and Sirota, 1988; Guo et al., 2014; Malkki et al., 2010; Rossi and Yin, 2012). Of these many options, I selected a forelimb task, as forelimb object manipulation is an ability shared by higher order mammals and rodents, and is dependent on descending motor cortical output (Morandell and Huber, 2017; Ogden and Franz, 1917; Penfield and Boldrey, 1937). The overarching aim of this thesis was to understand how different movements are encoded in primary motor cortex. To that end, I designed and implemented a lever manipulation task involving two diametrically opposed movements, as it is expected that such movements would have the greatest divergence in their neural correlates (Georgopoulos et al., 1982).

Is pushing and pulling a lever ethologically relevant for mice? Behavioural paradigms that depart too far from their untrained behavioural repertoires may be difficult to implement (Crawley and Paylor, 1997). For example, mice may struggle with complicated motor tasks, even those which have been successfully implemented to investigate human and/or monkey behaviour, because mice have less developed fine motor skills (Courtine et al., 2007; Gu et al., 2017). However, mice are avid burrowers: untrained mice use their forelimbs to voluntarily dig loose substrates (Deacon, 2009), and to push and pull bedding around their cages (Garner et al., 2017). In addition, they spontaneously extend and retract their forelimbs to grasp food and bring it towards their mouth for consumption (Farr and Whishaw, 2002). Since the forelimb trajectories required for mice to burrow or grasp food include forelimb

extension, retraction and object manipulation, pushing and pulling a lever engages similar muscle groups, is comparable to their normal behavioural repertoire in the 'wild', and can be considered ethologically relevant.

3.4.2 Does the push/pull task constitute skilled behaviour?

Though the boundary between "skilled" and "unskilled" is subjective and often poorly defined, it is nonetheless important to define it in the context of investigating M1 activity. According to Kawai et al., motor skills are "task-specific learned motor sequences" (Kawai et al., 2015). This is the working definition I will use throughout my thesis. By definition, skilled motor behaviour must be composed of sequences of physical movements that are learned, with increasing task performance over successive training days constituting evidence of learning. For all 3 training stages, mice performed significantly better on the last day of training than the first day of training (Figure 3.8), while naïve mice placed directly onto Stage 3 performed poorly (Figure 3.11). These findings provide strong indicators that attaining 'expert level' on Stage 3 was task-specific, and dependent on motor skill learning.

3.4.3 Summary

We sought to create an ethologically and neurobiologically relevant behavioural paradigm to provide a context for investigating population coding in $M1_{FL}$. To this end, we created a skilled motor task where mice were trained to perform repeated push and pull actions. We successfully developed and implemented such a task, with ~84 % of mice being able to achieve 'expert' level within 10 ± 3 days (SD). This provides a behavioural framework which we will employ to investigate the neural correlates of movement in primary motor cortex in later chapters.

This page was intentionally left blank.

Chapter 4: Two-photon calcium imaging in Layer 5B of mouse forelimb motor cortex: potential pitfalls of imaging in cortex during behaviour.

4.1 Introduction

The aim of this thesis is to study neuronal population activity in L5B of mouse $M1_{FL}$ during the execution of learned movements using two-photon population calcium imaging. While calcium imaging in the upper layers of mouse cortex has become commonplace in the last decade, there are several problems associated with calcium imaging in deep layers of cortex during behaviour. This chapter will discuss the potential pitfalls and the measures taken to address them.

4.1.1 Two-photon calcium imaging using the genetically-encoded calcium indicator GCaMP6s.

Calcium imaging is a relatively new technique, compared to the venerable electroencephalograph or tungsten microelectrode. It involves the labelling of neurons with calcium indicators, which are molecules that respond to changes in calcium concentration by altering their fluorescence properties. In neurons, action potentials lead to the opening of voltage-gated calcium channels, an influx of calcium ions, and increased intracellular calcium concentration. Therefore, the fluorescence levels of a calcium indicator present within a neuron can be used as a proxy for neuronal activity. Early calcium imaging studies in the 1980s used chemical calcium indicators based on BAPTA such as fura-2 (Cannell et al., 1987), but there has been a general shift towards using genetically encoded calcium indicators (GECIs) for calcium imaging ever since they were produced by the Tsien lab in 1997 (Miyawaki et al., 1997). GECIs have two key advantages over chemical calcium indicators: they are proteins synthesised by target cells so they do not need to be loaded into cells immediately before each imaging session, and unlike chemical calcium indicators that are indiscriminately taken up by all cell types, they can be targeted to specific cell subpopulations or even subcellular compartments using the appropriate genetic promoters and targeting sequences

(Lock et al., 2015). Thus, calcium imaging is able to target specific cell types using intersectional genetic strategies, and record from neuronal populations while still preserving single-cell resolution (Chen et al., 2013a).

As one performs calcium imaging in deeper imaging planes within the mouse cortex (> 400 µm from cortical surface), light scattering of emitted light increases, and fluorescence from the upper cortical layers increases the background signal during imaging (Grienberger and Konnerth, 2012; Mittmann et al., 2011; Oheim et al., 2001). Surprisingly, light absorption is not a major influence on light attenuation in neural tissue: the scattering coefficient of visible light in brain tissue is more than an order of magnitude higher than the absorption coefficient of visible light, so ~95% of light attenuation is caused by light scattering (Cuccia et al., 2009). The overall effect is that the signal-to-noise ratio decreases as a function of distance from the pial surface, limiting the maximum imaging depth. There are several measures that can be taken to overcome these constraints while performing deep-layer imaging: 1) selecting fluorescent indicators with better quantum yields, 2) increasing the wavelengths used (as longer wavelengths scatter less in brain tissue), 3) increasing the excitation laser power, and 4) decreasing the expression of fluorophores in upper cortical layers (Kobat et al., 2009; Theer and Denk, 2006).

The GCaMP6 series of GECIs are GFP-based calcium indicators, which exhibit high sensitivity, calcium affinity, and fast kinetics (Chen et al., 2013b). As the GCaMP6s variant demonstrates the largest dynamic responses to calcium (changes in fluorescence from baseline level after neuron spiking), and best signal-to-noise ratio (Chen et al., 2013b), it was chosen as most appropriate GECI for calcium imaging throughout this doctoral thesis project.

Fluorophores including calcium indicators have fixed excitation spectra, and like most other GFP derivatives, GCaMP6s has an excitation peak at 470 nm (i.e. blue light) which is strongly scattered by brain tissue (Al-Juboori et al., 2013; Chen et al., 2013b). However, the fixed nature of excitation wavelengths can be circumvented using two-photon imaging. This technique was developed in the 90s as an improvement over single-photon fluorescence microscopy (Denk et al., 1990). Unlike single-photon fluorescence microscopy where light source is set to the excitation wavelength of the fluorophore, in two-photon imaging a femtosecond pulsed laser produces photons which bear approximately half the energy of the standard excitation wavelength. While GCaMP6s has a single-photon excitation peak wavelength at 470 nm, its two-photon excitation peak wavelength is at 920 nm (i.e. near-

infrared light) (Chen et al., 2013b). Compared to blue light, infrared photons scatter less in tissue and are less energetic, leading to better depth penetration, lower levels of photobleaching, and less phototoxicity (Al-Juboori et al., 2013; Denk et al., 1994). During imaging, the excitation laser scans across a field of view in one plane of focus, leading to an optional sectioning effect with a high degree of spatial resolution, and a rapid drop-off in power (i.e. off-target fluorescence and phototoxicity) at locations outside the focal point. Producing more laser power is not a limitation during calcium imaging as modern lasers can be scaled to arbitrarily high power levels in the milliwatt range, but photoxicity at higher laser intensities can produce undesired effects.

In this study, I used a variant of two-photon microscopy termed LOTOS (low-power temporal oversampling), incorporating a high-frequency resonant scanner moving the beam along the X-axis, with a lower-frequency galvanometer scanner responsible for beam movements in the Y-axis (Chen et al., 2012). This arrangement enabled data acquisition at a high frame rate using a relatively low average but high instantaneous laser power. This results in minimal unwanted laser-related issues such as photobleaching, photoxicity, and thermal changes, while still maintaining a good signal-to-noise ratio.

Finally, to reduce background fluorescence coming from above the imaging plane, virus injections were centred directly in at the target region of L5B, 600 µm below the cortical surface, thus reducing the expression of GCaMP6s and therefore the fluorescence of neurons in the upper layers.

4.1.2 Potential pitfalls of our calcium imaging method

While traditional electrophysiological techniques offer high temporal resolution recordings at the sub-millisecond level, calcium imaging is comparatively limited in that regard. GCaMP6s has relatively slow kinetics: given a burst of 10 action potentials in dissociated rat hippocampal neurons, the average time to reach peak fluorescence is 480 ± 24 ms and the decay time ($t_{1/2}$) is 1796 ± 73 ms (Chen et al., 2013b). Thus, neuronal events that occur up to 4 s before a cued lever movement could potentially affect the fluorescence changes at the time of movement onset. Mice are generally restless animals that seldom remain still (an immobile mouse is either freezing in fear, asleep or unwell) making rapid, random

movements during large sections of behavioural training and imaging sessions. Despite being head-restrained, trained animals groomed themselves approximately every 60 s, and repositioned their forelimbs/hindlimbs and body position. Thus, to what extent do non-task-related movements affect neuronal population activity in primary motor cortex?

Another potential pitfall is sampling bias caused by the non-random identification of neurons. My aim was to perform neuronal population imaging in motor cortex, but during imaging sessions I had no direct way of measuring the total number of neurons physically present in each optical section (i.e. field of view). During the analysis of calcium imaging data, neurons were manually identified by the experimenter, and as such, neurons that did not display any changes in fluorescence during the recording session would remain 'invisible'. While this issue applies to any form of imaging, it is perhaps more important in deep-layer imaging where signal-to-noise can be reduced. Neurons may remain undetectable for a variety of reasons, from low level GCaMP6s expression, to persistent low levels of neuronal activity leading to negligible changes in GCaMP6s fluorescence.

If during calcium imaging experiments I only recorded the activity of a small fraction of the neurons present in each field of view, then this would limit our ability to investigate principles of population coding in M1. Moreover, undersampling L5B population activity would constitute a sampling bias and could potentially lead to misleading conclusions. Therefore, our aim was to find an independent measure of neuronal cell density in L5B and compare it with the neuronal cell density observed during 2-photon population calcium imaging.

Finally, as with any experiment involving viral transduction, there was the danger that the expression of GECIs in L5B of $M1_{FL}$ (see Chapter 2) was not reproducible and consistent. Imaging deep in cortex requires a sufficient level of GECI expression to ensure adequate levels of fluorescence in the target region. Since GCaMP6s expression was generated by viral injection several weeks prior to imaging, I had to ensure that virus injections reliably produced GCaMP6s expression throughout L5B of $M1_{FL}$. To address, we conducted a thorough histological analysis of GCaMP6s expression patterns across mice to confirm our virus expression patterns were accurately targeted to and covered the majority of $M1_{FL}$.

4.2 Materials and methods

4.2.1 Overview

All experiments and procedures involving animals were approved by the University of Edinburgh local ethical review committee and performed under license from the UK Home Office in accordance with the Animal (Scientific Procedures) Act 1986. Male 8-12 week old C57BL/6JCrl mice (20-30 g) were group housed (2-4 littermates per cage) with enrichment in the form of running wheels, cardboard tubes and/or boxes. Mice were maintained on a reversed 12:12 hour light:dark cycle. All experimental animals had *ad libitum* access to food and water, until the initiation of the water restriction schedule described in Chapter 3. All surgical procedures were performed using aseptic techniques appropriate for mouse recovery surgery.

In total, 47 C57BL/6JCrl mice were used for L5B population imaging. Of the 47 mice, data from 11 mice was acquired by Dr Stephen Currie as part of an ongoing collaboration.

4.2.2 Virus injection and headplate implantation surgery

Surgical procedures for headplate implantation were performed as described in Section 2.2.2, except that viral injection procedures (as described below) were conducted after an incision was made to the scalp, and before the edges of the skin were glued with Vetbond.

To label motor cortical neurons with GCaMP6s, we injected wildtype mice with an adeno-associated virus (AAV), AAV1.Syn.GCaMP6s.WPRE.SV40 (Penn Vector Core, University of Pennsylvania). AAVs are versatile DNA vectors that are able to transfect many mammalian cell types, and are able to stably produce high levels of transgene expression with little reported adverse effects (Grienberger and Konnerth, 2012; Salganik et al., 2015). The synapsin promoter (Syn) present in the viral payload restricted expression of the GCaMP6s construct exclusively to neuronal cells, ensuring that non-neuronal cells were not labelled (Schoch et al., 1996). AAV viral aliquots (5.02×10^{13} infectious units/ml, stored at -80 °C) were diluted with external saline solution (150 mM NaCl, 2.5 mM KCl, 10 mM HEPES, 1 mM $CaCl_2$, and 1 mM $MgCl_2$, adjusted to pH 7.3 with NaOH) to a final concentration of 10% immediately

before virus injection surgery, and kept frozen on dry ice at all times other than during dilution and injection procedures.

A three-axis stereotactic micromanipulator (Just for Mouse Stereotaxic Instrument, Stoelting Co.) was used to measure the anatomical coordinates for bregma and lambda, and the orientation of the skull was adjusted until bregma and lambda lay on the same frontal and sagittal planes. A small craniotomy was produced at 1.18 mm lateral and 0.18 rostral from bregma with a handheld dental drill (0.5 mm diameter drill burr). During drilling, the craniotomy was periodically cleared using compressed air and washed with external saline solution to remove swarf and minimise thermal changes in the skull. The bone was thinned to the point at which the bone depressed slightly when gently pressed with a pair of #5 forceps, then the central portion of bone ~200 µm wide was removed. A calibrated injection pipette (pulled glass pipette, 5 µl Calibrated Micropipette, Drummond Scientific Company) was pre-filled with ~300 nl of virus solution. To access the injection target location (1.6 mm lateral and 0.6 mm rostral from bregma, 0.6 mm deep from the cortical surface), the pipette tip was lowered to the dural surface at the centre of the craniotomy at an angle 45° from vertical, and 45° rostro-lateral when viewed from above, then slowly inserted into the brain to a depth of 0.85 mm from the cortical surface (Figure 4.1).

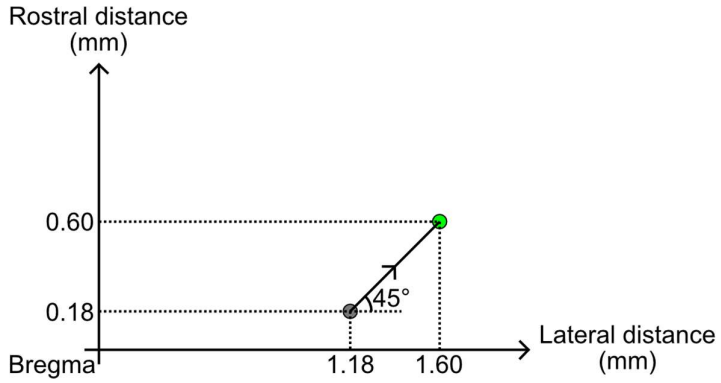

Figure 4.1: Schematic of virus injection on the cortical surface, viewed from above. The grey circle represents the location of the virus injection craniotomy, and the green circle represents the centre of the virus injection site. In addition to the 45° angle illustrated, the injection pipette (arrow) was also angled 45° downwards with respect to the cortical surface, and the injection site was positioned 600 µm below the cortical surface.

A Picospritzer III (Intracel) driven by compressed air was used to slowly inject 200 nl of the virus solution (20-40 ms pulse duration, 10-40 psi, 2 s inter-pulse interval with a target flow rate of 40 nl/min). The pipette was left in situ for 5 mins to ensure adequate stabilisation of pressure in the target zone before being slowly withdrawn. After the pipette was fully withdrawn, the injection craniotomy was sealed with a small volume of platinum-cure silicone (Body Double Fast Set, Smooth-On). Following the procedures described here, headplate implantation, other surgical procedures, and post-operative care were performed in the same manner as described in Section 3.2.2. Mice were then trained to perform the bidirectional lever task, as described in Section 3.2.4.

4.2.3 Cranial window implantation

Mice which had completed Stage 3 of behavioural training (see Chapter 3) were implanted with a cranial window to facilitate 2-photon population calcium imaging. Mice were prepared for surgery, anaesthetised, and injected with saline, Carprofen, and Dexamethasone, as described in Section 3.2.2. The upper surface of the headplate and the headplate well were cleaned and sterilised by wiping with a sterile cotton swab soaked in 70% ethanol, then dried with another sterile cotton swab. A handheld dental drill (0.5 mm diameter drill burr) was used to etch a square outline around central $M1_{FL}$ (1.6 mm lateral and 0.6 mm rostral from bregma), the edges of the square being approximately 2 mm long. The dental drill was then used to thin the bone at the edges of the square, until the bone depressed slightly when gently pressed with a pair of sterile #5 forceps (Dumont). During drilling, the craniotomy was periodically cleared using compressed air and washed with external saline solution to remove swarf and minimise thermal changes in the skull. If any significant bleeding occurred, drilling was paused, the area washed with external saline solution until the bleeding stopped and dried with a sterile cotton swab and compressed air. After all the edges were thinned, any remaining swarf was removed, and the central headplate well flooded with external saline solution for 5 mins to soften the thinned bone. From this point until the cranial window was affixed, the central headplate well was kept wet with external saline solution to avoid drying and damaging of the brain. One arm of the #5 forceps was then used to carefully pierce an edge of the square at an angle close to horizontal, then slid sideways along the edge of the square, parallel to the cranial surface, to create a ~200 µm wide opening. One arm of a sterile

#4 forceps (Dumont) was then inserted into the opening between the dura and bone, with the other arm used to grip the upper surface of the bone square. The central square of bone was slowly and carefully lifted away from the brain until it detached from the rest of the cranium. White, opaque scar tissue tends to grow on implanted cranial windows (Schendel et al., 2013), to avoid this 20 µl of dexamethasone (2 mg/ml Dexamethasone, Rapidexon, Dechra Veterinary Products) was applied to the dural surface (Park et al., 2015). A portion of a sterile glass coverslip (No. 0 cover glass, Menzel-Gläser), manually trimmed with a diamond-tipped glass cutter to closely fit the edges of the craniotomy, was lightly pressed into position with the #5 forceps. Any remaining liquid was removed from the headplate well, and the edges of the cranial window sealed by applying small amounts of cyanoacrylate adhesive (Super Glue Power Flex Gel, Loctite) around the edges with a hypodermic needle (Figure 4.2). Post-operative care was performed in the same manner as described in Section 3.2.2.

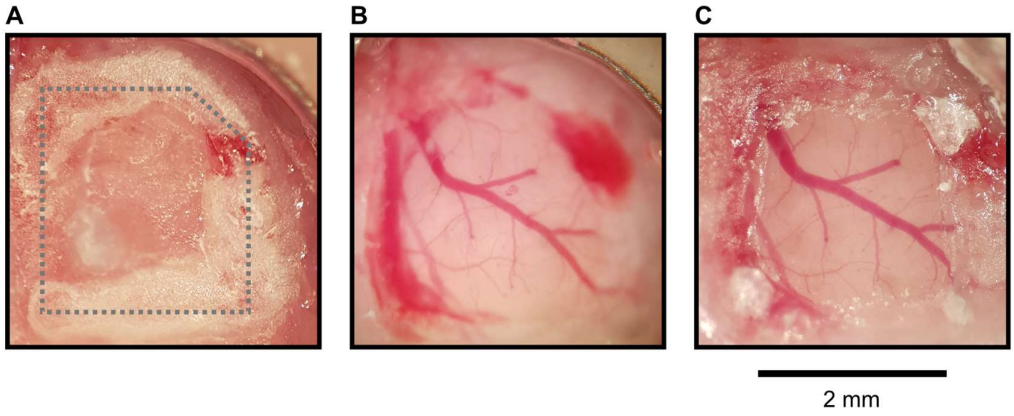

*Figure 4.2: Placement of a cranial window over $M1_{FL}$. **A)** Cranial surface of a mouse with the planned outline of a craniotomy etched onto the bone (dotted grey line). **B)** The same area after the outlined area of bone has been removed. **C)** A glass cranial window was fitted over the craniotomy and the edges sealed with cyanoacrylate adhesive. Note, minimal blood under the glass coverslip and the pial blood vessels are clearly visible indicating successful window implantation.*

4.2.4 Population calcium imaging during behaviour

Two-photon calcium imaging was performed 24 hrs after cranial window surgery, and repeated daily until connective tissue growth made the cranial windows too opaque to for calcium imaging at the desired depth. Mice were head-restrained in the lever set-up

configured for Stage 3 of our behavioural task (as described in Section 3.2.3), and the cranial window positioned directly under the objective lens of the two-photon microscope (40× water immersion lens, 0.80 NA, 3.5 mm working distance, Nikon). The headplate well and cranial window were cleaned by lightly wiping with a cotton swab soaked in 70% ethanol, then dried. The headplate well was then slightly overfilled with distilled water and the objective lens lowered into the water. GCaMP6s was excited using a Ti:sapphire pulsing laser (Chameleon Vision S, Coherent Inc.; <70 fs pulse width, 80 MHz repetition rate) set to deliver light at 920 nm, and emitted light was recorded with a gallium arsenide phosphide (GaAsP) photomultiplier tube (PMT). LotosScan 1.4 software (Beijing ABORO-Tech Co., Ltd.) was used to view live digitised output from the PMT. Initially, the imaging plane focused on the dural surface before being lowered to 500-650 µm below the surface to record from a field of view within layer 5B.

After ~ 5 minutes of habituation to the head restraint, the lever was unlocked and Stage 3 of the behavioural task was initiated. Images (600×600 pixels, corresponding to 372×372 µm) were acquired at 40 Hz using LotosScan 1.4 as .tdms files, in 5 minute blocks. Digital signals documenting parameters of the lever task, and infrared digital videos (described in Section 3.2.3) were continuously recorded during each two-photon imaging block at 60 frames per second. Each successive 5 minute recording block was acquired sequentially, minimising the inter-block interval and each imaging session contained on average 3-6 recording blocks (mean 4 recording blocks, i.e. 20 mins per imaging session).

4.2.5 Offline processing of calcium imaging data

For two-photon imaging data, the fluorescence of a region (in the context of this thesis, a neuronal cell body) at time point t (F_t) is conventionally expressed in terms of how much it differs from baseline fluorescence (F_0), divided by the baseline fluorescence:

$$\frac{F_t - F_0}{F_0}$$

Or in short, ΔF/F (Macleod, 2012) as a measure of neuronal activity. Before two-photon imaging data can be interpreted in terms of ΔF/F, it has to be processed offline in several stages. These can be broadly grouped into three steps, performed on every imaging field of

view: 1) motion correction, 2) the identification of regions of interest (ROIs), and 3) signal extraction. Each step was partially automated using a combination of custom-written ImageJ (National Institutes of Health), MATLAB (MathWorks) and Python (Python Software Foundation) scripts. The code developed in-house for offline processing of calcium imaging data was written by Drs Julian Ammer, Stephen Currie, Sander Keemink, Janelle Pakan, and Premchand Brian.

Two-photon recordings during behaviour often had visible movement artefacts as the brain moved with respect to the objective lens, especially during the execution of forelimb movements. In contrast, when imaging the surface of the cranial window movement artefacts were not visible, suggesting that the headplate and cranial window remained fixed in position. Any movement along the Z-axis would result in the plane of focus changing which is not correctable, thus fields of view with visible movement along the Z-axis were excluded from further analysis. To correct for movement artefacts along the X- and Y-axes, the remaining fields of view were converted from .tdms to .tif format, and processed with the motion correction functions of Sequential IMage Analysis (SIMA), an open source Python package developed by the Losonczy Lab (Kaifosh et al., 2014).

After motion correction, videos were manually reviewed to determine if motion correction was successful. Fields of view which were not successfully motion-corrected were excluded from further analysis. Each video was down sampled to 0.5 Hz to improve signal-to-noise, and regions of interest (ROIs) were then drawn in ImageJ over visually identified neuronal cell bodies (Figure 4.3), either manually by creating polygons or with the Cell Magic Wand plugin (Walker, 2014). If neurons overlapped, ROIs were drawn in a manner that excluded the overlapping region.

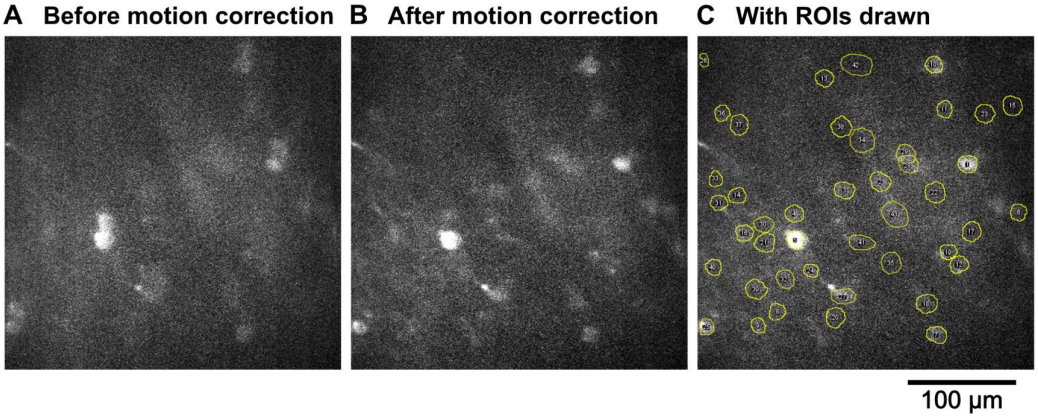

Figure 4.3: Two-photon images before and after motion correction. ***A)*** *A sample portion of an L5B recording, with 80 consecutive frames (i.e. 2 seconds of recording) summed into a single image. As there was movement within the 2 s (a ~15 µm shift, approximately along the Y-axis), features such as neuronal cell bodies appear blurred, with ghosting artefacts present.* ***B)*** *Motion correction eliminates the blurring and ghosting artefacts caused by movement.* ***C)*** *Same motion-corrected frame with regions of interest (ROIs) drawn around identified neuronal cell bodies. Not all the identified cell bodies are visible within this image as it is a 2 s truncated version of a 30 minute recording.*

After ROIs were drawn over identified neuronal somata, signal extraction was performed to extract the ΔF/F time series for each ROI. However, there is always some degree of light scattering in microscopy, and the fluorescence values in each ROI can be influenced by fluorescence near the ROI, for example nearby cell bodies and the surrounding neuropil. Hence, the Fast Image Signal Separation Analysis (FISSA) toolbox was employed to decontaminate calcium signals (Figure 4.4) (Keemink et al., 2018). FISSA automatically generates 4 regions around every ROI (termed 'neuropil regions'), then performs non-negative matrix factorisation (NMF) on the ROI and neuropil regions to de-mix the time series of somatic fluorescence signals, i.e. F_t. Baseline fluorescence (F_0) was then derived for each ROI by taking the lowest 5th percentile of the smoothed F_t (1 Hz low-pass, zero-phase, 60th-order FIR filter) across the entire imaging session. With F_t and F_0 found for each ROI, ΔF/F was then calculated as described previously.

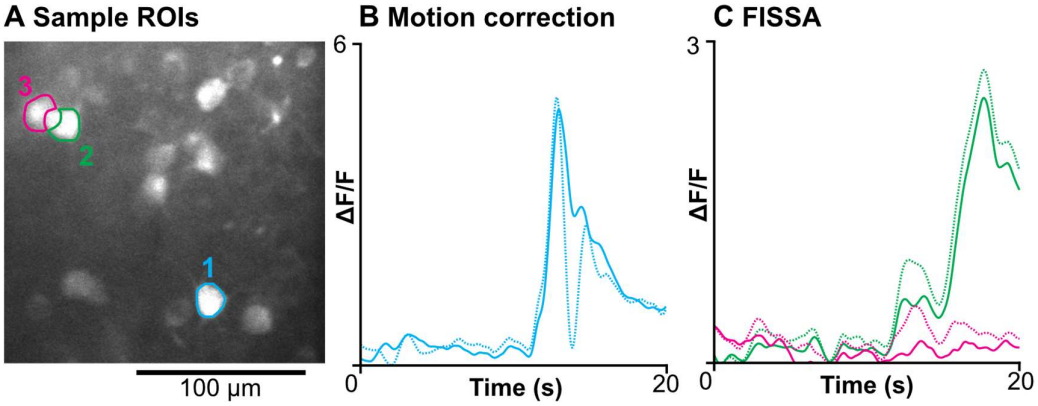

Figure 4.4: Effects of post-processing on ΔF/F. ***A)*** *A portion of a field of view, with 3 neuronal somata highlighted as regions of interest (ROIs). ROIs 2 and 3 have been drawn over non-overlapping portions of the underlying neurons.* ***B)*** *A portion of ROI 1's ΔF/F time series, without (dotted cyan line) and with (cyan line) motion correction. Movements of the imaging frame would at times move the cell partially or fully out of the ROI, leading to inaccurate ΔF/F measurements (for example, see rapid decrease ΔF/F at ~12s) .* ***C)*** *A portion of the ΔF/F time series of ROIs 2 and 3 in green and magenta, respectively, without (dotted lines) or with (solid lines) FISSA applied. Motion correction was applied for all traces in graph C. Due to both ROIs being in close proximity, light scattering from one ROI leads to 'bleed-through' into the other, thus the de-mixed ΔF/F signal extracted by FISSA tends to be lower in magnitude. All ΔF/F time series were smoothed with an 80-frame-wide loess filter.*

After completing the steps above, each ROI had a ΔF/F time series that spanned the entire behavioural session. Time series corresponding to parameters of the lever task (described in Section 3.2.3) were resampled to 40 Hz and aligned with the ΔF/F time series. Therefore, behaviourally relevant time points, especially the onsets of successful push and pull actions, could be located in the ΔF/F time series. Subsequent analyses in this chapter and following chapters used this alignment to measure ΔF/F values of each ROI *before* and after push/pull movement onsets.

4.2.6 Motion index calculation

In order to determine if non-task related movements were correlated with changes in fluorescence, we recorded videos of mouse behaviour using a moderate frame rate (60 fps) infrared camera. All videos were analysed offline and a "motion index" – a measure of frame-to-frame differences in pixel intensities – was used to quantify non-task-related movements.

This metric has been previously used to quantify the magnitude of mouse movements during electrophysiological recordings (Jelitai et al., 2016; Puggioni, 2015; Schiemann et al., 2015).

To measure motion index, a single rectangular ROI was drawn around the forelimb region in each video recording (Figure 4.5). A custom-written MATLAB script then calculated the motion index of each frame in that ROI. Motion index was calculated by reading each frame of the greyscale video as a matrix of 8-bit numbers, with each element in the matrix corresponding to the intensity of the corresponding pixel. First, the portion of the matrix corresponding to the ROI was isolated, then a matrix of "pixel differences" derived by subtracting the ROI matrix of each frame from the ROI matrix of the previous frame. The matrix of "pixel differences" was then multiplied by itself to create a Hadamard product. The motion index of each frame was then calculated by adding together every element in the Hadamard product, and dividing that value by the number of elements in the matrix (i.e. mean value). Figure 4.5 below graphically demonstrates how motion index was derived.

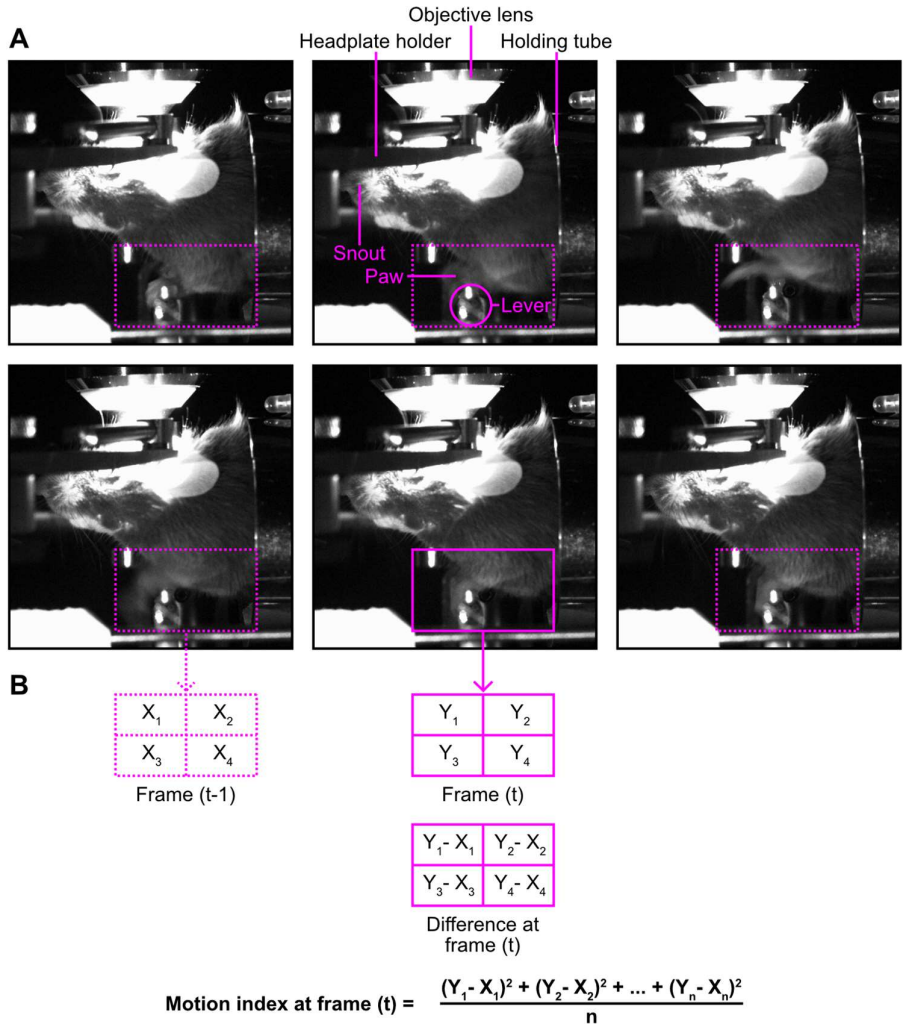

Figure 4.5: Derivation of a motion index metric from sequential video frames. ***A)*** *Six consecutive frames recorded during mouse behaviour. The bright structure above the mouse is the objective lens of the two-photon microscope. The objective lens and the mouse's head appear bright due to the 920 nm infrared laser used for two-photon excitation being visible in the infrared video recording. The magenta box depicts the region of interest (ROI) used for motion index calculation. In this example, the mouse lifts its left forepaw off the lever and returns it to the lever within six frames, the entire movement taking < 0.1 s (video acquisition rate = 60 Hz).* ***B)*** *Calculation of motion index assuming that the ROI contained only 4 pixels. Actual motion index calculations were performed on every pixel within the forelimb ROI (i.e. a matrix representing 170-by-300 pixels).*

Since the videos used for motion index measurements were initiated prior to calcium imaging, the start of each 2-photon recording could be identified by locating the frame at which there was a sharp increase in brightness when the laser shutter opened and two-photon imaging commenced. The motion index time series was then resampled from 60

frames per second to 40 frames per second (i.e. 40 Hz) to match the sampling frequency used for calcium imaging.

4.2.7 Linear mixed-effects models involving ΔF/F, action type and motion index

The main goal of this project is to investigate if and how different actions (pushes and pulls) are represented in the primary motor cortex. However, it has long been known that any arbitrary limb movement has some degree of neural representation in the motor cortex (Kakei et al., 1999; Oby et al., 2012), and given that we frequently observed forelimb movements prior to the onset of cued movements (see Section 4.3.2) it became necessary to determine if non-cued movements could affect our ability to isolate cued movement changes in fluorescence (Figure 4.6).

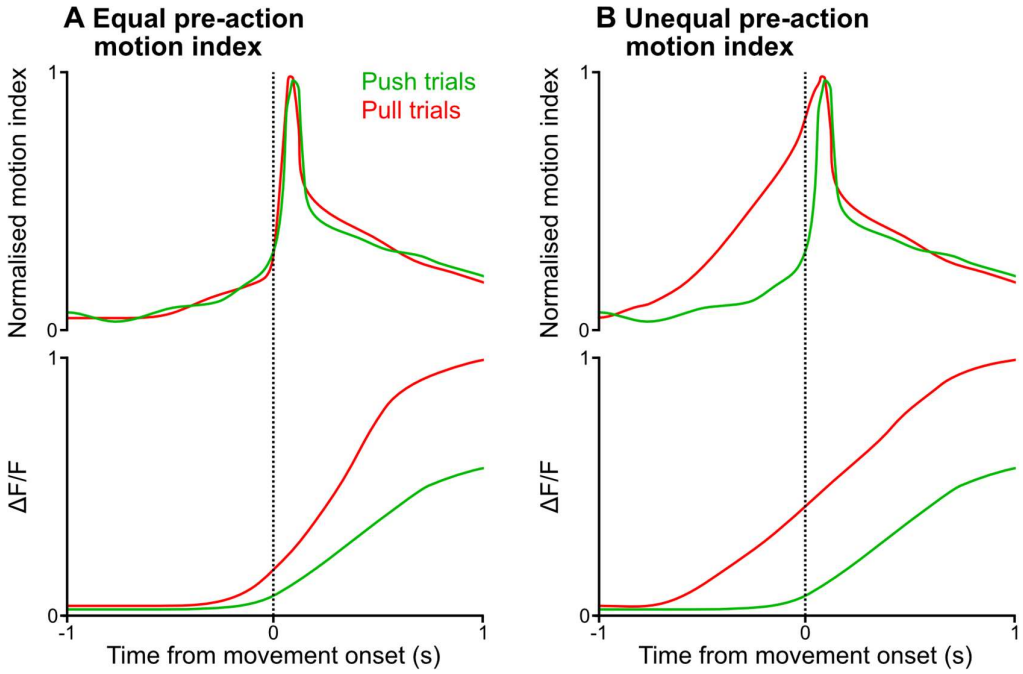

Figure 4.6: Illustration of how differences in motion index could complicate the interpretation of ΔF/F changes. The graphs here are illustrations and not actual recorded data. ***A)*** *Top: the mean motion index time series of a mouse across all push (green) and pull (red) trials. Bottom: mean ΔF/F time series from an example neuron across all push (green) and pull (red) trials.* ***B)*** *Another example neuron, but with a significantly higher pre-pull motion index.*

For the neuron depicted in **B)**, does the higher post-pull ΔF/F reflect action-specific coding? Or does its activity not encode action type at all, but instead encode any forelimb movement, with the higher post-pull ΔF/F reflecting increased pre-action forelimb movement? In order to determine if pre-action motion index influenced action-related ΔF/F, and whether action type (i.e. push or pull) or motion index was a better predictor of ΔF/F, linear mixed-effects models (LMEs) were constructed and compared against each other (Figure 4.7). Each observation (structured as a line in a data table) corresponded to a ROI during a successful action. An observation would include the FOV the action came from, the ROI, the action type (push or pull), the mean motion index from -1 s to 0 s and the mean ΔF/F of the ROI from 0 s to 1 s with respect to the start of the action. The start of an action was defined as the time point at which the lever moved away from the back sensor (for a push) or the front sensor (for a pull). Each identified ROI was assigned a unique number, i.e. the first ROI in the first field of view was not assigned the same number as the first ROI in the second field of view.

ΔF/F (Dependent variable)	**FOV (Random effect)**	**ROI (Random effect)**	**Action type (Dummy variable)**	**Motion index (Fixed effect)**
0.18	1	1	Push	7.1
0.56	1	1	Push	13.4
…	…	…	…	…
0.09	13	566	Pull	22.6
0.15	13	566	Pull	16.6

Figure 4.7: Data structure used for linear mixed effects model analysis. The numbers in the table are from the actual dataset used, except that the full table had 25,510 lines, i.e. 25,510 unique observations.

LMEs were coded, processed, and compared against each other using MATLAB. The Akaike information criterion (AIC) was used to compare the quality of the models. Further description and analysis of these models are available in the results section.

4.2.8 Quantification of neuronal cell density

To derive a 'ground truth' measure of neuronal density in L5B that could be compared against the density observed during two-photon imaging, $M1_{FL}$ sections were immunostained with a neuron-specific antibody and imaged with confocal microscopy. Anti-NeuN was selected as the primary antibody, as NeuN is a pan-neuronal marker specifically expressed in neurons (Gusel'nikova and Korzhevskiy, 2015; Mullen et al., 1992).

After two-photon imaging was complete, mice were transcardially perfused with paraformaldehyde as described in Section 2.2.4, but instead of 60 µm coronal slices, 30 µm horizontal slices were cut parallel to the surface of $M1_{FL}$.

1) For the initial washing and blocking step, sections were rinsed in phosphate-buffered saline (PBS, containing 64.6 mM Na_2HPO_4, 19.7 mM $NaH_2PO_4 \cdot H_2O$, 15.4 mM NaCl in distilled water, with pH adjusted to 7.4) overnight, incubated with a blocking solution (PBS, with 0.5% Triton X-100 (Sigma-Aldrich) and 10% goat serum (Sigma-Aldrich)) for 2 hrs, then rinsed with PBS.
2) For primary antibody binding, sections were incubated overnight with mouse anti-NeuN (MAB377 Anti-NeuN Antibody, clone A60, Merck) diluted 1:1500 in carrier solution (PBS, with 0.5% Triton X-100 and 1% goat serum), then rinsed with PBS.
3) For secondary antibody binding, sections were incubated overnight with a secondary antibody (Goat anti-Mouse IgG (H+L) Cross-Adsorbed Secondary Antibody, Alexa Fluor 568, Invitrogen) diluted 1:750 in carrier solution then rinsed with PBS.
4) Finally, sections were mounted onto glass slides, briefly air-dried, covered with VECTASHIELD Antifade Mounting Medium (Vector Laboratories), and sealed with a glass coverslip. All immunohistological procedures were performed at room temperature, then the slides stored at 4 °C.

Images of $M1_{FL}$ (1024×1024 pixels, corresponding to 627×627 µm) were acquired using a Nikon A1R FLIM confocal microscope, (20× objective lens, 0.8 NA, Plan Apo VC, Nikon) with the appropriate excitation laser and filters for Alexa Fluor 568. Three images were taken at imaging planes corresponding to layer 5B (550 µm). The number of cells in each image was manually counted, and then divided by the total area of the image to obtain a measure of neuron density.

For most fields of view (FOVs) recorded during calcium imaging, neurons were not visible in all portions of each frame. This was for a number of reasons, such as blood vessels occluding the excitation light and the intensity of GCaMP6s labelling being reduced as a function of distance from the centre of the virus injection. By dividing the number of observed neurons by the total imaging area would therefore underestimate the density of neurons. Instead, the area in each FOV that had visible neurons was estimated, by manually drawing a polygon around all identified neurons. The neuronal density of a field of view was then calculated by dividing the number of neurons by this area.

4.2.9 Quantification of GCaMP6s labelling

Histological procedures were performed on a cohort of mice to determine the accuracy and spread of virus injections within the cortex. After completion of all imaging sessions, mice were transcardially perfused with paraformaldehyde, whereupon the brain was removed and cut into 60-µm-thick coronal sections. Each section was then mounted on a glass slide as described in Section 2.2.4. Images of each section were acquired using a Leica DM R epifluorescence microscope. For each mouse, the anatomical coordinates of the injection site (taken as brightest location of GCaMP6s labelling), then the mediolateral and dorsoventral extents of GCaMP6s labelling, were measured for each injected brain.

4.3 Results

4.3.1 L5B neuronal activity during the execution of push-pull lever sequences

This project is focused on the differences in neural activity between push and pull trials, so measures of motion index (MI) and ΔF/F were aligned to the start of successful movements. A total of N = 11 fields of view and corresponding MIs were recorded from 7 mice. The ΔF/F from each ROI and corresponding MI traces were temporally-aligned to the onset of cued movements (Figure 4.8). A further 4 fields of view were imaged, but either had no infrared video, or the infrared videos could not be temporally aligned to calcium imaging data.

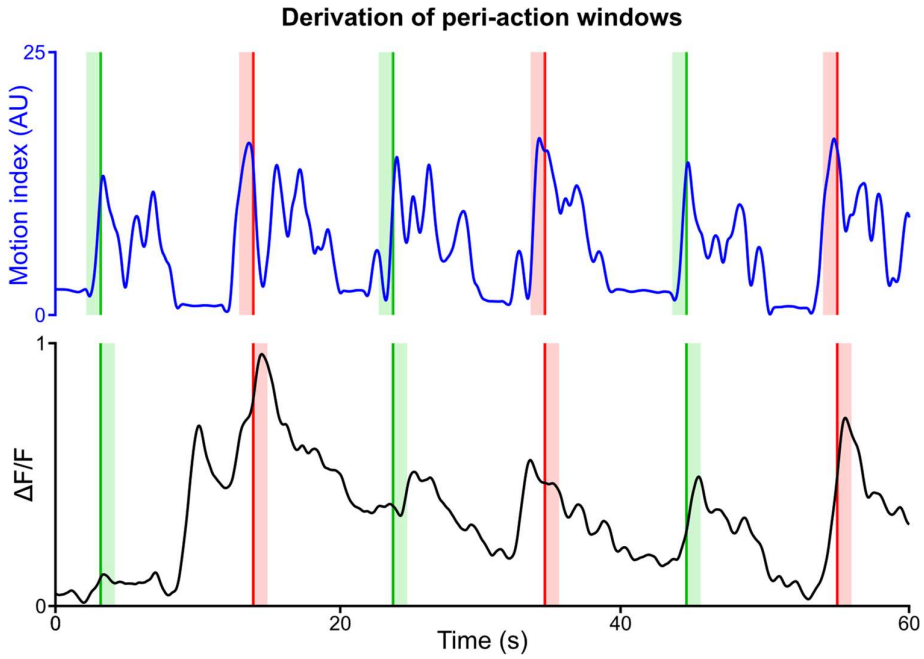

Figure 4.8: Derivation of peri-action windows. This graph displays a typical 60-second-wide window of ΔF/F and motion index data recorded during behaviour. The mean motion index (blue line) and ΔF/F (black line, representing the fluorescence changes of a single ROI) were measured around the time points of rewarded actions (green lines = push trials, red lines = pull trials). The red and green vertical lines depict push and pull movement onsets, respectively. A window spanning -1 s to 0 s with respect to each action onset was used to calculate mean pre-action movement index, and a window spanning 0 s to +1 s with respect to each action onset was used to quantify the ΔF/F of each ROI.

4.3.2 Relationship between motion index and ΔF/F

We sought to determine if MI was significantly different between push and pull trials, and if these differences in MI influenced the activity recorded in L5B neurons. Having derived contemporaneous time series of ΔF/F, lever movements and MI, MI was aligned to the onset times of successful pushes and pulls in each of the N = 11 fields of view (FOVs). It was apparent that during many of the FOVs, MI prior to rewarded pulls was not the same as MI prior to rewarded pushes (Figure 4.9).

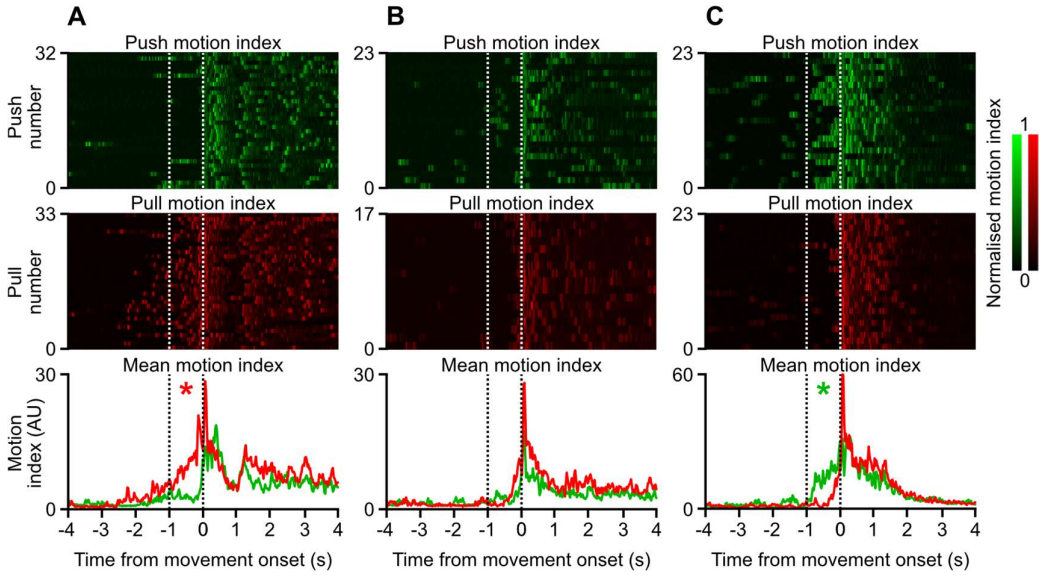

Figure 4.9: Motion index profiles during behaviour. ***A), B)*** *and* ***C)*** *are represent motion indices measured during the recording of 3 calcium imaging FOVs in different mice. The top panels are heat maps of normalised MI during push trials aligned to movement onset. The dotted lines indicate the -1 s to 0 s window which was used to measure pre-action MI. The middle panels are heat maps of normalised motion index during push trials aligned to movement onset. The bottom panels are plots of mean MI for push trials (green) and pull trials (red). The asterisks indicate whether MI was higher during pre-push or pre-pull periods (Welch's unequal variances* t*-test, two-tailed).*

Welch's unequal variances *t*-test (two-tailed) was performed on the -1 s to 0 s pre-action bin for each of the 11 FOVs. During the imaging of some FOVs like **B)**, pre-action MI was not significantly different between push or pull trials (d.f. = 38, $p = 0.26$). For others, MI was significantly higher during the pre-pull period (e.g. **A)**, d.f. = 63, $p < 0.001$), or during the pre-push period (e.g. **C)**, d.f. = 44, $p < 0.001$). In total, 4 FOVs had significantly ($p < 0.05$) higher

motion index during pre-push periods, 2 FOVs had significantly ($p < 0.05$) higher motion index during pre-pull periods, and 5 FOVs had statistically insignificant differences between pre-push and pre-pull periods.

4.3.3 Linear mixed-effects model analysis of action type and motion index

As motion index during the pre-action periods was significantly different in 55% of calcium imaging FOVs, LMEs were created to examine whether motion index was a good predictor of ΔF/F. Three LMEs were generated in MATLAB. In Wilkinson notation, the models were:

$\mathbf{1}) \; \Delta F/F \sim (1|FOV) + (ActionType|ROI) + (MotionIndex|ROI)$

$\mathbf{2}) \; \Delta F/F \sim (1|FOV) + (MotionIndex|ROI)$

$\mathbf{3}) \; \Delta F/F \sim (1|FOV) + (ActionType|ROI)$

Models **2)** and **3)** are nested within model **1)**. As ROIs were inherently grouped by FOV and not truly independent of each other, "FOV" was used as a grouping variable with a random effect intercept. It would not be reasonable to assume that different ROIs (i.e. different neurons) would have the same response to changes in motion index or action type, so ROI-specific random effects were included in the terms "ActionType" and "MotionIndex".

As the effects of "ActionType" and "MotionIndex" were modelled on a per-ROI basis, the individual slopes and intercepts for the (ActionType|ROI) and (MotionIndex|ROI) terms are not very informative. Nevertheless, model comparison techniques can be employed to contrast the relative quality of each model, to quantify the relative contributions of "ActionType" and "MotionIndex" to ΔF/F. I decided to use the Akaike information criterion (AIC), which evaluates the relative goodness of fit and simplicity of models (Akaike, 1974). The AIC is a logarithmic measure that increases with the sum of squared errors of prediction (SSE) remaining after model fitting, and with the complexity of the model. Lower AIC values indicate higher relative model quality. To determine if including the terms (ActionType|ROI) and (MotionIndex|ROI) improved model **1)**, the Akaike information criterion (AIC) of each model was calculated with MATLAB (Figure 4.10).

Model	1), all terms	2), no ActionType	3), no MotionIndex
Degrees of freedom	9	6	6
Log likelihood	-9634	-9673	-9654
AIC value	19285	19358	19320

*Figure 4.10: Model comparison using the AIC metric. Model **1)** had the lowest AIC, indicating that the inclusion of both the ActionType and MotionIndex terms improved the quality of the model. Model **3)** had a lower AIC than model **2)**, indicating that a model which did not consider ActionType had a lower quality than a model which did not consider MotionIndex.*

The likelihood ratio test was also applied to compare each pair of models. Model **1)** was found to be better than **2)** and **3)**, and model **3)** better than model **2)** ($p < 0.001$ for all three tests). Since model **1)** was better than model **3)**, we can conclude that pre-action motion index does provide information on action-related ΔF/F, i.e. it most likely causes differences in action-related ΔF/F. Similarly, since model **1)** was better than model **2)**, it is also conclusive that action type provides information on action-related ΔF/F. However, model **3)** was significantly better than model **2)**, indicating that the variance in post-action ΔF/F was explained far better by action type than by the variation in MI. In sum, pre-action movement did have an effect on action-related ΔF/F, but the impact of such movement action was far smaller than the effect of movement direction on action-related ΔF/F. Most of the differences between push- and pull-related ΔF/F changes were related to the difference in movement direction, not differences in pre-action MI.

4.3.4 Average neuron density in L5B of primary motor cortex

To determine whether L5B calcium imaging experiments sampled data from the whole population or sampled a fraction of the total population, sections of $M1_{FL}$ were stained for NeuN and the total neuron density measured (Figure 4.11). The average neuronal density in L5B was calculated by counting NeuN positive cells from n = 3 sections of a mouse brain. This value was then compared to the average density of GCaMP6s positive cells acquired from n = 15 different fields of view acquired during 2P calcium imaging from N = 7 mice.

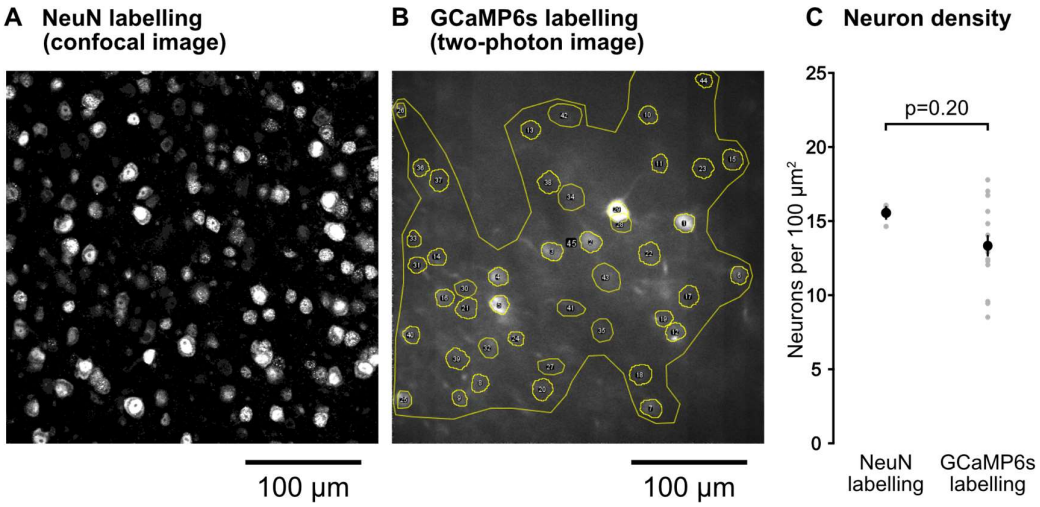

Figure 4.11: Neuron density in L5B. ***A)*** *A sample confocal image of L5B neurons stained with an anti-NeuN antibody and a secondary goat anti-mouse fluorescent secondary antibody.* ***B)*** *A sample 2-photon image of L5B neurons expressing GCaMP6s. The yellow circles are ROIs drawn around identified neuronal cell bodies, while the large yellow outline is an estimation of the area where neurons are present. This correction was necessary as certain areas within each field of view were obstructed by overlying blood vessels. This resulted in visibly darker regions where cell bodies were absent. If an area correction method had not been implemented the final cell density calculations would represent an underestimation of the total neuronal density.* ***C)*** *Average L5B neuronal density measured using NeuN and GCaMP6s labelling.*

The neuronal density of L5B as measured by NeuN labelling was 15.6 ± 0.5 neurons per 100 µm^2, while the neuronal density measured by GCaMP6s labelling was 13.3 ± 0.7 neurons per 100 µm^2 (mean ± s.e.m.). However, this difference was statistically insignificant (d.f. = 16, p = 0.20, two-sample *t*-test), indicating that two-photon imaging FOVs adequately sampled $M1_{FL}$ L5B population activity.

4.3.5 Distribution of GCaMP6s labelling

Histology was used to confirm the reliability of virus injections by observing if the coordinates of central $M1_{FL}$ (1.6 mm lateral and 0.6 mm rostral from bregma) were successfully labelled with GCaMP6s. While all virus injections were targeted to the same coordinates, there is always some degree of anatomical variation and imprecision during surgery. In addition, viral labelling *in vivo* can be variable, and there is no guarantee that a given concentration and

volume of virus will produce a consistent spread of neuronal labelling. Thus, histology was used as an independent measure to verify our virus injection coordinates.

N = 16 mice injected with GCaMP6s were perfused, sectioned and imaged to determine the distribution of GCaMP6s labelling in $M1_{FL}$. In each brain, the anatomical coordinates of the apparent centre of GCaMP6s-labelling at 600-µm-deep was recorded, as well as the width of labelling measured parallel to the cortical surface (Figure 4.12). GCaMP6s labelling tended to spread across a large area of L5B (900-1900 µm wide). The centre of labelling tended to be somewhat medial and caudal compared to the centre of $M1_{FL}$ (1200-1600 µm lateral from bregma, 60-600 µm rostral from bregma), but central $M1_{FL}$ was successfully labelled in every brain due to the large spread of GCaMP6s labelling.

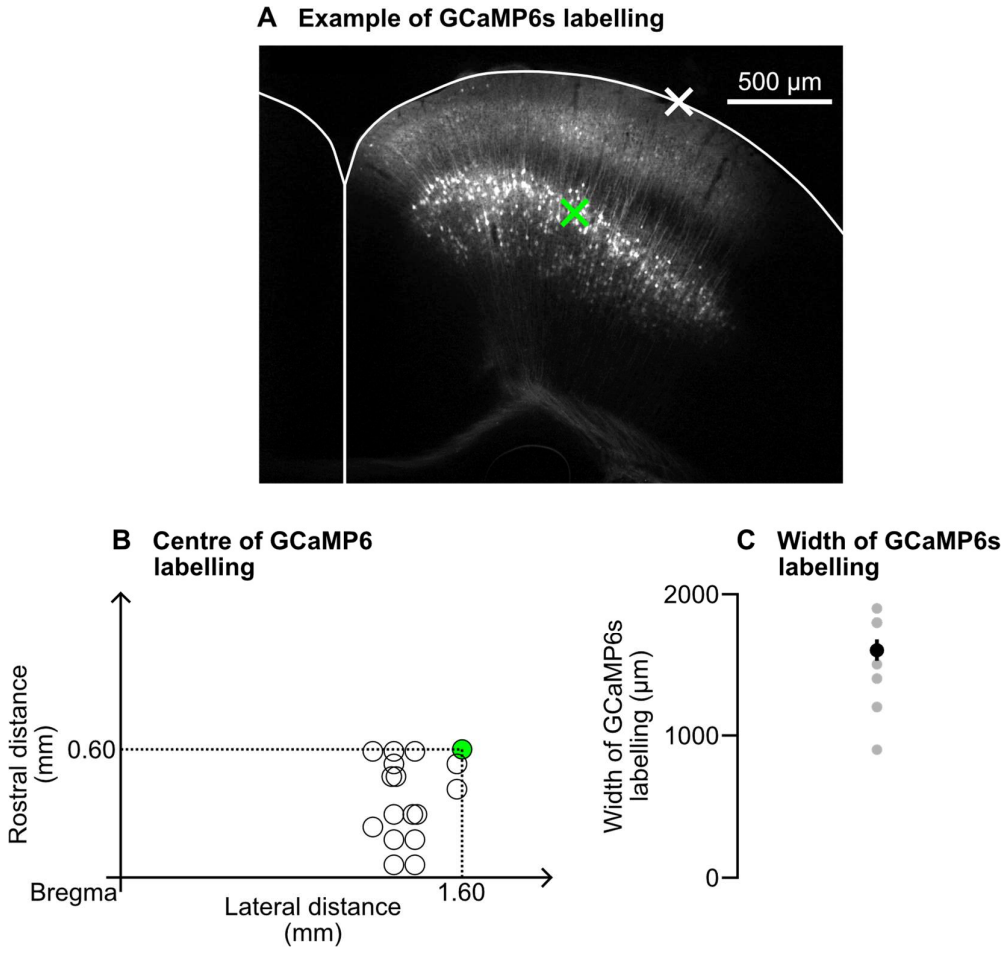

*Figure 4.12: Distribution of GCaMP6s labelling in $M1_{FL}$. **A)** A representative GCaMP6s-labelled coronal section at the anatomical coordinates of central $M1_{FL}$. The white cross indicates the*

centre of $M1_{FL}$ at the surface (i.e. 1.6 mm lateral and 0.6 mm rostral from bregma). The green cross indicates the centre of GCaMP6s labelling which tended to be more medial and caudal compared to the virus injection target. ***B)*** *Table indicating the centres of GCaMP6s labelling for N = 16 mice. All of these points were within 620 µm of central $M1_{FL}$.* ***C)*** *Width of GCaMP6s labelling in L5B across all mice (N = 16 mice). The measurements for individual mice are plotted in grey, while the mean and s.e.m. are plotted in black. The narrowest observed spread of GCaMP6s labelling was 900 µm, therefore the target at central $M1_{FL}$ (1.6 mm lateral, 0.6 mm rostral from bregma) was labelled in all mice.*

4.4 Discussion

This chapter illustrates the potential pitfalls in the acquisition and interpretation of calcium imaging data acquired in L5B of cortex during behaviour, and the measures put in place to address these issues.

4.4.1 Relationship between motion index and ΔF/F

One major concern with the interpretation of action-related neuronal activity is the confounding effect of non-action related movements. If FOVs contain significantly different levels of pre-push and pre-pull movements, and changes in ΔF/F are related to all forelimb movement (which is to be expected in $M1_{FL}$) (Hira et al., 2013a; Puggioni, 2015; Tennant et al., 2011), then any differences between push- and pull-related neural activity might be explained by differences in the magnitude of pre-action movement rather than the execution of the action itself. Analysis of the behavioural videos revealed that mice did indeed display different levels of pre-push and pre-pull movement during many imaging sessions. To try and account for this possible confound, we developed a robust statistical method to investigate the extent to which differences in motion index contributed to changing ΔF/F values during the execution of the cued lever movements.

Early attempts involving linear regression or Spearman's rank correlation to compare the time series of motion index and ΔF/F were found to be inappropriate, as GCaMP6s has nonlinear and time-dependent dynamics that stymied pointwise calculations (Chen et al., 2013b). Ultimately, the data binning approach described earlier in this chapter was chosen for two reasons. Firstly, binning motion index ΔF/F in 1 s windows reduced the difference between the time-scales of mouse movement as measured by motion index (on the order of 0.1 s) and neuronal calcium transients (on the order of seconds). Secondly, selecting bins around the time points of successful actions ensured that our measures of movement and neuronal activity were temporally close to the actions (pushes and pulls).

Next, a model was required to meaningfully investigate our multidimensional dataset. However, there is currently no widely-accepted model in the field that describes how movement is related to neuronal ΔF/F in $M1_{FL}$. We constructed several linear mixed-effects

models as approximations of neural coding. While these models are simplified approximations of neural coding in $M1_{FL}$, which is almost certainly non-linear in nature and represents far more information than what was included in the models, they were nonetheless able to provide informative insights into the relationship between movement and L5B neuronal activity.

We found that including both MI and action type improved the strength of an LME predicting ΔF/F. However, an LME including information on action type performed far better than an LME which included MI alone. This indicates that motion index indeed predicted ΔF/F to some degree, but action type was a far better predictor of ΔF/F. If instead, ΔF/F was mainly influenced by motion index, we should find that the model including motion index but not action type performed better. Thus, action type is encoded in neuronal ΔF/F in a manner than does not merely reflect differences in pre-action motion index.

In summary, our findings suggest that experiments involving motor behaviour should consider the effects of the non-task-related movements that may occur prior to cue-driven movements. While many contemporary studies involving mouse forelimb behaviours incorporate some form of infrared video recording and motion tracking, most focus only on limb movements that occur after the onset of a trial. Such an approach could potentially miss the confounding effect of pre-task movements on neural activity.

4.4.2 Neuron density and GCaMP6s expression in L5B

Despite the recent explosion of publications which study population calcium imaging in mice, there is a remarkable paucity in the documentation of layer-specific neuronal density in mouse cortex. Nonetheless, I believe that measurements of layer-specific neuronal density are important, especially in the context of deep-layer imaging in L5B where signal-to-noise ratios can be lower than in upper cortical layers. While current population calcium imaging techniques preclude recordings from all neurons within a cortical area, it should be empirically confirmed if a representative fraction of the neuronal population has been sampled: if the observed neuronal density during population imaging is significantly lower than the expected neuronal density, the discrepancy should be accounted for otherwise there remains the possibility that a sampling bias could be introduced that may confound

interpretations of experimental results. The observed neuronal density in L5B of $M1_{FL}$ during calcium imaging was not significantly different from the measured neuronal density measured immunohistochemically, thus such confounds can be safely rejected for my L5B calcium imaging results.

In addition, the significant spread of viral transfection ensured that each injection sufficiently labelled a large proportion of $M1_{FL}$ L5B neurons with GCaMP6s. We confirmed that the AAV and associated injection techniques were able to reproducibly and consistently produce GECI expression in our area of interest.

Chapter 5: Population activity in Layer 5B of mouse forelimb motor cortex

5.1 Introduction

The overarching goal of this doctoral thesis was to investigate how L5B neurons in $M1_{FL}$ of mice encode different actions. Having quantified the laminar depth of L5B within $M1_{FL}$ in Chapter 2, established a cued push/pull behavioural task in Chapter 3, and validated our experimental approach of population calcium imaging during behaviour in Chapter 4, this chapter will describe the neural correlates of forelimb push and pull movements in L5B.

5.1.1 Population coding of diametrically opposite movements in primates

Given a classical centre-out directional reaching task, directional sensitivity has been demonstrated in a remarkably diverse set of experimental settings in both humans and primates. Many measures of M1 neuronal activity demonstrate directional preference, including multi-unit recordings in primates, human and non-human primate local field potentials (LFPs) and functional magnetic resonance imaging (fMRI) (Fabbri et al., 2010; Georgopoulos et al., 1982; Mehring et al., 2004; Schwartz, 1994; Toxopeus et al., 2011). If mouse motor cortex encodes directional movement in a similar manner, then we would expect M1 neurons to display similar activity patterns: producing higher spike rates during movements in their preferred directions when compared to movements in non-preferred directions.

Other forms of orientation-specific coding have been found in many other mammalian cortical regions. Individual neurons in the primary visual cortex respond to preferred orientations of visual gratings, and this phenomenon has been demonstrated in many mammalian species including cats, primates and mice (Hubel and Wiesel, 1959; Niell and Stryker, 2008; Skottun et al., 1991). Neurons in the hippocampus and entorhinal cortex of rats encode spatial trajectories during voluntary locomotion (Frank et al., 2000), and neurons

in the primate lateral prefrontal cortex encode direction-specific short-term memories of moving visual stimuli (Mendoza-Halliday and Martinez-Trujillo, 2017). Direction coding is therefore a recurring motif in many forms of mammalian neural coding.

While most experiments involving directional sensitivity in motor cortex have involved a centre-out reaching task with targets arranged in a two-dimensional plane, primate M1 neurons encode movement vectors in 3D-space (Georgopoulos et al., 1988), with the appearance of 2D directional preference being a result of 3D tuning curves projected onto a 2D task space. Despite this dimensionality reduction, the majority of neurons demonstrate some degree of directional preference in reaching tasks with a 2D target arrangement (Fu et al., 1995; Georgopoulos et al., 1982). This is not an unexpected phenomenon: points located at the edge of a 2D circle constitute a subset of points on the surface of a 3D sphere, and as long as the preferred directions of individual neurons are arranged in a reasonably uniform manner, 2D directional preference will emerge (Georgopoulos et al., 1988). Extending the logic of dimensionality reduction, a 1D line is merely a degenerate 2D circle, so if the same assumptions hold, neurons in M1 should differentially encode push versus pull movements, as these two forelimb motions are collinear but in opposite directions (Figure 5.1).

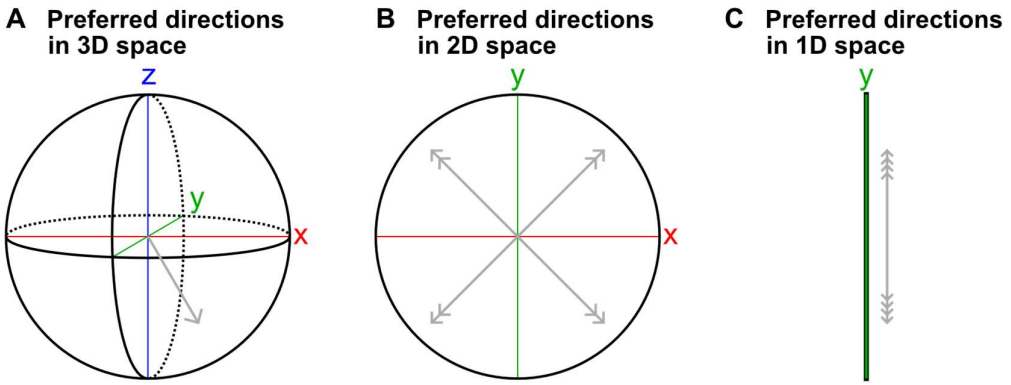

Figure 5.1: Illustration of how 3D directional preference can be perceived as directional preference in lower dimensions. ***A)*** *As an extreme example, assume there are 8 neurons in M1, each with a directional preference in 3D space (represented by the x-, y- and z-axes). Their preferred directions are distributed evenly, with each neuron corresponding to one octant of a sphere. Only one of the neurons (grey arrow) is depicted. Each neuron's vector has x-, y- and z-components.* ***B)*** *If the z-axis is removed, and the directional preferences of the 8 neurons (grey arrows) sampled only in 2D space, they will have preferred directions in the xy-plane, with 2 neurons preferring each quadrant. This is equivalent to looking at A) along the z-axis.* ***C)*** *If another axis is removed, and neuronal preferred direction is only sampled in one dimension (e.g. a push/pull task), then 4 of these neurons will prefer pushes, and 4 will prefer*

pulls. This is equivalent to looking along the x-axis in B). In an ideal situation with no noise, any neuron with a preferred direction in 3D space that is not perfectly orthogonal to the y-axis will have a preferred direction in the y-axis.

However, it is far from certain if we will find patterns of action-specific coding identical to those found in primates while performing calcium imaging in L5B of mouse $M1_{FL}$, as primate and mouse cytoarchitectures are quite different. Firstly, primate motor cortex contains Betz cells, which are giant corticospinal pyramidal neurons exclusively present in L5B. In human motor cortex, 12% of L5B pyramidal neurons are Betz cells, and these neurons directly synapse with lower motor neurons in the anterior grey column of the spinal cord (Rivara et al., 2003). Betz cells are implicated in fine motor control, and Betz cell pathologies are associated with motor deficits (Braak et al., 2017; Sherwood et al., 2003). In contrast, mice M1 does not contain Betz cells, nor does it have any other neuron type that directly synapses with lower motor neurons. Therefore, the circuits and motor-related activity patterns mediating fine motor control in mouse $M1_{FL}$ are likely to be organised differently than their homologues in primate motor cortex. Secondly, cortical neural organisation is not perfectly conserved across different mammalian species. For example, primates (but not rodents) have a supplementary motor area (SMA) that is adjacent to and strongly connected with M1, while marsupials have no M1 (Kaas, 2004). Considering how divergent gross neuroanatomy can be across different mammalian orders, is likely that there will be important differences in the connectivity and activity patterns in mouse M1 populations when compared to other mammals.

Nonetheless, despite the existence of several neuroanatomical differences between species, mouse M1 and primate M1 are evolutionarily homologous providing powerful models of cortical motor control both in health and disease (Brooks and Dunnett, 2009; Ellenbroek and Youn, 2016; Krubitzer and Dooley, 2013; Rabl et al., 2016). The advantage of using mice as a model system to investigate cortical control of skilled movements is their genetic tractability, vast array of Cre-driver mouse lines, possibilities for opto- and chemo-genetic manipulations and overall lower costs compared to experiments involving primates (Doyle et al., 2012; Passini et al., 2004).

5.1.2 Population coding of individual movements in rodents

While the 8-directional primate reaching experiments described above have not been replicated in rodents, directional movements have been explored. One such study trained rats to push a constant-torque lever, hold it for >1 s, and then pull it for a reward. Electrophysiological recordings from these rats revealed that many M1 neurons produced different spike rates during directional movements, in both superficial and deep layers (Isomura et al., 2009). Moreover, population calcium imaging of L5A/B neurons in anterior lateral motor cortex (ALM) of mice trained to lick either to the left or to the right in a whisker tactile discrimination task displayed differential activity patterns during execution of the task, e.g. higher activity during a left lick or during a right lick (Li et al., 2015). A separate study trained mice to perform reaches with the contralateral forelimb in one of three directions, and found a subpopulation of L2/3 neurons in mouse secondary motor cortex preferentially increased their activity during reaches in one or more directions (Galiñanes et al., 2018). Thus, neurons in rodent motor cortex do display movement-specific and direction specific activity during behaviour.

Regardless of their different neuroanatomy and connectomes, motor cortical neurons in mouse and primate are both responsible for the same function, which is to drive forelimb movements. This chapter will examine how motor commands are encoded in L5B population activity in $M1_{FL}$ during the execution of a push/pull lever task, and how patterns of activity compare with other known schemes of motor coding.

5.2 Materials and methods

ΔF/F time series acquired for individual ROIs during calcium imaging, and the time points of successful lever movements (i.e. pushes and pulls), were obtained using the methods described in Chapter 4. The analysis algorithms described in this chapter were written by Premchand Brian, Dr Julian Ammer, and Dr Stephen Currie. Statistical tests were performed with the significance value (α) set at 0.05.

5.2.1 Classifying neurons based on differences in pre-movement baseline

During electrophysiological recordings in mammals, movement-related changes in neuronal activity in M1 appear ≤500 ms before the onset of movement (Evarts, 1974; Fu et al., 1995; Georgopoulos et al., 1982; Makino et al., 2017). Any neural activity that occurs more than 500 ms before the cued movement is considered to be unrelated to the behavioural task. Therefore, the pre-movement baseline period was defied as the mean ΔF/F in a window ranging from -1.5 s to -0.5 s prior to movement onset. The baseline window was not extended any further than -1.5 s to avoid including changes in activity related to the previous trial. As discussed in Chapter 4, differences in ΔF/F observed in the baseline period likely relates to the encoding of non-task-related movement, or differences in posture prior to the execution of a learned forelimb movement. Therefore, it was necessary to exclude neurons with significant pre-movement baseline differences during push and pull trials.

To classify a neuron as posture or non-posture related, a Welch's unequal variances *t*-test (two-tailed) was performed on the pre-movement baseline period before each push and pull movement, to determine if there was a statistically significant difference. Due to the slow kinetics of GCaMP6s (described in detail in Section 4.1.2), any differences in pre-movement baseline ΔF/F will influence the movement period and confound the interpretations of ΔF/F around the time of movement. In addition, it would not be possible to separate the relative contributions of task-related and non-task-related activity. Therefore, neurons with significantly different pre-movement baselines (named posture neurons for brevity) were excluded from further analysis.

5.2.2 Classifying neurons based on movement-related activity

Neurons that had statistically similar baselines were further classified based on their push- and pull-related (i.e. movement-related) activity levels. Movement-related activity was calculated from the mean ΔF/F in a 1 s period from movement onset. Since each successful movement resulted in the delivery of a water reward at 1 s after completion of the task, this period excluded reward delivery. This exclusion was intentional, as mice engaged in licking and produced gross body and forelimb movements upon presentation of the water spout, actions which were not directly related to the forelimb lever movement.

An alternative method for quantifying movement-related activity was also considered. This entailed measuring the maximal post-movement change in ΔF/F from baseline (either a positive peak or negative trough) and using it as a measure of movement-related activity. Only measuring activity in terms of maximal ΔF/F changes had the advantage of avoiding bin edge effects. However, this method was ultimately rejected as it produced higher levels of variability from the same data set, suggesting that it was more sensitive to noise. In addition, the method was unable to separate reward-related neural activity, such as activity related to licking, drinking, gross body movements, etc., from task-related neural activity, as many neurons displayed peak ΔF/F values after the water reward had been administered. More details on this method are available in Appendix A.1.

In order to account for inter-ROI variability in baseline ΔF/F prior to each cued movement, all movement-related changes in ΔF/F were baseline subtracted. Thus, movement-related activity represents the change of a neuron's activity from its baseline during the execution of the lever task. Since ΔF/F can increase or decrease from baseline levels, movement-related activity can be positive or negative. For each neuron, Welch's unequal variances *t*-test (two-tailed) was performed on push- and pull-related activity, to test if they were significantly different from zero. If both forms of movement-related activity were statistically equivalent to zero, that neuron was considered to be non-task-related and excluded from further analyses.

For task-related neurons, a dissimilarity index (DI) was calculated to quantify the differences between push- and pull-related ΔF/F changes. This dissimilarity index was created to be a quantifiable measure of the difference in push- and pull-related activity, with a dissimilarity

index far from zero representing a neuron that differentially encodes push and pull trials (Figure 5.2).

To calculate a neuron's DI, a Welch's unequal variances *t*-test (two-tailed) was first used to compare push- and pull-related ΔF/F changes observed in that neuron across all trials, producing a p-value 'p', which was then used to calculate:

$$\text{Dissimilarity index} = -\log_{10}(\text{p}) \text{ if } \Delta\text{F}/\text{F}_{\text{push}} > \Delta\text{F}/\text{F}_{\text{pull}}$$

$$\text{Dissimilarity index} = \log_{10}(\text{p}) \text{ if } \Delta\text{F}/\text{F}_{\text{pull}} > \Delta\text{F}/\text{F}_{\text{push}}$$

High DIs correspond to higher push-related activity than pull-related activity, and vice-versa. Therefore, the dissimilarity index can be seen as a one-dimensional version of 'directional preference' (see Figure 5.1), without the implication that high activity in a certain direction encodes movement in that direction. Given the α level of 0.05, the neurons were categorised as having significant DI if it was greater than 1.3 or less than -1.3, with the cut-off of 1.3 being $|\log_{10}(0.05)|$. Other neurons with a dissimilarity index between -1.3 and 1.3 (i.e. dissimilarity index ≈ 0) were considered to have statistically equivalent push- and pull-related activity.

Graphs depicting mean normalised ΔF/F were also plotted for each neuronal category. For these graphs, each neuron in that category had its mean ΔF/F change from baseline smoothed with a 2-second-wide loess filter, then normalised to a range between -1 and 1, with the largest absolute change from 0 being defined as 1.

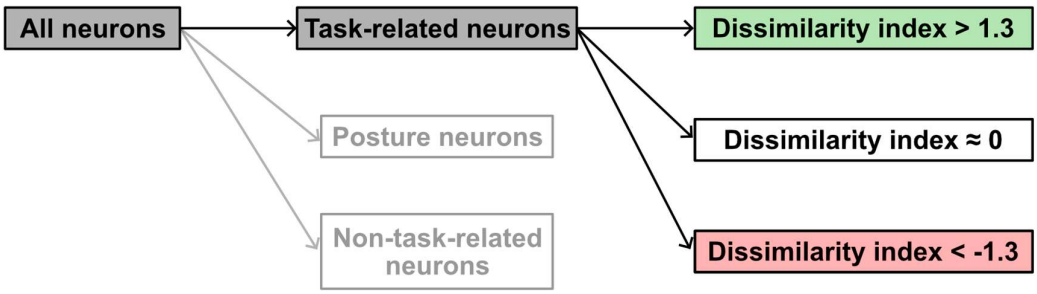

Figure 5.2: Overview of neuron classification. Neurons which had significantly unequal baselines were classified as posture neurons, while neurons with no significant movement-related activity were classified as non-task-related. These two categories of neurons were excluded from further analysis. The remaining neurons, classified as task-related neurons, were further divided based on the differences between push-related and pull-related activity, quantified in terms of their dissimilarity indices.

5.3 Results

The data analysed in this section were derived using the methods described in Chapters 3 and 4. A total of N = 15 non-overlapping calcium imaging fields of view, ranging from 500 to 636 µm below the dural surface, were recorded in L5B of $M1_{FL}$ in 7 mice, containing a total of n = 851 neurons.

5.3.1 Identification of non-task-related neurons or neurons displaying unequal pre-movement baseline fluorescence

As an initial step, neurons with significantly different pre-movement baselines (posture neurons) and neurons with no movement-related ΔF/F changes (non-task-related neurons) were identified and excluded from further analysis. Figure 5.3 below depicts the ΔF/F activity of several posture and non-task-related neurons.

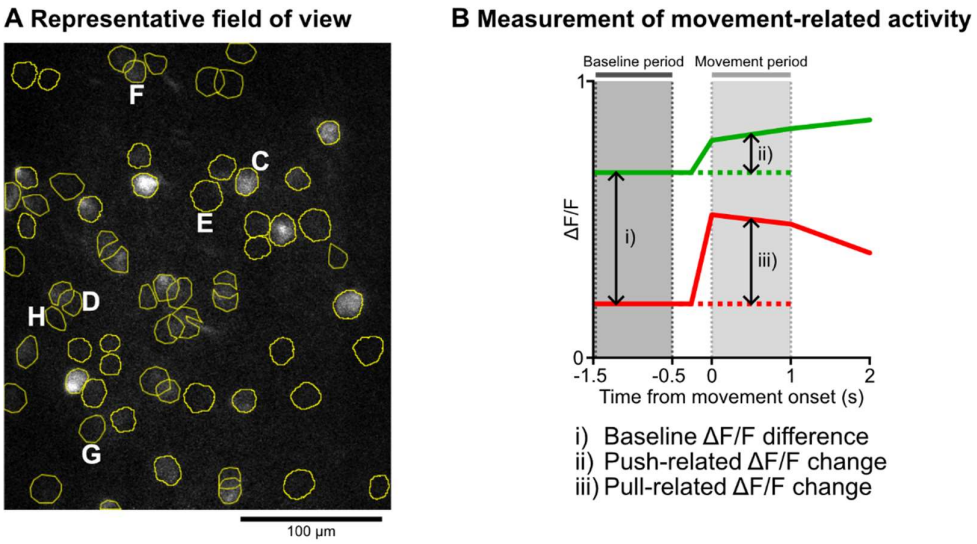

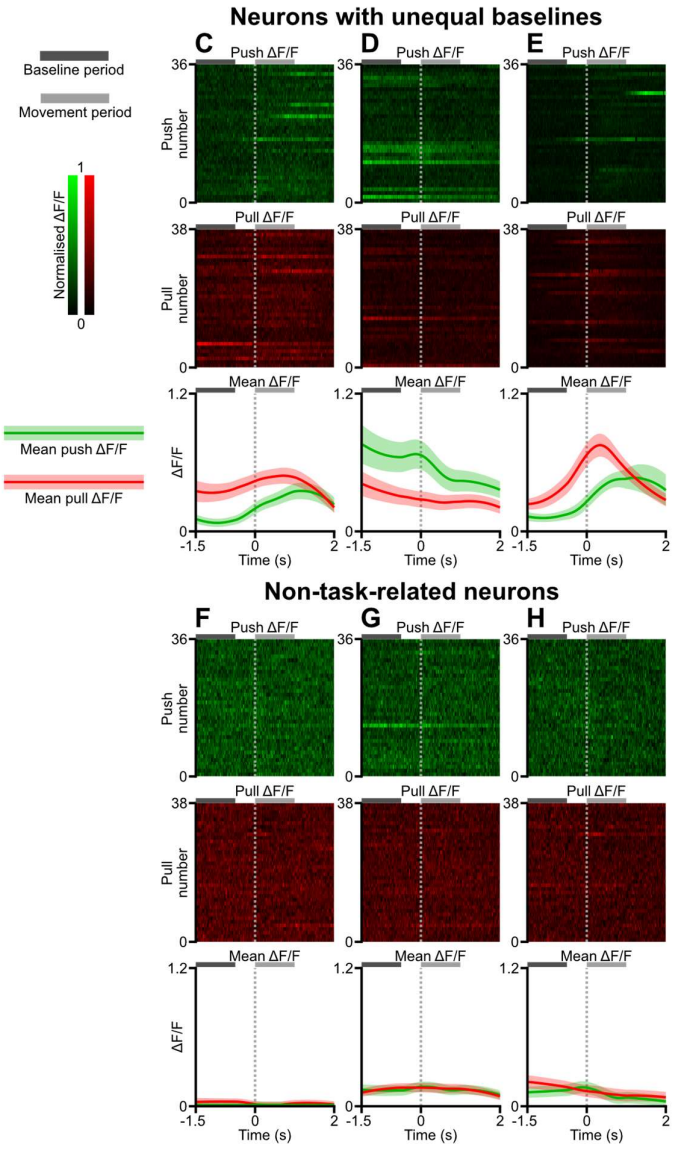

Figure 5.3: ΔF/F metrics during movement in non-task-related L5B neurons. ***A)*** *An example field of view of L5B neurons, with regions of interest (yellow circles) drawn around each identified neuron. The neurons labelled C-H have their movement-related ΔF/F values plotted on the lower half of the figure.* ***B)*** *Schematic of how movement-related ΔF/F metrics were calculated for each neuron. The green line represents ΔF/F values during a push trial, and the red line represents ΔF/F values during a pull trial. i) Difference between pre-push and pre-pull baselines. ii) Push-related ΔF/F change. iii) Pull-related ΔF/F change.* ***C-E)*** *Upper heat maps depict ΔF/F during individual push trials, while the lower heat maps depict ΔF/F during individual pull trials. Each row on the heat map represents one successful push or pull movement, and the heat maps were normalised to the maximum and minimum ΔF/F values of that neuron across all trials. The dark grey bar depicts the 1 s baseline period, and the light grey bar depicts the 1 s movement period. The lower plot depicts mean ΔF/F smoothed with a 2-second-wide loess filter, with mean push ΔF/F in green and mean pull ΔF/F in red ± s.e.m. The dotted vertical line indicates the time of movement onset.* ***F-H)*** *Three example neurons with no task-related activity.*

For each neuron in a field of view, ΔF/F values were examined during both baseline and movement periods. If the baseline ΔF/F values were significantly different, the neuron was classified as a posture neuron and excluded from further analyses. If push-related and pull-related changes in ΔF/F were not significantly different from zero, the neuron was classified as non-task-related and excluded from further analyses. By eliminating posture neurons and non-task-related neurons, I aimed to ensure that the remaining neurons were 1) producing neural activity patterns related to the execution of the task, and 2) not potentially contaminated by baseline differences resulting from non-task-related movements.

From n = 851 neurons recorded in L5B, a total of 141 neurons were classified as posture neurons and of the remaining 710 neurons, 148 were found to be non-task-related. The remaining 562 neurons (66.0% of the original 851 neurons) had statistically equivalent pre-push and pre-pull baselines and displayed task-related ΔF/F changes so were classified as task-related neurons.

Even after removing the posture neurons, task-related neurons which had statistically equivalent baselines often had variable baseline ΔF/F values between trials, likely due to the fact that cortical neurons exhibit a high degree of trial-to-trial firing rate variability *in vivo* (Holt et al., 1996; Salinas, 2006). While some of this variance is inevitably a result of the stochastic biochemical processes underlying neuronal activity, it may also serve as a functional component of neuronal computations, or carry information on other behaviourally relevant parameters such as motivation or sensory input (Faisal et al., 2008; Hussar and Pasternak, 2010; Scaglione et al., 2011). Regardless of its origin and physiological function, the high degree of variability in baselines potentially obscured movement-related ΔF/F changes during task execution. Therefore, baseline ΔF/F values observed in task-related neurons were subtracted on a trial-by-trial basis.

5.3.2 Neural activity patterns in task-related neurons

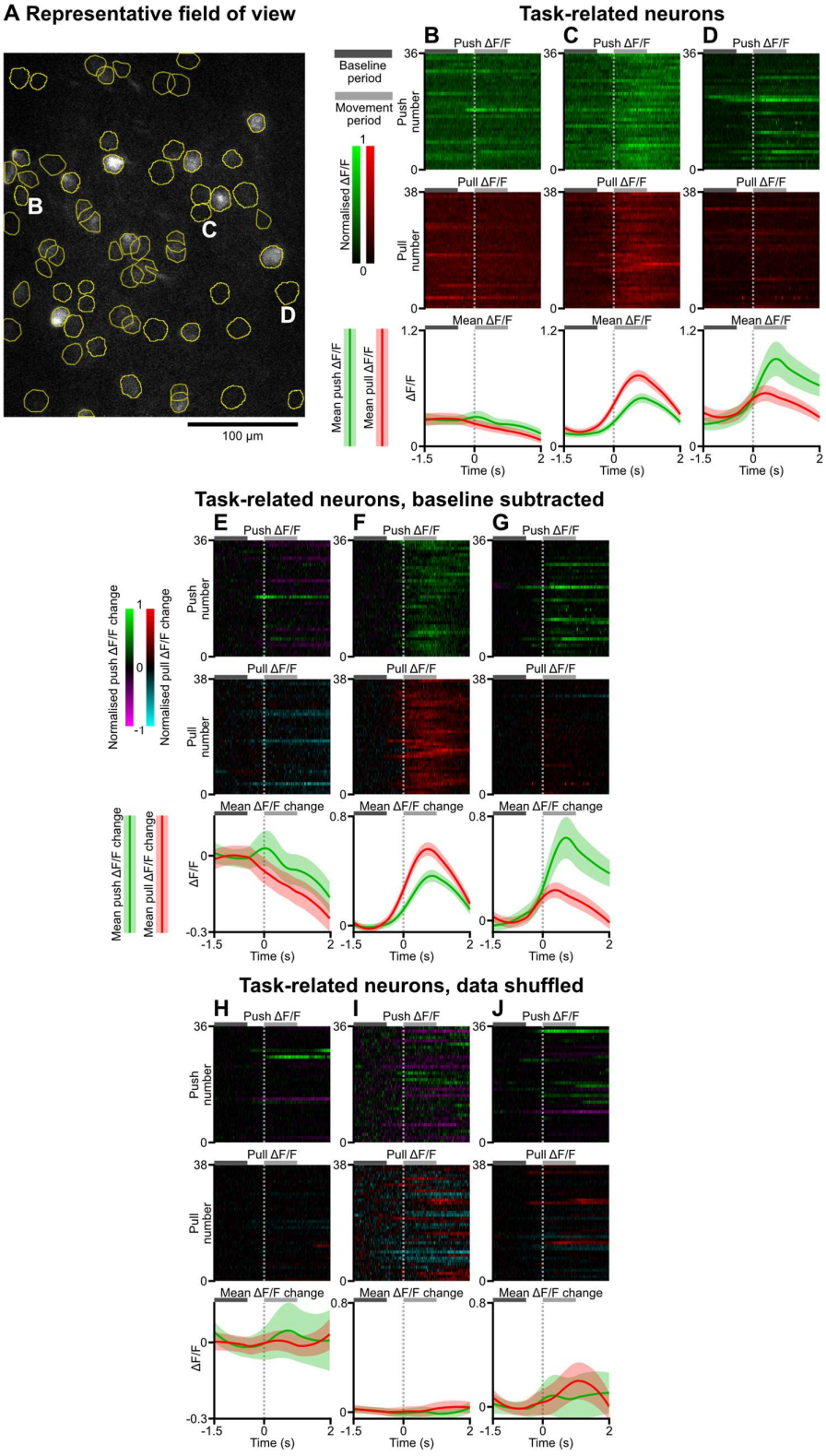

Figure 5.4: Movement-related ΔF/F changes in task-related L5B neurons. ***A)*** *An example field of view of L5B neurons, with regions of interest (yellow circles) drawn around each identified neuron. For continuity, this is the same field of view as shown in Figure 5.3, but with three example task-related neurons labelled B-D.* ***B-D)*** *Movement-related activity of 3 task-related neurons. The upper heat maps depict ΔF/F during individual push trials, while the middle row of heat maps depict ΔF/F during individual pull trials. Each row on a heat map represents one successful push or pull trial, and heat maps are normalised to the maximum and minimum ΔF/F values of that neuron across all trials. The dark grey bar depicts the 1 s baseline period, while the light grey bar depicts the 1 s movement-related period. The lower plots depict mean ΔF/F smoothed with a 2-second-wide loess filter, with mean push ΔF/F in green and mean pull ΔF/F in red ± s.e.m. The dotted vertical line indicates the time of movement onset.* ***E-G)*** *The same neurons shown in B-D, but plotted with the pre-action baseline subtracted from each row to emphasise how ΔF/F changes from baseline. The heat maps were normalised to the largest change in ΔF/F from baseline across all time points and all actions, in terms of absolute magnitude.* ***H-J)*** *The same neurons shown in B-C, but with peri-push and peri-pull ΔF/F time series randomly aligned to time points from the entire ΔF/F time series, thus providing a randomly sampled distribution of non-task-related neural activity. The axes of the mean ΔF/F plots in H-J are the same as those used in E-G, respectively.*

Figure 5.4 above presents a representative field of view of L5B neurons, and ΔF/F time series of several neurons recorded during execution of the lever task. The neuron shown in E) is a typical example of a neuron with similar pre-movement baselines that displayed a significant decrease in ΔF/F during both movement trial types. Conversely, the example neurons shown in F & G also displayed no significant difference in pre-movement baselines, but displayed a significant increase in ΔF/F during both trial types. All 3 example neurons shown above were classified as task-related.

To account for the variability in pre-movement baseline ΔF/F across trials, baseline subtraction – a ubiquitous method throughout the field of neuroscience – was employed to aid in visualising ΔF/F changes during movement. This involved subtracting the mean baseline ΔF/F from the ΔF/F time series of each individual action, resulting in the heat maps and ΔF/F time series depicting changes in ΔF/F from baseline. Given the improvement in visualisation and interpretation all subsequent ΔF/F time series will be shown with baselines subtracted. In **E-G)**, increases in ΔF/F were colour-coded as green for push and red for pull trials, while decreases in ΔF/F were colour-coded as their complementary colours on the RGB model, i.e. magenta for pushes and cyan for pulls. This colour scheme will be used in all subsequent figures that depict task-related ΔF/F changes.

One potential concern of baseline subtraction is that by defining the baseline as zero, any change in ΔF/F on a continuously changing time series could be falsely classified as a

movement-related change, especially if there was a consistent upwards/downwards trend over time. To address this concern, **H-J)** depict negative control examples where ΔF/F time series for each 'push' and 'pull' were aligned to random points on the entire ΔF/F time series. The shuffled ΔF/F time series demonstrate that the changes in ΔF/F observed in E-G) reflect movement onset and execution.

5.3.3 Heterogeneous activity patterns of task-related L5B neurons

Having excluded posture neurons and non-task-related neurons, the remaining n = 562 neurons were classified as task-related. These neurons displayed heterogeneous activity patterns during task execution. To organise this diverse data set of motor activity into a comprehensible taxonomy, task-related neurons were classified into several categories based on their dissimilarity indices. The first category consisted of neurons that displayed task-related activity, either in terms of significantly increased or decreased ΔF/F during push or pull trials, but with no significant difference between trial types, i.e. dissimilarity index ≈ 0. Out of the 562 task-related neurons, 381 (67.8%) had dissimilarity indices ≈ 0.

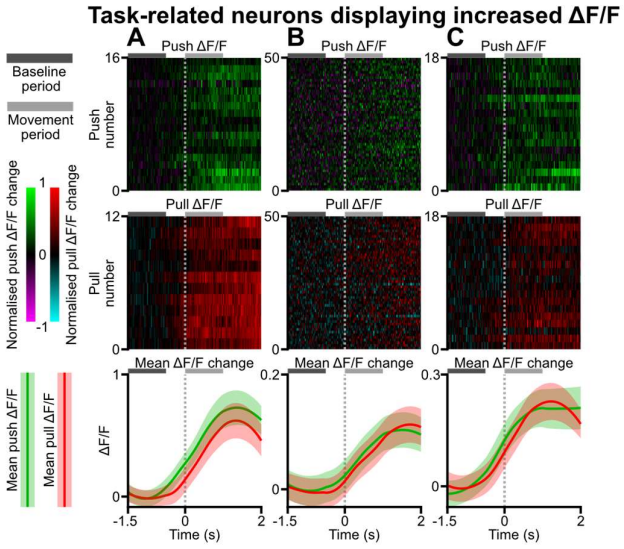

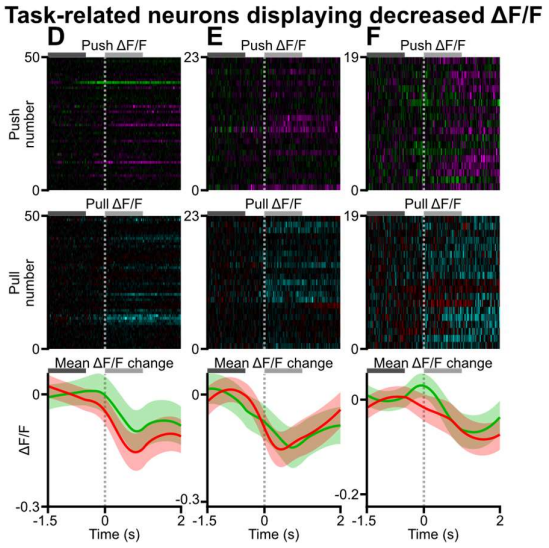

Figure 5.5: Examples of movement-related ΔF/F changes in L5B neurons with a dissimilarity index ≈ 0. ***A-C)*** *Movement-related ΔF/F changes in 3 representative neurons that show a significant increase in ΔF/F during both push and pull trials, with a dissimilarity index ≈ 0. The upper heat map depicts ΔF/F during individual push trials, while the middle heat map depicts ΔF/F during individual pull trials. Each row represents one successful push or pull trial, and the heat maps were normalised to the maximum and minimum ΔF/F values of that neuron across all trials. The dark grey bar depicts the 1 s baseline period, while the light grey bar depicts the 1 s movement-related period. The lower plot depicts mean ΔF/F smoothed with a 2-second-wide loess filter, with mean push ΔF/F in green and mean pull ΔF/F in red ± s.e.m. The dotted vertical line indicates the time of movement onset.* ***D-F)*** *Movement-related ΔF/F changes in 3 representative neurons that show a significant decrease in ΔF/F during both push and pull trials, with a dissimilarity index ≈ 0.*

The example neurons shown in Figure 5.5 all display movement-related changes in ΔF/F, however the response magnitude between different trial types (i.e. push or pull) were not statistically different, suggesting they do not specifically encode push or pull movements. In contrast, we did observe other categories of task-related neurons that displayed significant changes in ΔF/F changes during push and pull movements, but with DI < -1.3 or > 1.3. These neurons made up 181 (32.2%) of the 562 task-related neurons.

Considering that corticospinal activity drives the execution of skilled forelimb movements in mice (Guo et al., 2015; Morandell and Huber, 2017; Wang et al., 2017), and that L5B of the cortex is the sole source of corticospinal projections (Anderson et al., 2010; Hooks et al., 2013; Oswald et al., 2013; Schiemann et al., 2015), it is reasonable to suggest that motor commands driving different forelimb movements are likely to be encoded in L5B neuron activity. In order to encode motor commands for different movements, they must exhibit

distinct activity patterns during different movements, i.e. neurons that display dissimilarity indices that are significantly different from zero (Figure 5.6).

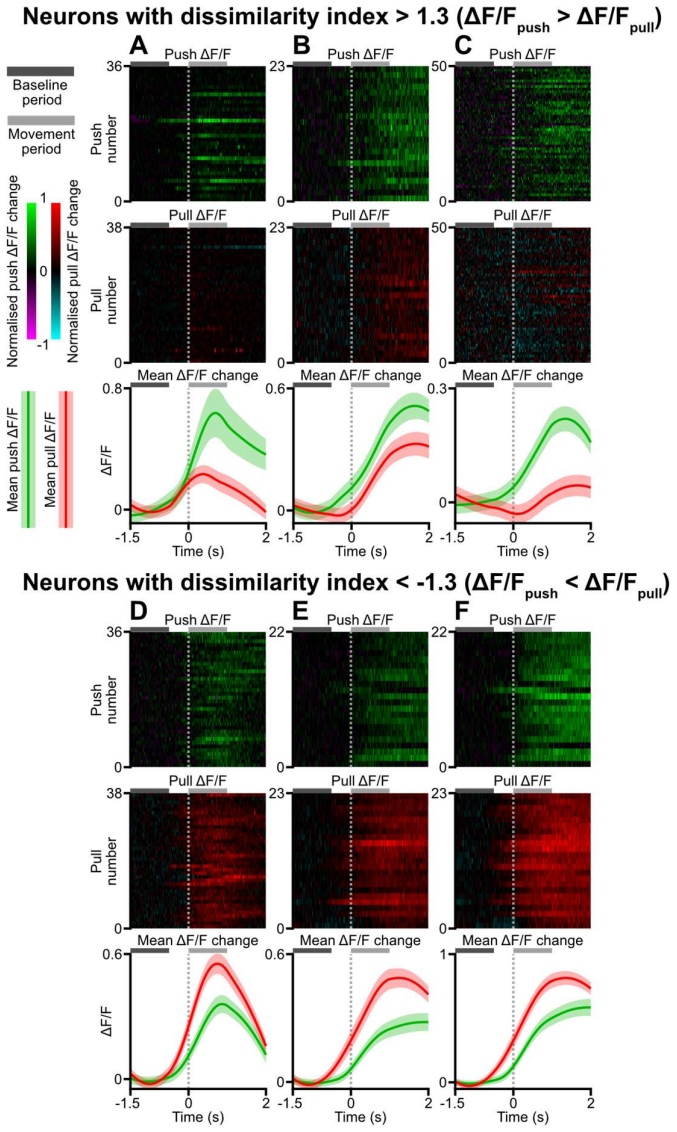

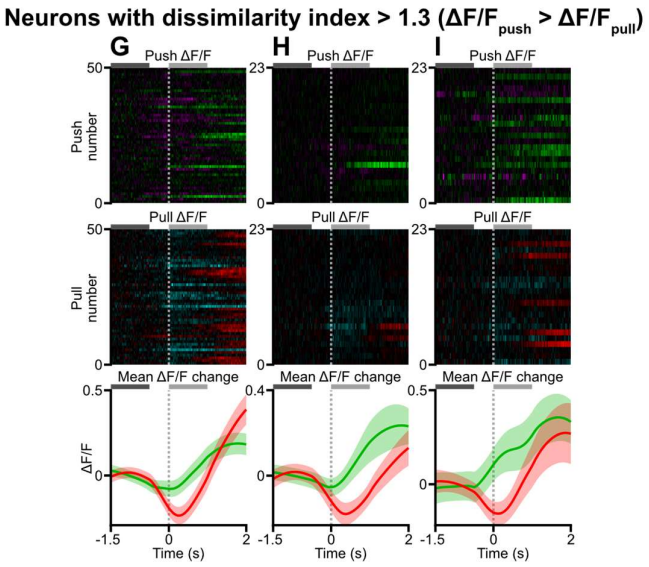

Figure 5.6: Examples of task-related L5B neurons with dissimilarity indices > 1.3 or < -1.3. ***A-C)*** *Movement-related ΔF/F changes in 3 representative neurons that show a significant increase in ΔF/F during both push and pull trials, and a dissimilarity index > 1.3 due to* $\Delta F/F_{push} > \Delta F/F_{pull}$*. The upper heat map depicts ΔF/F during individual push trials, while the middle heat map depicts ΔF/F during individual pull trials. Each row represents one successful push or pull trial, and the heat maps were normalised to the maximum and minimum ΔF/F values of that neuron across all trials. The dark grey bar depicts the 1 s baseline period, while the light grey bar depicts the 1 s movement-related period. The lower plot depicts mean ΔF/F smoothed with a 2-second-wide loess filter, with mean push ΔF/F in green and mean pull ΔF/F in red ± s.e.m. The dotted vertical line indicates the time of movement onset.* ***D-F)*** *Movement-related ΔF/F changes in 3 representative neurons that show a significant increase in ΔF/F during both push and pull movements, and a dissimilarity index < -1.3 due to* $\Delta F/F_{push} < \Delta F/F_{pull}$*.* ***G-I)*** *Movement-related ΔF/F changes in 3 representative neurons that show ΔF/F increases during pushes and ΔF/F decreases during pulls, and a dissimilarity index > 1.3 due to* $\Delta F/F_{push} > \Delta F/F_{pull}$*.*

Within the category of neurons that exhibited dissimilarity indices > 1.3 or < -1.3, a diverse range of activity patterns was observed. Neurons **A-C)** are examples of neurons that exhibited an increase in ΔF/F during both movement types, with the push-related increase being larger than the pull-related increase, resulting in a dissimilarity index greater than 1.3. Neurons **D-F)** also exhibited increased ΔF/F during push and pull trials, but the pull-related changes were on average larger. Whereas in **G-I)**, neurons exhibited divergent patterns of activity, with ΔF/F increasing during push and decreasing during pull trials, but resulting in a dissimilarity index of greater than 1.3.

One interesting observation was the lack of neurons with a dissimilar index of <-1.3 where push-related activity resulted in the largest change in ΔF/F when compared to pull trials. Nearly all neurons with dissimilarity index < -1.3 (64 out of 66 neurons) displayed a ΔF/F increase during both pushes and pulls.

5.3.4 Task-related activity in the L5B neuronal population

In order to take a wider view of the neural activity in task-related neurons across all field of view, heat maps were generated to display mean ΔF/F changes during push and pull trials (Figure 5.7).

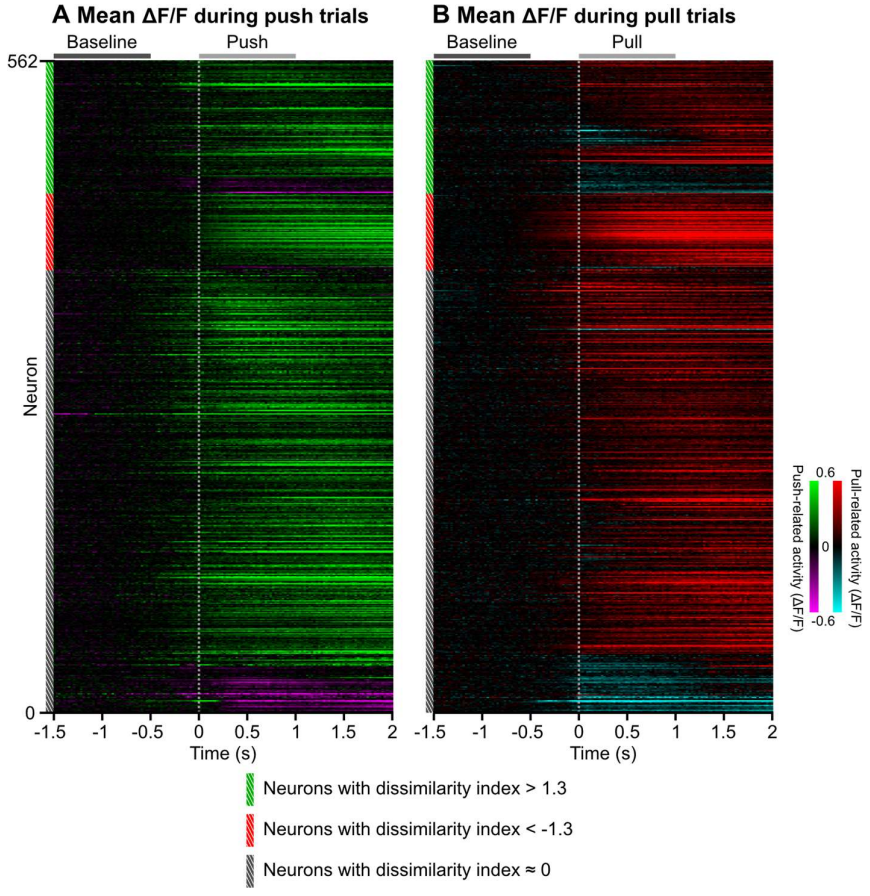

Figure 5.7: Heat maps of ΔF/F changes in task-related L5B neurons. ***A)*** *Heat map of mean push-related changes in ΔF/F. Each row represents a neuron, with the colours indicating the mean change in ΔF/F from its baseline. The hatched bars on the left represent neuron*

classification. From top to bottom on the left, neurons were sorted by 1) neuron classification, 2) increasing or decreasing ΔF/F during the movement period and 3) by peak ΔF/F. ΔF/F values were not smoothed or normalised. The dark grey bar depicts the 1 s baseline period, while the light grey bar depicts the 1 s movement-related period. The dotted vertical line indicates the time of movement onset. ***B)*** *Heat map of mean pull-related changes in ΔF/F organised as in A), except that the neurons/rows were not sorted and correspond to the same neurons shown in A).*

The heat maps above indicate that the majority of neurons in $M1_{FL}$ L5B exhibited ΔF/F increases during push (506/90.0% increase, 56/10.0% decrease) and pull trials (450/80.1% increase, 112/19.9% decrease). Moreover, most neurons have a dissimilarity index ≈ 0 (381/67.8%), while among the remaining neurons, more had a dissimilarity index > 1.3 (115/20.5%) than < -1.3 (66/11.7%). This finding was surprising, as I did not have any *a priori* reasons to believe that push and pull trials would be encoded asymmetrically in $M1_{FL}$. Indeed, the initial models of directional coding in primates theorised that the directional preference vectors of primate M1 neurons are uniformly distributed (Caminiti et al., 1990; Georgopoulos et al., 1988). The implications of this asymmetry in terms of movement coding in $M1_{FL}$ will be explored in the discussion.

By way of comparison, the same data on task-related neuronal activity was grouped by field of view and re-plotted, to better describe how action-related activity compared across fields of view (Figure 5.8).

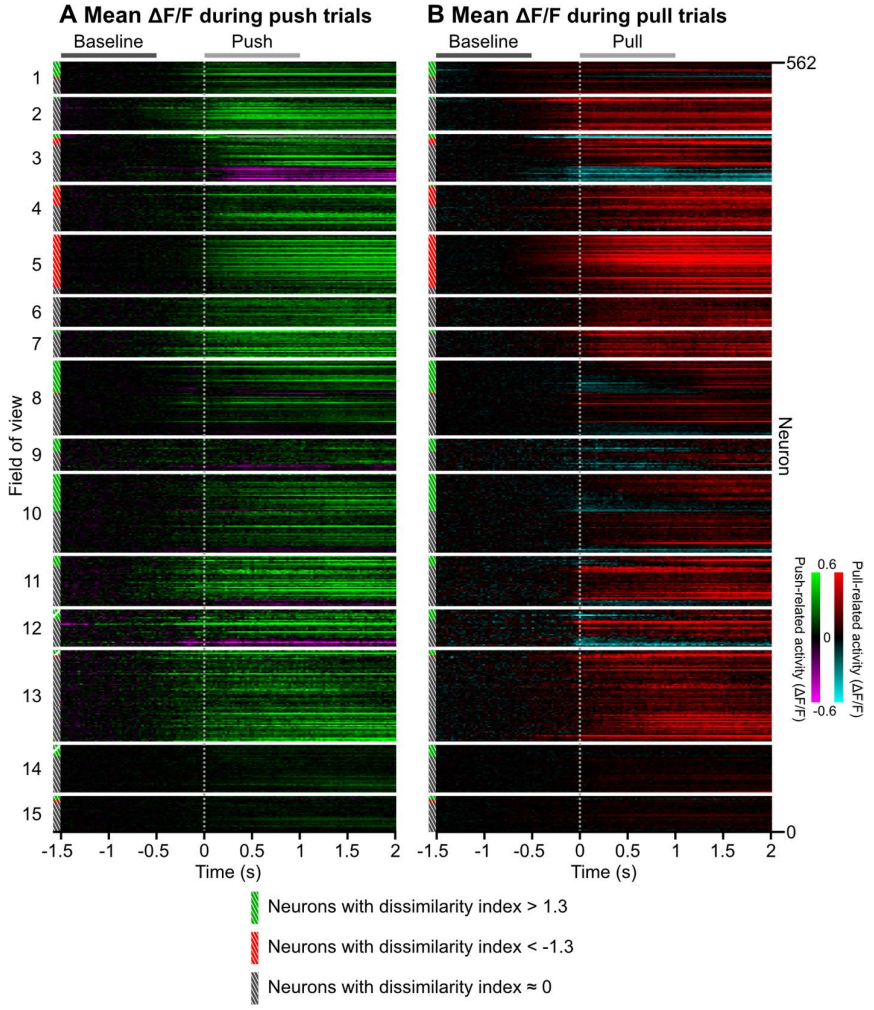

Figure 5.8: Heat maps of ΔF/F changes in task-related L5B neurons, grouped by field of view. ***A)*** *Heat map of mean push-related changes in ΔF/F. Each row represents a neuron, with the colours indicating the mean change in ΔF/F from its baseline. The hatched bars on the left represent neuron classification. From top to bottom on the left, neurons were sorted by 1) field of view 2) neuron classification, 3) increasing or decreasing ΔF/F during the movement period and 4) by peak ΔF/F. ΔF/F values were not smoothed or normalised. The dark grey bar depicts the 1 s baseline period, while the light grey bar depicts the 1 s movement-related period. The dotted vertical line indicates the time of movement onset.* ***B)*** *Heat map of mean pull-related changes in ΔF/F organised as in A), except that the neurons/rows were not sorted and correspond to the same neurons shown in A).*

The dissimilarity index-based neuronal categories were not evenly distributed across different fields of view. The majority contained more neurons with a dissimilarity index > 1.3, while only two fields of view were dominated by neurons with a dissimilarity index < -1.3. Initially, there were concerns that dissimilarities between push and pull activity were driven by differences in pre-action motion index. For example, if the mouse recorded in field of view

10 made more non-task-related forelimb movements in the window between -0.5 to 0 s before pushes than before pulls, and neuronal ΔF/F was influenced by any forelimb movement, the high dissimilarity indices in those neurons might be related to differences in pre-action motion index rather than the lever movements themselves. Indeed, the linear mixed-effects analysis described in Chapter 4 indicated that pre-action forelimb movement as measured by motion index was correlated with neuronal ΔF/F.

However, the model outcomes also showed that motion index provided a far smaller influence on neuronal ΔF/F than movement direction (i.e. push or pull), so this is unlikely to significantly influence neuron classification. Moreover, pre-action motion index was not directly related to neuronal classification based on dissimilarity indices, with no clear trend between pre-movement motion index and dissimilarity index in each field of view. More details are available in Appendix A.1.

To provide an overview of the task-related changes in ΔF/F across the L5B population, each ROI within a field of view was plotted and colour coded according to their 1) average movement-related ΔF/F during push and pull trials (Figure 5.9) or 2) dissimilarity index (Figure 5.10).

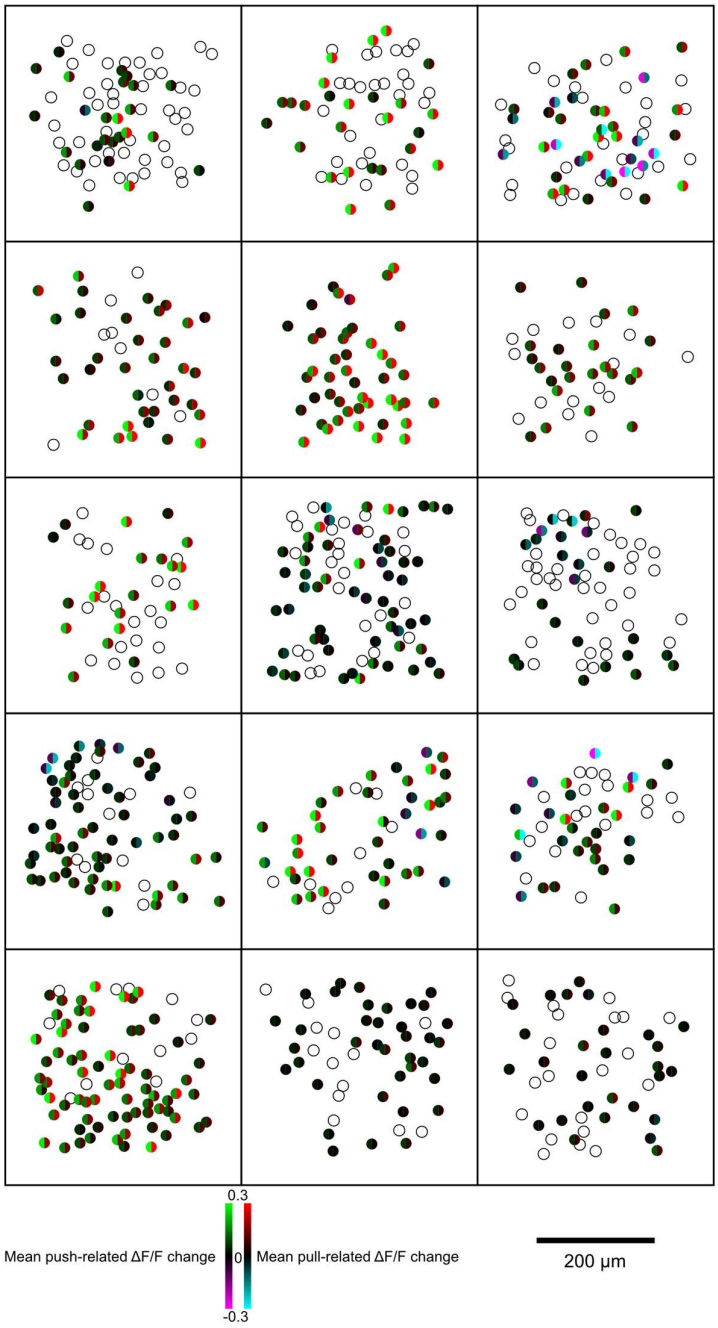

Figure 5.9: Overview of ΔF/F changes in task-related L5B neurons grouped by field of view. Each square represents a field of view and each circle represents an individual neuron. The spatial position of each circle plotted here corresponds to the position of the neuron's centre in the actual field of view. Neurons excluded due to unequal baselines (i.e. posture neurons) or due to being non-task-related are depicted as empty circles. Task-related neurons are plotted as coloured circles with the left half indicating its mean push-related ΔF/F change and right half indicating mean pull-related ΔF/F change. From left to right and top to bottom, each field of view is in the same order as the heat map shown in Figure 5.8 above.

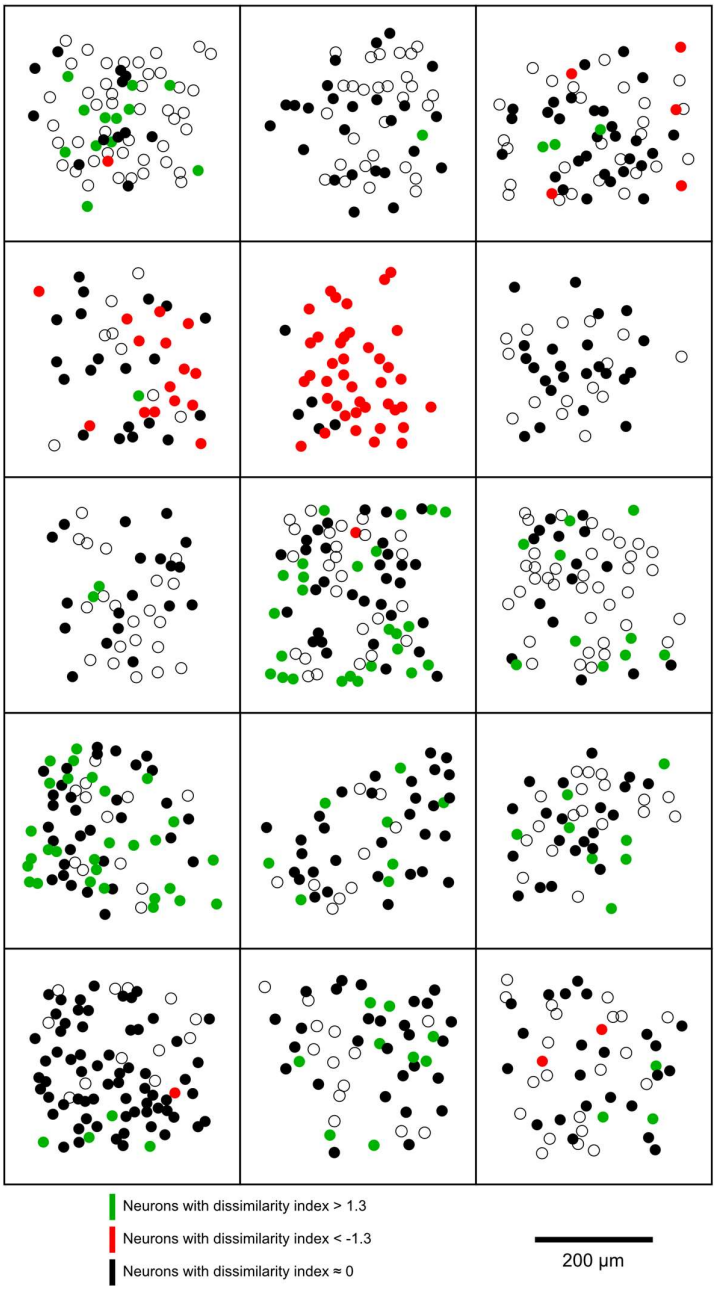

Figure 5.10: Overview of dissimilarity indices in task-related L5B neurons grouped by field of view. Each square represents a field of view and each circle represents an individual neuron. The spatial position of each circle plotted here corresponds to the position of the neuron's centre in the actual field of view. Neurons excluded due to unequal baselines (i.e. posture neurons) or due to being non-task-related are depicted as empty circles. Task-related neurons are plotted as coloured circles with the left half indicating its mean push-related ΔF/F change and right half indicating mean pull-related ΔF/F change. From left to right and top to bottom, each field of view is in the same order as the heat map shown in Figure 5.8 above.

While there was no immediately apparent consistent pattern of ΔF/F changes or dissimilarity indices across all L5B fields of view, this absence in itself is an important observation. Neurons in primates M1 are thought to be spatially organised into repeating columns of directional preference approximately 120 µm wide, with each column perpendicular to the cortical surface and containing ~30-µm-wide mini-columns of direction-preferring neurons, with preferred directions covering all octants of 3D space (Amirikian and Georgopoulos, 2003; Georgopoulos et al., 2007). In contrast, we observed some fields of view (e.g. field of view 3) where neurons that were adjacent to each other had differential patterns of activity. In contrast, in field of view 5 nearly all neurons displayed the same activity patterns during behaviour.

This lack of cortical columnar organisation in "lower mammals" is not unprecedented. For example, neurons in the primary visual cortices (V1) of cats, monkeys and humans are arranged in "pinwheel" orientation columns (Dow, 2002; Hubel and Wiesel, 1963; Yacoub et al., 2008), while in mouse V1 directionally-preferring cells are scattered in a random "salt-and-pepper" arrangement (Dräger, 1975; Hansel and van Vreeswijk, 2012; Ohki and Reid, 2007). A study involving pellet grasping and retrieval in mice also identified neurons that were preferentially active during different phases of the task. Some were more active during the initial forelimb reaching phase, while others were more active during post-grasping forelimb retraction, and these were unevenly scattered throughout M1 (Wang et al., 2017). Specifically, more rostromedial neurons tended to be preferentially activated during forelimb reaches, while more caudolateral neurons tended to be preferentially activated during forelimb retractions, though both of these neuronal types were intermingled. Another study involving optogenetic stimulation of rostral M1 produced forelimb abductions, while stimulating caudal M1 produced forelimb adductions (Harrison et al., 2012). Forward-oriented reaches and forelimb abductions are mechanically similar to the lever pushes used in this study, while post-grasp pellet retrieval and forelimb adductions are mechanically similar to our lever pulls. Therefore, instead of being organised in repeating cortical columns ~120µm wide, neurons which preferentially activate during a specific directional movement may be clustered in non-repeating macro-scale somatotopic regions.

Compared to both of these studies mentioned above, the coordinates at which we imaged $M1_{FL}$ correspond to the region between the "push-related zone" and "pull-related zone". If $M1_{FL}$ is somatotopically mapped to push and pull actions, with some degree of variation

between individual mice, it is possible that most of the fields of view (FOVs) we recorded were in "push-related zone" (e.g. the FOVs numbered 1/8-12/14), two in the "pull-related zone" (FOVs 4-5), and the remainder in-between these two regions, resulting in dissimilarity indices of cells being scattered in a "salt-and-pepper" arrangement (Ohki and Reid, 2007).

5.3.5 Overview of task-related neural activity

To provide an overview of neuronal task-related activity and dissimilarity indices across all fields of view, and therefore an insight into how $M1_{FL}$ neuronal encoding of movement in L5B, I plotted the mean push-related ΔF/F change as a function of pull-related ΔF/F for each task-related neuron (Figure 5.11).

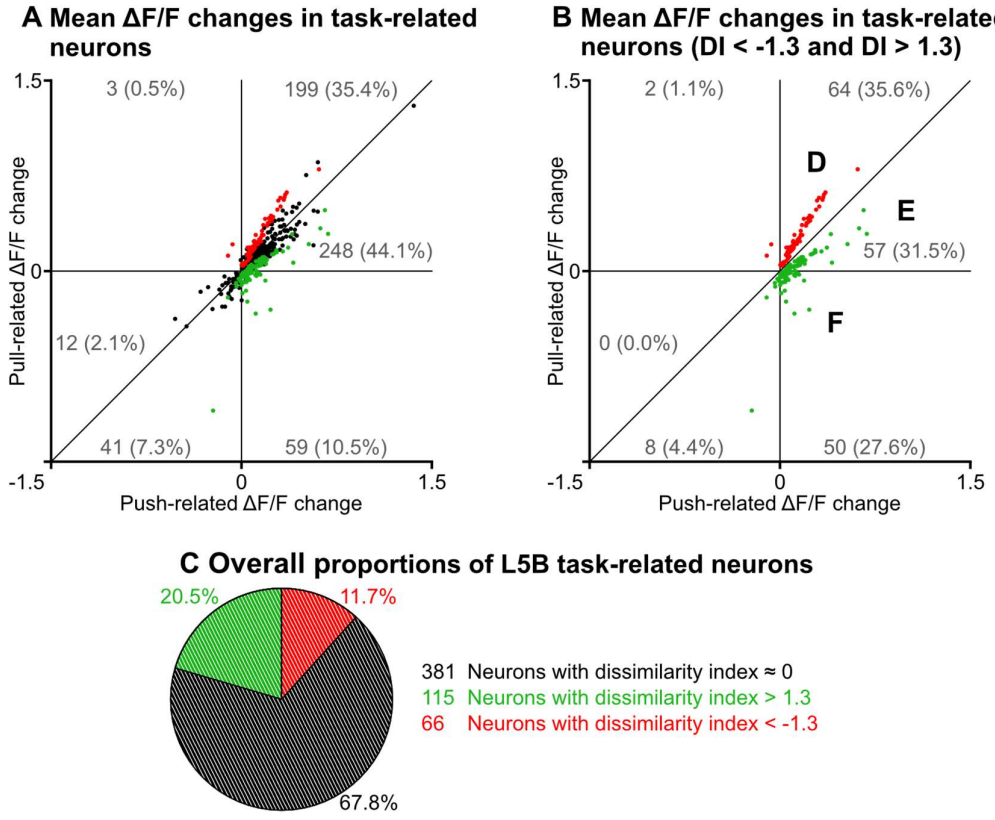

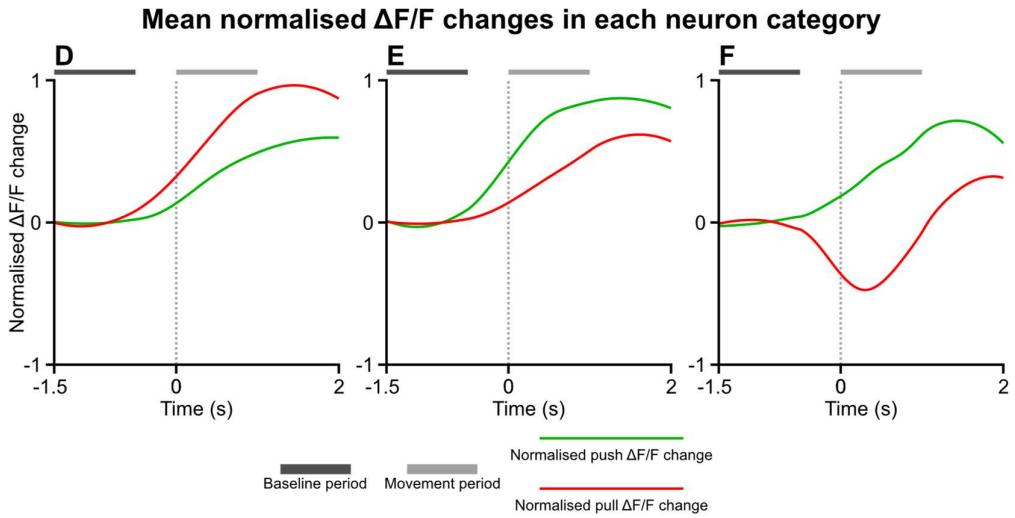

Figure 5.11: Overview of mean task-related ΔF/F changes in L5B neurons across all fields of view. ***A)*** *A total of 562 task-related neurons, with mean change in push-related ΔF/F plotted against mean change in pull-related ΔF/F. Green and red circles represent neurons with significant push/pull dissimilarity, and black circles represent neurons with a dissimilarity index ≈ 0. The grey numbers in each sector indicate the number of neurons in that sector of the graph and the percentage of the overall population in brackets.* ***B)*** *Same graph as A), with neurons with a dissimilarity index ≈ 0 removed.* ***C)*** *Pie chart summarising the number of neurons in each category and the percentage of the whole population.* ***D-F)*** *Graphs depicting mean normalised ΔF/F changes in the three neuronal subpopulations labelled in B). The dark grey bar depicts the 1 s baseline period, and a light grey bar depicts the 1 s movement-related period. The dotted vertical line indicates the time of movement onset.*

Most task-related neurons had similar push-related and pull-related ΔF/F changes (67.8%) so they lie close to the identity line in Figure 5.11 and have a dissimilarity index close to zero. The remainder either had dissimilarity indices > 1.3 (20.5%) or DI < -1.3 (11.7%) and are likely to encode action-specific motor activity, which ultimately commands downstream circuits to perform either push or pull actions.

The majority of neurons with DI < -1.3 or > 1.3 were present in the regions labelled **D-F)**, with all other regions containing insubstantial neuron counts. Intriguingly, while 27.6% of neurons with DI < -1.3 or > 1.3 decreased their ΔF/F during pull trials, almost no neurons with DI < -1.3 or DI > 1.3 (1.1%) decreased their ΔF/F during push trials. In addition, there were nearly twice as many neurons displaying dissimilarity indices > 1.3 (i.e. “push-preferring”) than dissimilarity indices < -1.3 (i.e. “pull-preferring). This is consistent with a model where different motor actions such as pushes and pulls are somatotopically mapped onto regions

in $M1_{FL}$, and the fields of view we imaged were predominantly in the region linked to pushes (Harrison et al., 2012; Wang et al., 2017).

5.4 Discussion

This chapter documents population neuronal activity in the primary output layer of mouse $M1_{FL}$ during the execution of a directional forelimb lever task. What do the results reveal about population neuronal coding in L5B of mouse $M1_{FL}$?

5.4.1 Action-specific coding in L5B neuronal populations

A significant proportion of neurons in L5B of $M1_{FL}$ (181/851, 21.3%) differentially encode push and pull trials, measured as significant differences in the amplitude and direction of movement-evoked ΔF/F. In this chapter, we defined neurons as displaying "high dissimilarity index" instead of "direction preference", despite the latter term being frequently used in the literature (Eisenberg et al., 2010; Galiñanes et al., 2018; Georgopoulos et al., 1982; Isomura et al., 2009; Li et al., 2015). While the latter is entirely appropriate when describing neural activity in a task with more than two directions, the push/pull task used in this study is strictly binary in nature, with every successful trial being either a push or a pull. Therefore, any information regarding the probability of one action occurring, gives equal information on the probability of the other action occurring. For example, a neuron which displays an increase in ΔF/F of 1 from baseline during push trials, and a decrease in ΔF/F of -0.2 during pull trials would conventionally be described as "push-preferring" (because the net change in ΔF/F is larger in the push direction when compared to pull), but in reality any change in ΔF/F (and therefore neural activity) during a given trial encodes information on whether it is one movement or the other. This distinction will be discussed in more detail in Chapter 7 where we discuss how changes in ΔF/F can be used to train a model to decode action type.

One important point that needs to be addressed is why we observed far more neurons with a dissimilarity index > 1.3 (20.5%) than neurons with a dissimilarity index < -1.3 (11.7%). Especially as early pioneering studies describing directional coding in primates theorised that the directional preferences of M1 neuronal populations are evenly distributed in space (Caminiti et al., 1990; Georgopoulos et al., 1988). However, recent studies have revealed that the preferred directions of M1 neurons in non-human primates are clustered around forelimb movements in specific directions, particular reaches away from the body (Lillicrap

and Scott, 2013; Mitsuda and Onorati, 2002; Naselaris et al., 2006). The forelimb movements during such reaches are mechanically similar to those generated during our lever pushes. However, there is no clear consensus on the cause of this non-uniformity, with possible reasons including differences in motor experience and differences in muscle activation. Differences in motor experience may arise due to test animals performing more forward reaches (e.g. to grasp food) over their lifetime than reaches in other directions (Naselaris et al., 2006). For the latter, it is possible that mainstream models of direction coding are incomplete, and that M1 neurons map better to specific muscles rather than forelimb movement directions, with the muscles activated during forwards reaches being mapped to a larger proportion of neurons in the cortex (Lillicrap and Scott, 2013). Although these data have been generated in non-human primates, the same reasoning may apply to mice.

Alternatively, the possibility exists that there is some degree of overlapping action-specific somatotopy in mouse M1 similar to that observed in human M1 (Hluštík et al., 2001; Penfield and Boldrey, 1937). If this is correct, specific regions of mouse $M1_{FL}$ will preferentially encode certain movements. For example, a cortical map of mouse M1 by (Wang et al., 2017) suggests that a higher percentage of neurons in rostral M1 display increased activity preferentially during forelimb reaches (similar to our push trials), and more neurons in caudal M1 preferentially activate during forelimb retractions (similar to our pull trials), with a continuous gradient in between. Although our imaging fields of view were always centred on the same anatomical coordinates, at 1.6 mm lateral and 0.6 mm rostral from bregma, it is possible that the somatotopy is variable between individuals, similar to human M1 somatotopy. Our results could be accounted for by the existence of a region that preferentially activated during pushes, a region that preferentially activated during pulls, and a shifting border between these two regions. To determine if this is indeed the case, wide-field calcium imaging can be performed over a larger area of $M1_{FL}$, including the rostral limb-abduction region and the caudal limb-adduction regions as previously described (Harrison et al., 2012; Wang et al., 2017), to ascertain whether lever pushes and pulls coincided with the preferential activation of different regions in $M1_{FL}$.

5.4.2 Sparse and dense coding in L5B

Neuronal coding in the mammalian cortex is often described in terms of its sparseness, whether in rat somatosensory cortex or human inferotemporal cortex (Brecht and Sakmann, 2002; Young and Yamane, 1992). However, there are two distinct forms of sparse coding which are nonetheless often used interchangeably in the field: temporal/lifetime sparseness, referring to coding schemes where single neurons display low levels of activity across most conditions, and population sparseness, referring to coding schemes where neuronal populations contain few active neurons at a given point in time (Graham and Field, 2007; Spanne and Jörntell, 2015; Willmore and Tolhurst, 2001). This ambiguity has led M1 neuronal activity to be described in the context of Georgopoulos' population vector model as both dense and sparse by different authors (Holscher and Munk, 2008; Tam, 2003). This polysemy is further compounded by the fact that there is no universally accepted threshold of what constitutes "active" or "most" in either definition of sparseness. For the purposes of this thesis, I will be exclusively referring to population sparseness, as this study focuses on population activity during movement-related time periods, not single-neuron activity over prolonged time periods. In addition, I will define "most" as "over 50%" for the sake of simplicity.

In terms of coding movements, L5B neurons in $M1_{FL}$ exhibit a dense code. The majority (66.0%) of recorded neurons exhibited significant levels of task-related activity during execution of the lever task, which is far more than what a sparse coding model would predict. In addition, the histological techniques described in Chapter 4 indicate that I sampled 85.3% of the neurons in each imaging plane, and this high proportion of active neurons cannot be explained by a large hidden population of silent, undetectable neurons that generate a sampling bias.

However, a small subpopulation of L5B neurons exhibited direction-specific activity patterns, where 21.3% of neurons displayed dissimilarity indices greater than 1.3 or less than -1.3. This would suggest that coding of task-related activity in L5B populations is dense, while coding of action-specificity in L5B neurons is sparse. In contrast, L2/3 population imaging in secondary motor cortex (M2) during a tri-directional forelimb reaching task revealed that only 12% of recorded neurons displayed task-related activity, and of the 12%, the vast majority were only responsive during reaches in 1 direction (Galiñanes et al., 2018). This

coding scheme appears to be sparse with respect to both task-relatedness and direction-specificity.

L2/3 of M2 projects to L5B of M2, which in turn has strong excitatory long-range connections with L5B of M1 (Hira et al., 2013b; Hooks et al., 2013; Weiler et al., 2008). M2 L2/3 activity is therefore two excitatory synapses upstream from M1 L5B activity. Is it possible that neural coding becomes sparser as one goes further away from the body and deeper into the CNS? Many sensory systems are organised such that the primary sensory cells (e.g. muscle spindle cells, retinal photoreceptors, olfactory receptor neurons) exhibit dense activity patterns during the presentation of most stimuli, but coding representations become increasingly sparse as one follows neural connections downstream towards the cortex (Babadi and Sompolinsky, 2014). Could the reverse be true for motor systems, with secondary motor cortex exhibiting sparse coding, which gets increasingly dense downstream? Downstream of L5B lies the brainstem and spinal circuits, which are technically challenging to record from (whether via electrophysiology or calcium imaging) during awake behaviour, but immediately upstream of L5B is L2/3, which is fortunately far more accessible. We will examine L2/3 population in the next chapter and compare the sparseness of L2/3 population coding with that of L5B during the execution of the same motor task.

5.4.3 Experimental limitations and future improvements

Out of the 851 L5B neurons recorded, 141 (16.6%) displayed significantly different pre-action baseline ΔF/F values. Since electrophysiological recordings indicate that movement-related neuronal activity in $M1_{FL}$ arises not more than 500 ms before movement onset (Evarts, 1974; Fu et al., 1995; Georgopoulos et al., 1982; Makino et al., 2017), it is unlikely that the differences in baseline directly related to the push or pull movements. Instead, they could be related to pre-existing differences in pre-action movement and/or differences in posture (including joint positions and muscle tensions) prior to movement onset. Nonetheless, the fact that 16.6% of recorded neurons displayed unequal baseline values indicates that the majority of neurons (83.4%) did not significantly reflect postural differences or differences in pre-action movement in their baseline activity.

To address these potential problems, several changes could be made to the experimental methods. Firstly, non-task-related forelimb movements prior to the onset of lever movement could be minimised. Notwithstanding the eagerness of mice to move, it is possible to train them to continuously rest their forelimbs on a lever before the onset of a task. Galiñanes et al. (2018) describe a directional mouse reaching task where mice must hold a "resting bar" for 2 s before a trial is initiated, and a touch detector circuit is used to detect when its forepaw is resting on the bar (Slotnick, 2009). This circuit can be fitted to the lever in our push/pull task, and the task reprogrammed such that the cue is withheld until the mouse maintains its forepaw on the lever for 2 s. If the mouse fails to do so, the trial will be aborted. While such restrictions would increase the difficulty of the task and elongate training, the payoff would be the elimination of limb repositioning (as described in Chapter 4) prior to the onset of push and pull trials.

Secondly, most GECIs including GCaMP6s are not optimised to detect decreases in Ca^{2+} concentration; they have low levels of fluorescence (and therefore low signal-to-noise) when neurons display low baseline firing rates and thus experience a floor effect when firing rates fall further (Hara-Kuge et al., 2018). In addition, the kinetics of GCaMP6s mean that ΔF/F rapidly rises in response to rising calcium levels, but decay slowly when calcium levels drop, so brief increases in activity are more visible than brief decreases in activity (Chen et al., 2013b). These two aforementioned reasons could account for why many electrophysiological studies in M1 find neurons that display decreased firing rates during movement (Caminiti et al., 1990; Georgopoulos et al., 1982; Schiemann et al., 2015), while almost all population calcium imaging studies in M1 do not report neurons with reduced activity (Galiñanes et al., 2018; Peters et al., 2014). While the analysis methods employed here were able to detect neurons that displayed decreased activity during movement, inverse-type calcium detectors may be able to better quantify decreases in neuronal activity. These GECIs increase their fluorescence in response to decreases in neural activity, and have far more rapid responses to calcium drops than GCaMP-type indicators (Hara-Kuge et al., 2018).

Like many areas of the mammalian cortex, mouse M1 is hierarchically organised, with layer 5 receiving strong inputs from layer 2/3 (L2/3). L2/3 -> L5 is the dominant intracortical pathway in rodent motor cortex (Beul and Hilgetag, 2015; Douglas et al., 1989; Kang, 1995; Shepherd, 2009), with strong excitatory connections between pyramidal neurons in L2/3 and pyramidal neurons in upper L5B. Determining if L2/3 and L5B share similar patterns of

population activity during the execution of a given task would advance our understanding of cortical coding. The next chapter will examine population coding of movement in L2/3 of $M1_{FL}$.

Chapter 6: Population activity in Layer 2/3 of mouse forelimb motor cortex

---

6.1 Introduction

Verum, sine mendacio, certum et verissimum. Quod est inferius est sicut quod est superius, et quod est superius est sicut quod est inferius, ad perpetranda miracula rei unius.

- *Latin text of the Emerald Tablet*

True it is, without falsehood, certain and most true. That which is above is like to that which is below, and that which is below is like to that which is above, to accomplish the miracles of one thing.

- *English translation of the Emerald Tablet (Linden, 2003)*

While layer 5B is the primary output layer of motor cortex, all cortical layers are intricately interconnected in recurrent loops, and each contributes to the final output. Excitatory projections from layer 2/3 (L2/3) to L5 neurons constitute an important component of the canonical neocortical microcircuit, and this is the dominant inter-layer pathway within rodent motor cortex (Anderson et al., 2010; Beul and Hilgetag, 2015; Douglas et al., 1989; Kang, 1995; Shepherd, 2009). Hermes Trismegistus was probably not referring to layer-specific cortical coding when he wrote the Emerald Tablet, but the text nonetheless offers a testable hypothesis regarding cortical coding. Is population neuronal activity in the upper layers of $M1_{FL}$ similar to population neuronal activity in the lower layers of $M1_{FL}$ during the execution of a given movement? Do L2/3 neurons exhibit the same kind of direction-specific activity patterns as L5B neurons? This chapter examines population activity in L2/3 during the execution of a push/pull lever task, using the same experimental and analysis tools as in Chapter 5.

6.1.1 Layer 2/3 in the motor cortex

While the cerebral cortex is generally considered to be divided into layers 1 to 6 during embryogenesis, layer 2 (the external granular layer) and layer 3 (the external pyramidal layer) are generally merged into a single layer by the time a mammal reaches adulthood, and are collectively termed layer 2/3 (Brodmann, 2006). The cortex in M1 is considered to be agranular (that is, lacking a distinct layer 4, or possibly having a very thin layer 4) (Yamawaki et al., 2014), so effectively L2/3 in M1 lies directly above L5. Layer 2/3 neurons in rodent M1 receive a range of long-range inputs from sensory thalamus, motor thalamus, frontal cortex, and somatosensory cortex, as well as recurrent input from L2/3, L5, and L6 neurons in the same cortical region (Douglas and Martin, 2007; Hooks et al., 2011, 2013; Reep et al., 1990).

In turn, L2/3 pyramidal neurons in M1 provide strong feedforward excitatory input to L5A and L5B. Retroviral tracing and photostimulation experiments have shown that that many L2/3 neurons directly synapse with corticospinal neurons in L5B of M1 in primates and mice, respectively (Hooks et al., 2013; Rathelot and Strick, 2009; Weiler et al., 2008; Yu et al., 2008). Considering the strength of their anatomical and functional connections, it is likely that L2/3 and L5B operate as a cohesive unit in the production of motor cortical output. Examining population activity in L2/3 would inform us if push- and pull-specific activity patterns are exclusive to L5B, or are already present further upstream in L2/3. Moreover, imaging L2/3 population activity would allow us to test the hypothesis generated in Chapter 5, that coding of motor control signals becomes sparser as a function of distance from lower motor neurons.

6.2 Materials and methods

The methods used for acquiring and processing calcium imaging data from L2/3 were identical to those described in the previous chapters. Calcium imaging data from L2/3 were acquired at depths ranging from 200 to 300 μm below the pial surface. This depth range was purposely selected as a conservatively narrow estimate of the L2/3 boundary in $M1_{FL}$ (Masamizu et al., 2014).

6.3 Results

A total of N = 19 non-overlapping fields of view were recorded in L2/3 of $M1_{FL}$ in 11 mice, containing a total of 1322 neurons. Using the same methods as described in Chapter 5, 379 posture neurons and 86 non-task-related neurons were excluded, leaving a total of 857 task-related neurons for further analysis, or 64.8% of the sampled population of neurons.

6.3.1 Average neuron density in L2/3 of primary motor cortex

As with L5B, a major concern was whether our L2/3 calcium imaging sessions sampled all the neurons physically present in L2/3 imaging planes. To confirm this, I quantified the mean neuron density using the same histological methods as described in Chapter 4, and compared this against the average neuron density observed in L2/3 calcium imaging FOVs (Figure 6.1).

The average neuronal density in L2/3 was calculated by counting the number of NeuN-stained neurons in the centre of $M1_{FL}$ in n = 3 sections from one mouse brain. This value was then compared to the average density of GCaMP6s positive neurons acquired from n = 19 L2/3 FOVs. The neuronal density in L2/3 was 22.6 ± 0.2 neurons per 100 μm^2, while the neuronal density measured by GCaMP6s labelling was 11.6 ± 0.7 neurons per 100 μm^2 (mean ± s.e.m.). This difference was statistically significant (d.f. = 20, $p < 0.001$, two-sample *t*-test), indicating that two-photon imaging was not able to detect all neurons in the L2/3 population.

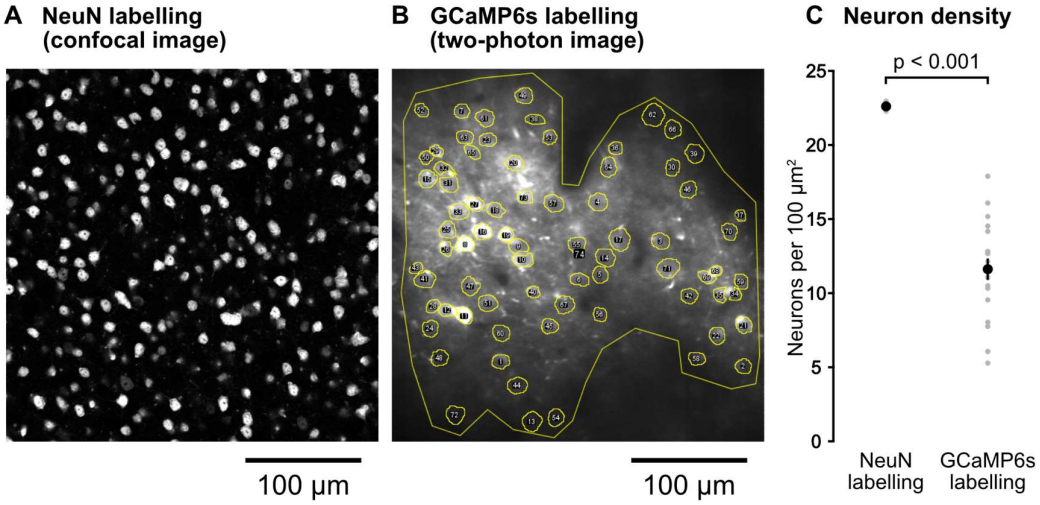

Figure 6.1: Neuron density in L2/3. ***A)*** *A sample confocal image of L2/3 neurons, with their nuclei stained with a primary mouse anti-NeuN antibody and a secondary goat anti-mouse secondary antibody.* ***B)*** *A sample 2-photon image of L2/3 neurons expressing GCaMP6s. The yellow circles are ROIs drawn around identified neuronal cell bodies, while the large yellow outline is an estimation of the area where neurons are present.* ***C)*** *Average L2/3 neuronal density measured by counting NeuN and GCaMP6s labelling.*

As expected, neurons in L2/3 were noticeably smaller in diameter than L5B neurons and were more densely packed, with NeuN staining revealing an average of 22.6 neurons per 100 µm^2 in L2/3 and 15.6 neurons per 100 µm^2 in L5B. However, the density as measured by calcium imaging was significantly lower in L2/3, at only 51.4% the density measured by NeuN labelling, suggesting that calcium imaging was unable to detect approximately half the neurons in L2/3. Given that the same virus was used for all imaging sessions, and that the signal-to-noise ratio was higher in L2/3 when compared to L5B (as light scattering increases as a function of depth from the pial (Denk and Svoboda, 1997)), it is likely that this difference was due to lower baseline activity levels in L2/3 neurons as most L2/3 pyramidal neurons display low baseline firing rates of <1 Hz (Petersen and Crochet, 2013; Poulet and Petersen, 2008). While imaging with GCaMP6s can potentially detect single spikes in single L2/3 neurons under ideal conditions (Chen et al., 2013b), non-optimal recording conditions *in vivo* may leave some low firing rate neurons undetected.

6.3.2 Heterogeneous activity patterns of task-related L2/3 neurons

L2/3 neurons exhibited a diverse range of movement-related activity patterns. To distil this large data set into a more understandable taxonomy, the remaining n = 857 neurons were classified based on their dissimilarity indices (DIs) providing a comparison with the L5B data in Chapter 5. Similar to observations in L5B, there was a subpopulation of neurons (598 neurons, 69.8%) with a dissimilarity index ≈ 0, as shown in Figure 6.2 below.

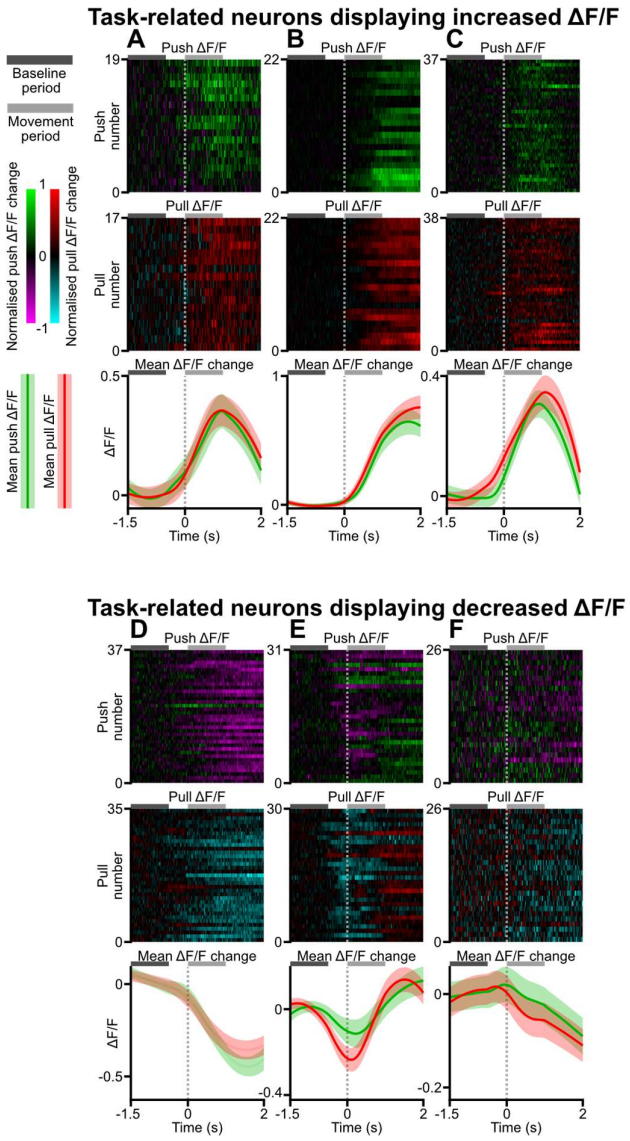

Figure 6.2: Examples of movement-related ΔF/F changes in L2/3 neurons with a dissimilarity index ≈ 0. ***A-C)*** *Movement-related ΔF/F changes in 3 representative neurons that show a significant increase in ΔF/F during both push and pull trials. The upper heat map depicts ΔF/F during individual push trials, while the middle heat map depicts ΔF/F during individual pull trials. Each row represents one successful push or pull trial, and the heat maps were normalised to the maximum and minimum ΔF/F values of that neuron across all trials. The dark grey bar depicts the 1 s baseline period, while the light grey bar depicts the 1 s movement-related period. The lower plot depicts mean ΔF/F smoothed with a 2-second-wide loess filter, with mean push ΔF/F in green and mean pull ΔF/F in red ± s.e.m. The dotted vertical line indicates the time of movement onset.* ***D-F)*** *Movement-related ΔF/F changes in 3 representative neurons that show a significant decrease in ΔF/F during both push and pull trials.*

I observed a subpopulation of task-related neurons which increased their ΔF/F values during both push and pull trials, and another subpopulation which exhibited decreased ΔF/F values during both push and pull trials. These data suggest that a large proportion of L2/3 neurons encode information related to the onset of lever movement, but not information specific to push or pull actions. Instead, it appears likely that direction-specific information is encoded in the subpopulation of L2/3 neurons (n = 271/857 neurons, i.e. 30.2% of all L2/3 neurons) with dissimilarity indices greater than 1.3 or less than -1.3 (Figure 6.3).

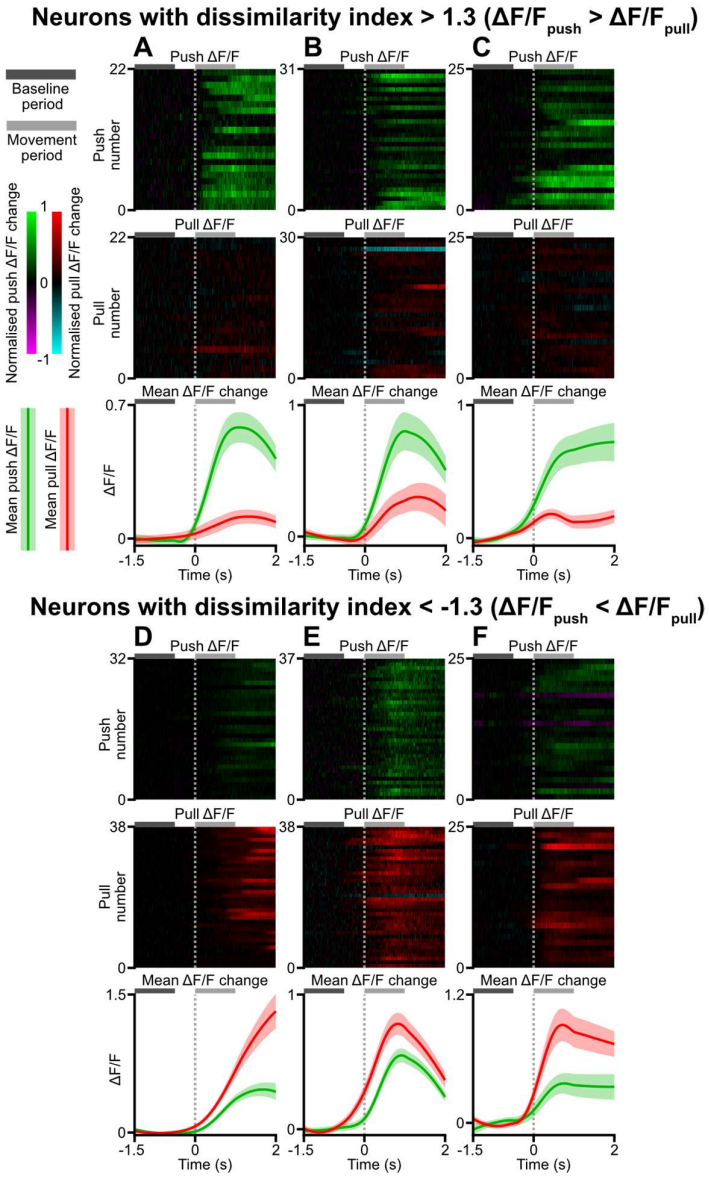

Figure 6.3: Examples of task-related L2/3 neurons with dissimilarity indices > 1.3 or < -1.3. ***A-C)*** *Movement-related ΔF/F changes in 3 representative neurons that show a significant increase in ΔF/F during both push and pull trials, and a dissimilarity index > 1.3 due to* $\Delta F/F_{push} > \Delta F/F_{pull}$*. The upper heat map depicts ΔF/F during individual push trials, while the middle heat map depicts ΔF/F during individual pull trials. Each row represents one successful push or pull trial, and the heat maps were normalised to the maximum and minimum ΔF/F values of that neuron across all trials. The dark grey bar depicts the 1 s baseline period, while the light grey bar depicts the 1 s movement-related period. The lower plot depicts mean ΔF/F smoothed with a 2-second-wide loess filter, with mean push ΔF/F in green and mean pull ΔF/F in red ± s.e.m. The dotted vertical line indicates the time of movement onset.* ***D-F)*** *Movement-related ΔF/F changes in 3 representative neurons that show a significant increase in ΔF/F during both push and pull movements, and a dissimilarity index < -1.3 due to* $\Delta F/F_{push} < \Delta F/F_{pull}$.

In summary, a small proportion of L2/3 neurons displayed a DI > 1.3 (60 neurons/7.0%), where ΔF/F values increased during both push and pull trials but with push-related ΔF/F changes being larger. In addition, I observed a larger subpopulation with DI < -1.3, where ΔF/F values increased during both push and pull trials but with pull-related ΔF/F changes being larger (119 neurons/23.2%). Surprisingly, unlike L5B, there was a noticeable lack of neurons with decreasing push-related ΔF/F, which will be discussed later.

6.3.3 Task-related activity in L2/3 neurons

To obtain an overview of population activity in L2/3 task-related neurons, heat maps were plotted to display mean ΔF/F changes across push and pull trials (Figure 6.4).

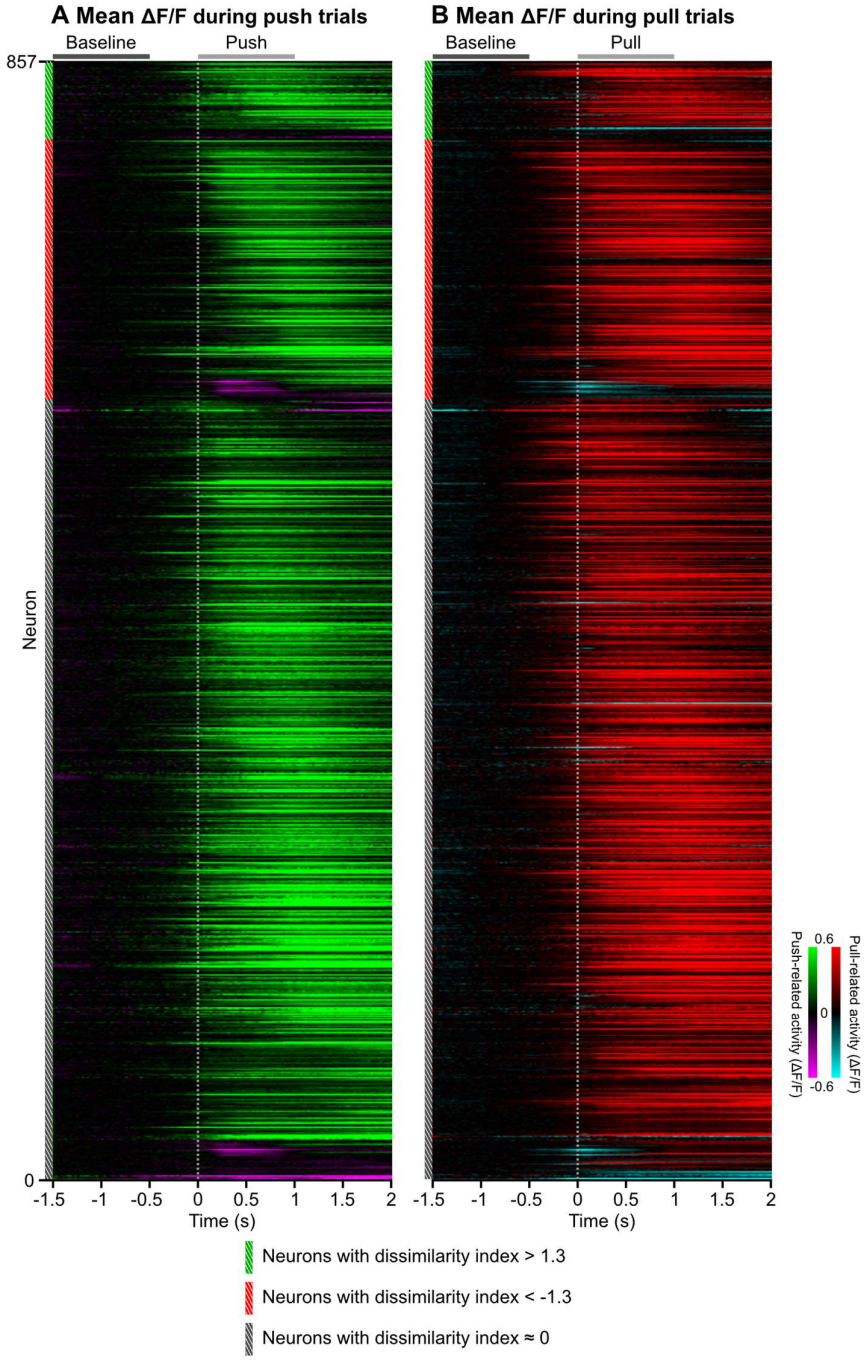

Figure 6.4: Heat maps of ΔF/F changes in task-related L2/3 neurons. ***A)*** *Heat map of mean push-related changes in ΔF/F. Each row represents a neuron, with the colours indicating the mean change in ΔF/F from its baseline. The hatched bars on the left represent neuron classification. From top to bottom on the left, neurons were sorted by 1) neuron classification, 2) increasing or decreasing ΔF/F during the movement period and 3) by peak ΔF/F. ΔF/F values were not smoothed or normalised. The dark grey bar depicts the 1 s baseline period, while the light grey bar depicts the 1 s movement-related period. The dotted vertical line indicates the time of movement onset.* ***B)*** *Heat map of mean pull-related changes in ΔF/F organised as in*

A), except that the neurons/rows were not sorted and correspond to the same neurons shown in A).

The overview of ΔF/F changes in task-related L2/3 neurons identified that the majority displayed increased activity during both push and pull trials. However, in L2/3, there were more neurons with dissimilarity index < -1.3 than neurons with dissimilarity index > 1.3, which displayed larger ΔF/F increases during pull trials than push trials: which is the opposite of that observed in L5B.

To visualise how mean action-related activity compared across fields of view, task-related neuronal activity was plotted, grouped by field of view (Figure 6.5).

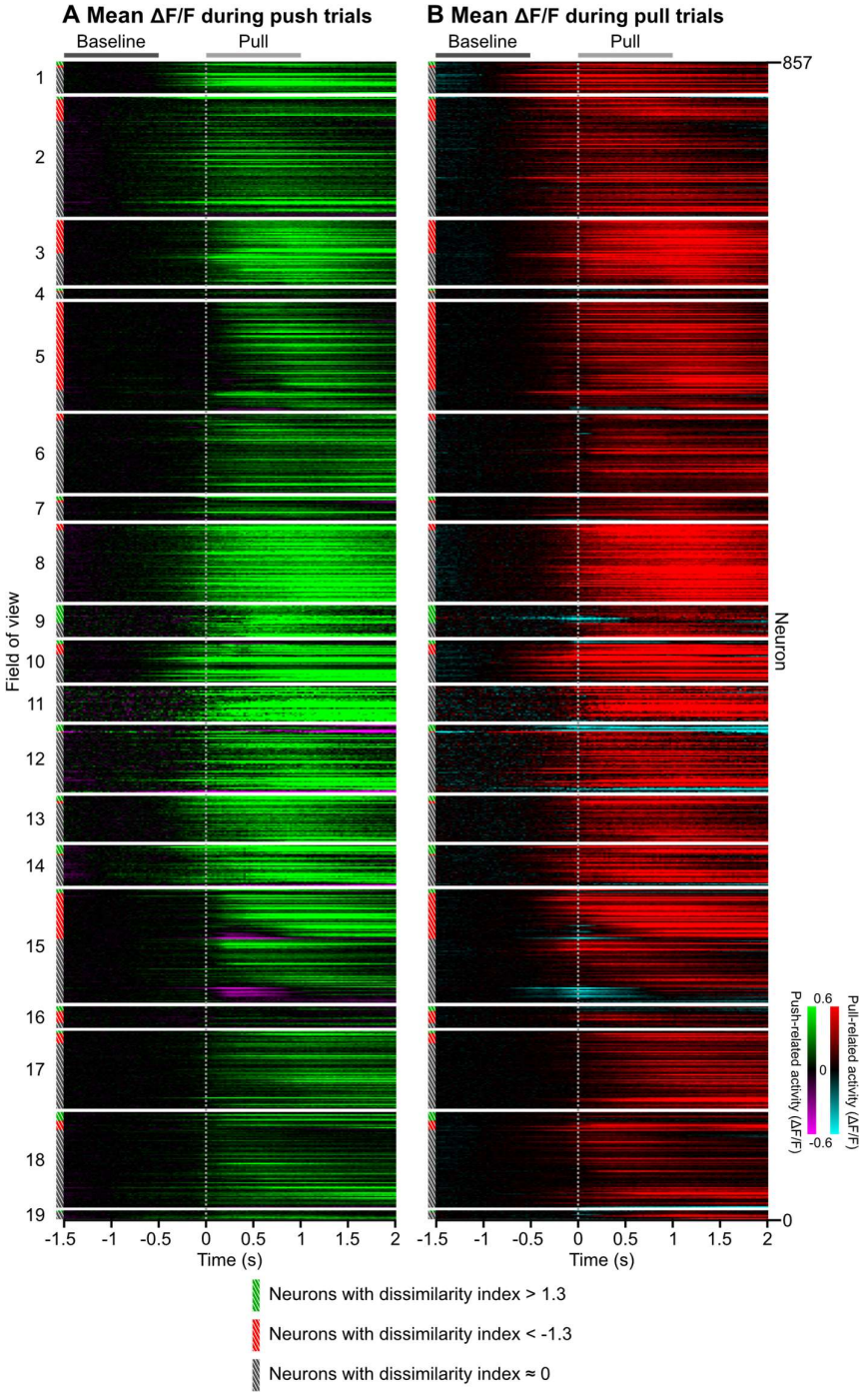

Figure 6.5: Heat maps of ΔF/F changes in task-related L2/3 neurons, grouped by field of view. ***A)*** *Heat map of mean push-related changes in ΔF/F. Each row represents a neuron, with the colours indicating the mean change in ΔF/F from its baseline. The hatched bars on the left represent neuron classification. From top to bottom on the left, neurons were sorted by 1) field of view 2) neuron classification, 3) increasing or decreasing ΔF/F during the movement period and 4) by peak ΔF/F. ΔF/F values were not smoothed or normalised. The dark grey bar depicts the 1 s baseline period, while the light grey bar depicts the 1 s movement-related*

period. The dotted vertical line indicates the time of movement onset. ***B)*** *Heat map of mean pull-related changes in ΔF/F organised as in A), except that the neurons/rows were not sorted and correspond to the same neurons shown in A).*

Dissimilarity indices were not evenly distributed among individual fields of view, and each field of view contained different proportions of each neuronal category. To provide an overview of the task-related changes in ΔF/F changes across the L2/3 population, each ROI within a field of view was plotted and colour coded according to their 1) average movement-related ΔF/F during push and pull trials (Figure 6.6) or 2) dissimilarity index (Figure 6.7).

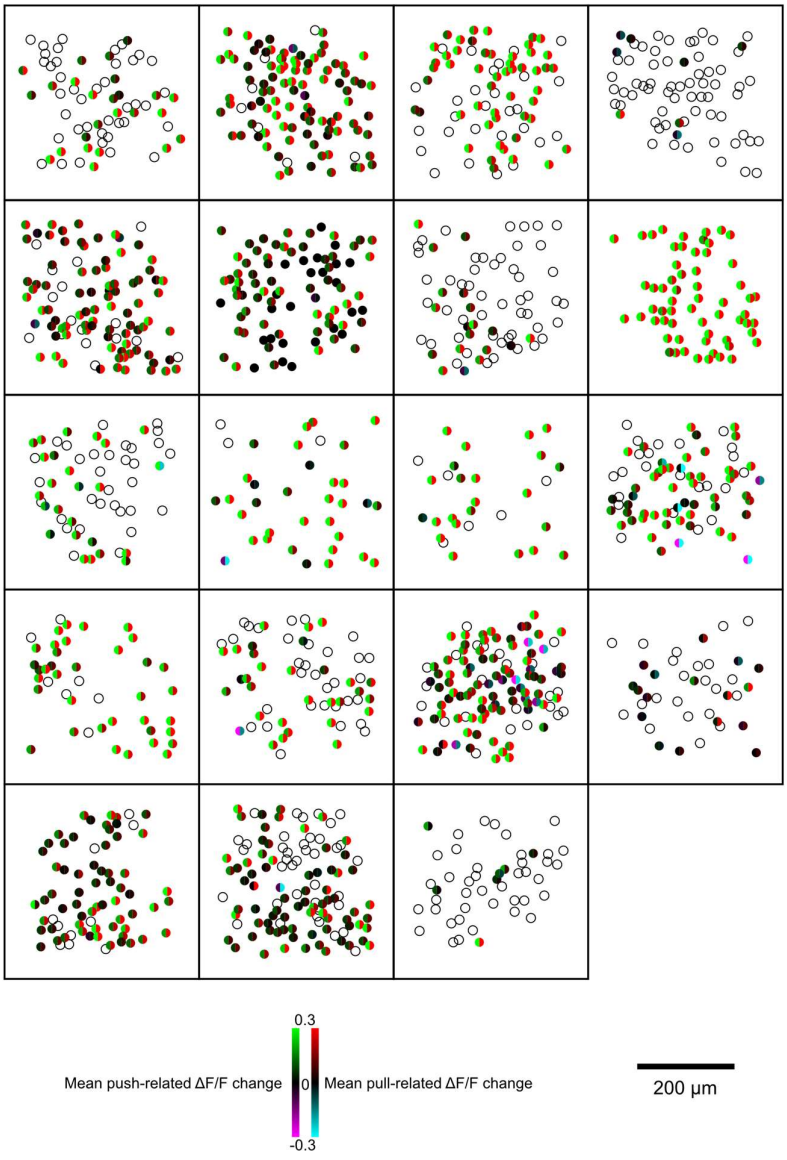

Figure 6.6: Overview of ΔF/F changes in task-related L2/3 neurons grouped by field of view. Each square represents a field of view and each circle represents an individual neuron. The spatial position of each circle plotted here corresponds to the position of the neuron's centre in the actual field of view. Neurons excluded due to unequal baselines (i.e. posture neurons) or due to being non-task-related are depicted as empty circles. Task-related neurons are plotted as coloured circles with the left half indicating its mean push-related ΔF/F change and right half indicating mean pull-related ΔF/F change. From left to right and top to bottom, each field of view is in the same order as the heat map shown in Figure 6.5 above.

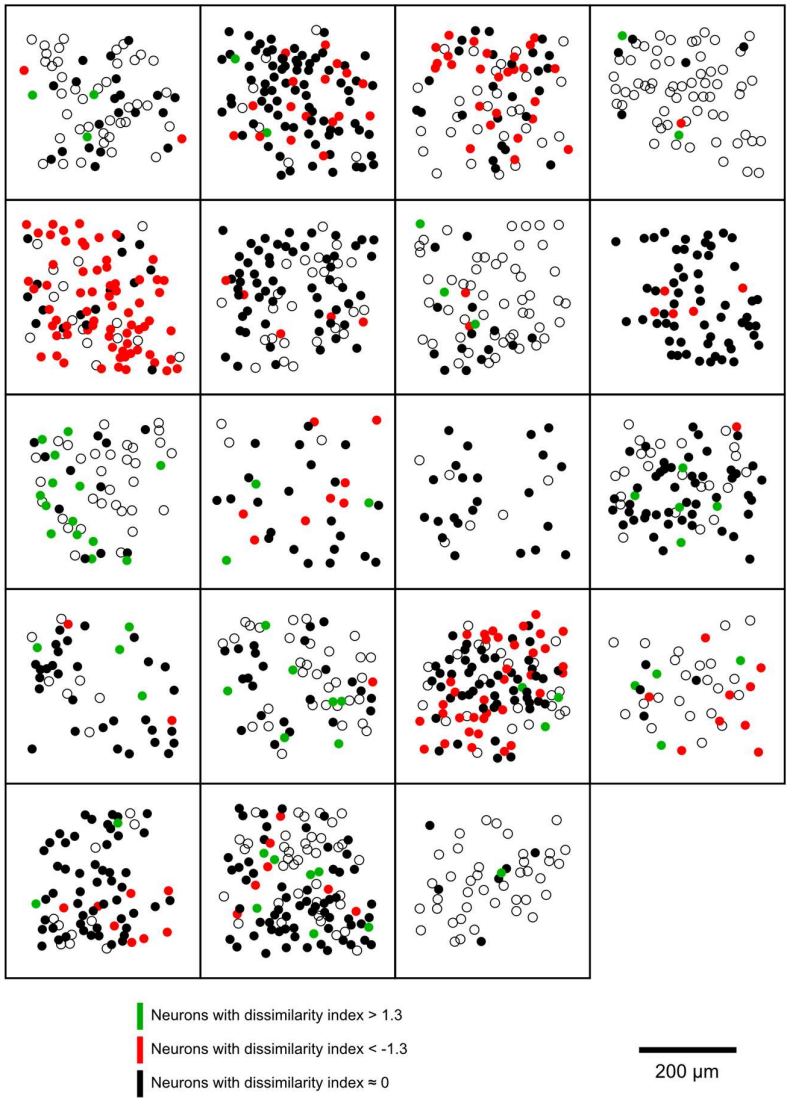

Figure 6.7: Overview of dissimilarity indices in task-related L2/3 neurons grouped by field of view. Each square represents a field of view and each circle represents an individual neuron. The spatial position of each circle plotted here corresponds to the position of the neuron's

centre in the actual field of view. Neurons excluded due to unequal baselines (i.e. posture neurons) or due to being non-task-related are depicted as empty circles. Task-related neurons are plotted as coloured circles with the left half indicating its mean push-related ΔF/F change and right half indicating mean pull-related ΔF/F change. From left to right and top to bottom, each field of view is in the same order as the heat map shown in Figure 6.5 above.

I found that individual fields of view displayed highly divergent task-related activity patterns, with no obvious general organisation of neurons into cortical columns. Many FOVs were dominated by neurons with DI < -1.3 (e.g. #5), with only two FOVs having a preponderance of neurons with DI > 1.3 (e.g. #9 and #12). In addition, there were other FOVs with apparently random distributions of neurons from each category (e.g. #1). The distribution of task-related and non-task-related neurons appeared rather inhomogeneous, with FOV #4 containing few task-related neurons, and FOV #8 containing no non-task-related neurons. Similar to L5B, these findings suggest a lack of topographical organisation of DI-based neuronal categories in L2/3. This lack of structure also conflicts with the repeating column model of motor cortical organisation proposed by Georgopoulos et al. (2007).

6.3.4 Overview of task-related neural activity

In contrast to L5B, L2/3 contained a larger number of neurons with positive dissimilarity indices. To provide an overview of neuron classification, and therefore an insight into how $M1_{FL}$ neuronal populations in L2/3 encode directional movement, I plotted the mean push-related ΔF/F change as a function of pull-related ΔF/F for each task-related neuron (Figure 6.8).

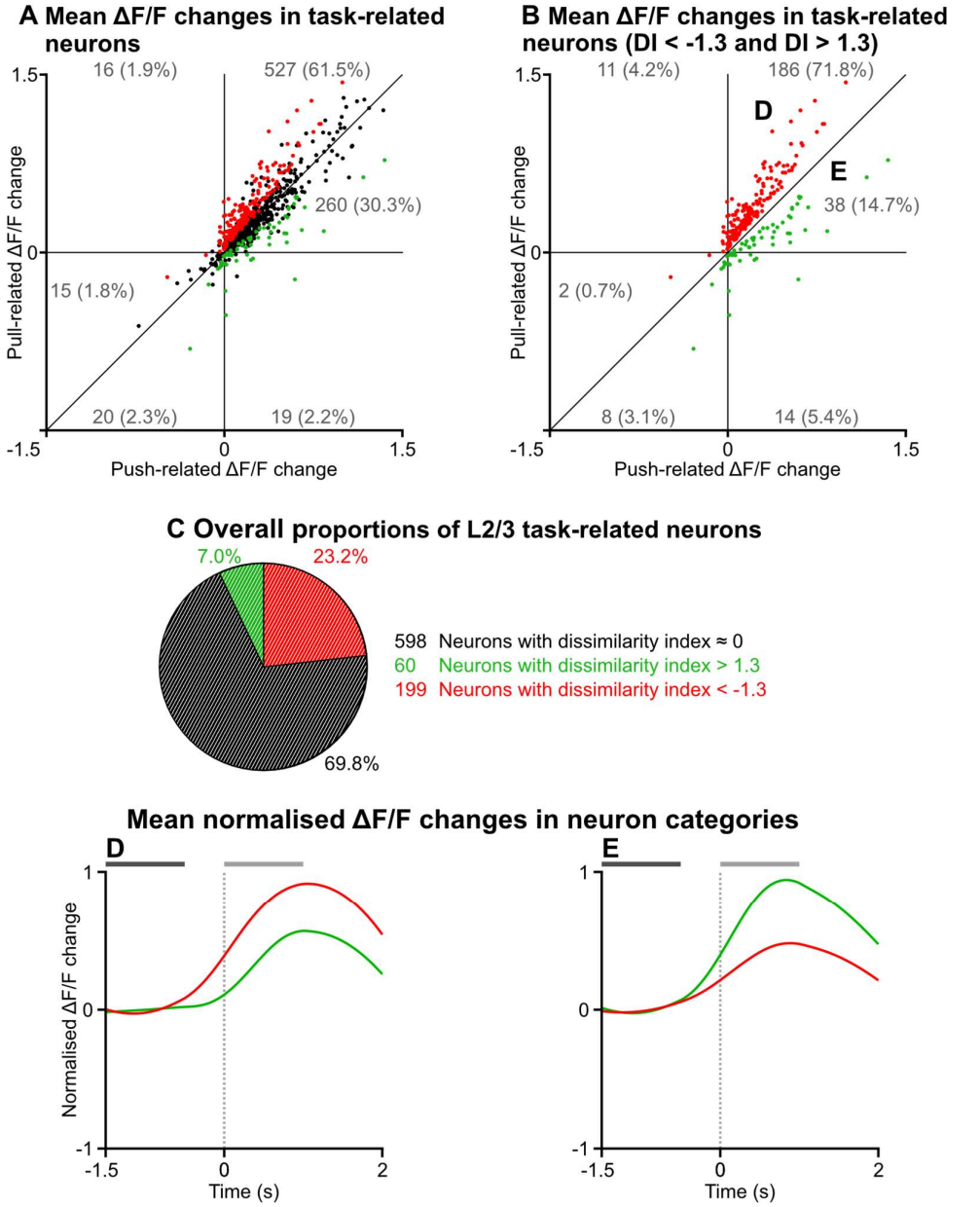

Figure 6.8: Overview of mean task-related ΔF/F changes in L2/3 neurons across all fields of view. ***A)*** *A total of 857 task-related neurons, with mean change in push-related ΔF/F plotted against mean change in pull-related ΔF/F. Green and red circles represent neurons with significant push/pull dissimilarity, and black circles represent neurons with a dissimilarity index ≈ 0. The grey numbers in each sector indicate the number of neurons in that sector of the graph and the percentage of the overall population in brackets.* ***B)*** *Same graph as A), with neurons with a dissimilarity index ≈ 0 removed.* ***C)*** *Pie chart summarising the number of neurons in each category and the percentage of the whole population.* ***D-E)*** *Graphs depicting mean normalised ΔF/F changes in the two neuronal subpopulations labelled in B). The dark grey bar depicts the 1 s baseline period, and a light grey bar depicts the 1 s movement-related period. The dotted vertical line indicates the time of movement onset.*

The majority of L2/3 neurons displayed task-related activity during the execution of the push/pull lever task, suggesting L2/3 plays a role in the generation of motor output. These task-related neurons had similar push-related and pull-related ΔF/F changes (69.8%), lie close to the identity line and have a dissimilarity index close to zero. The remaining neurons either had dissimilarity indices > 1.3 (23.2%) or dissimilarity indices < -1.3 (7.0%). However, while more L5B neurons displayed dissimilarity indices > 1.3 (>1.3 = 20.5% vs <-1.3 = 11.7%), the reverse was true in L2/3 (>1.3 = 7.0% vs <-1.3 = 23.2%). Applying a chi-squared test for independence found that the distribution of neurons in the three categories (dissimilarity index ≈ 0 / dissimilarity index > 1.3 / dissimilarity index < -1.3) were significantly different from the distributions observed in L5B (d.f. = 2, $\chi^2 = 74.0$, $p < 0.001$).

Moreover, while most L5B neurons with non-zero dissimilarity indices fell into 3 groups each containing ~30% of the total neuronal population, in L2/3 the vast majority of neurons could be grouped into two categories (labelled **D** and **E**). There was a noticeable paucity of L2/3 task-related neurons which exhibited a reduction in ΔF/F during movement. This could reflect differences in how each layer encodes movement, however, I suggest that this result was primarily due to sampling bias. L2/3 excitatory neurons have significantly lower firing rates when compared to L5B excitatory neurons, often as low as < 1 Hz (Petersen and Crochet, 2013; Poulet and Petersen, 2008). The kinetics of GCaMP6s and dynamics of ΔF/F changes are subject to a floor effect at low levels of neuronal activity (Chen et al., 2013b). This means that neurons which display low baseline firing rates that reduce further upon task execution (e.g. 0.5 Hz to 0.25 Hz) may be transmitting crucial task-specific information to downstream neurons, but this decrease in activity would likely go undetected.

6.4 Discussion

The aim of this chapter was to address the basic but fundamentally important question: how are two diametrically opposing movements represented in L2/3 population activity, and how does L2/3 population activity compare with L5B population activity during the execution of the same movements?

6.4.1 Action-specific coding in L2/3 neuronal populations

L2/3 neurons were found to demonstrate direction-specific patterns of activity in similar proportions when compared to L5B neurons. While the vast majority of L5B neurons displayed dissimilarity indices of > 1.3, the majority of L2/3 neurons displayed dissimilarity indices of < -1.3. It is worth noting that in a task with binary outcomes like the push/pull lever task, any change in activity from baseline can potentially encode motor output. While many neurophysiological studies implicitly assume that changes in neuronal activity are equivalent to increased firing rates, neurons can encode and transmit information to downstream targets via a multitude of other coding schemes such as phase shifts, spike count correlations, or even suppressed firing rates. Since the coding schemes present in mouse $M1_{FL}$ are not known, we cannot assume a priori that a greater increase in ΔF/F is more important in terms of population coding. Suppression of neuronal firing in certain neurons may be equally or more important when generating volitional skilled movements. Nonetheless, the fact that L2/3 populations and L5B populations behave differently during execution of the same task is an important finding. Below I propose several hypotheses which may explain this apparent disparity in layer-specific activity, and the means by which they can be tested.

One possibility is that there are cortical maps in $M1_{FL}$ that represent individual movements. A previous study using mice found that L5B corticospinal neurons in the rostral forelimb area (RFA) preferentially activate during forelimb extensions, while neurons in the caudal forelimb area preferentially activate during forelimb retractions (Wang et al., 2017). Another complementary study found that stimulating L5B pyramidal neurons in the RFA produced forelimb abductions, while stimulating L5B pyramidal neurons in the CFA produced forelimb adductions (Harrison et al., 2012). Interestingly, the coordinates we used for $M1_{FL}$ (1.6 mm

lateral and 0.6 mm rostral from bregma) lie directly between the forelimb-abduction (i.e. push) and forelimb-adduction (i.e. pull) regions described in these studies. If the topography of these maps were variable across different mice, similar to how cortical representations of specific movements in primate M1 differ across individuals and training periods (Nudo et al., 1996; Plautz et al., 2000), it would explain why we observed different distributions of neuronal DIs across different FOVs, as seen in Figure 5.10 and Figure 6.7. It would be possible to empirically test this idea in future experiments involving the same behaviour, by employing wide-field calcium imaging where the field of view is large enough to capture all of $M1_{FL}$: if different sub-regions within $M1_{FL}$ are mapped to either push or pull trials these would be visible in the larger field of view.

However, the hypothesis described in Figure 6.9A alone does not explain the differences between the predominantly negative neuronal DIs observed in L2/3 FOVs versus the predominantly positive neuronal DIs observed in L5B FOVs. The possibility exists that most L5B fields of view were randomly selected from a 'push-related' region and most of the L2/3 fields of view from a 'pull-related' region. This possibility could be tested by simultaneous imaging of L2/3 and L5B in the same cortical column, to determine if direction preference is preserved across lamina.

One possible circuit scheme, depicted in Figure 6.9B, is that pyramidal neurons in L2/3 provide strong feedforward input to inhibitory neurons in L5B. This feedforward inhibitory network organisation has previously been proposed (Apicella et al., 2012; Otsuka and Kawaguchi, 2009). In this scenario, L2/3 pyramidal neurons that preferentially activate during pull trials would drive a net inhibition of L5B neurons resulting in higher ΔF/F changes during push trials. However, despite L2/3 pyramidal neurons producing strong disynaptic inhibition of L5 pyramidal neurons, they also provide significant monosynaptic excitatory input which overrides inhibition to produce a net excitatory influence (Apicella et al., 2012; Weiler et al., 2008). This functional anatomical arrangement would suggest that the scenario depicted in Figure 6.9B is unlikely.

One alternative explanation, as illustrated in Figure 6.9C, would be that pyramidal neurons mostly exhibit higher ΔF/F changes during push trials in both L5B and L2/3 (i.e. DI > 1.3), while inhibitory interneurons which inhibit these pyramidal neurons exhibit higher ΔF/F changes during pull trials (i.e. DI < -1.3). However, ΔF/F decreases in the L2/3 pyramidal neurons are not observable under two-photon imaging, due their extremely low baseline firing rates of

<1 Hz (Petersen and Crochet, 2013; Poulet and Petersen, 2008). Instead, we primarily observe the inhibitory interneurons in L2/3 which have DI < -1.3. Therefore, even though the L2/3 and L5B populations produce similar patterns of activity during push and pull trials, L2/3 neurons are mostly classified as having DI < -1.3, and L5B neurons tend to be classified as having DI > 1.3. However, this is also an unlikely scenario, as only 20% of cortical neurons are inhibitory neurons, and interneurons are interspersed among pyramidal neurons in the cortex (Espuny-Camacho et al., 2013).

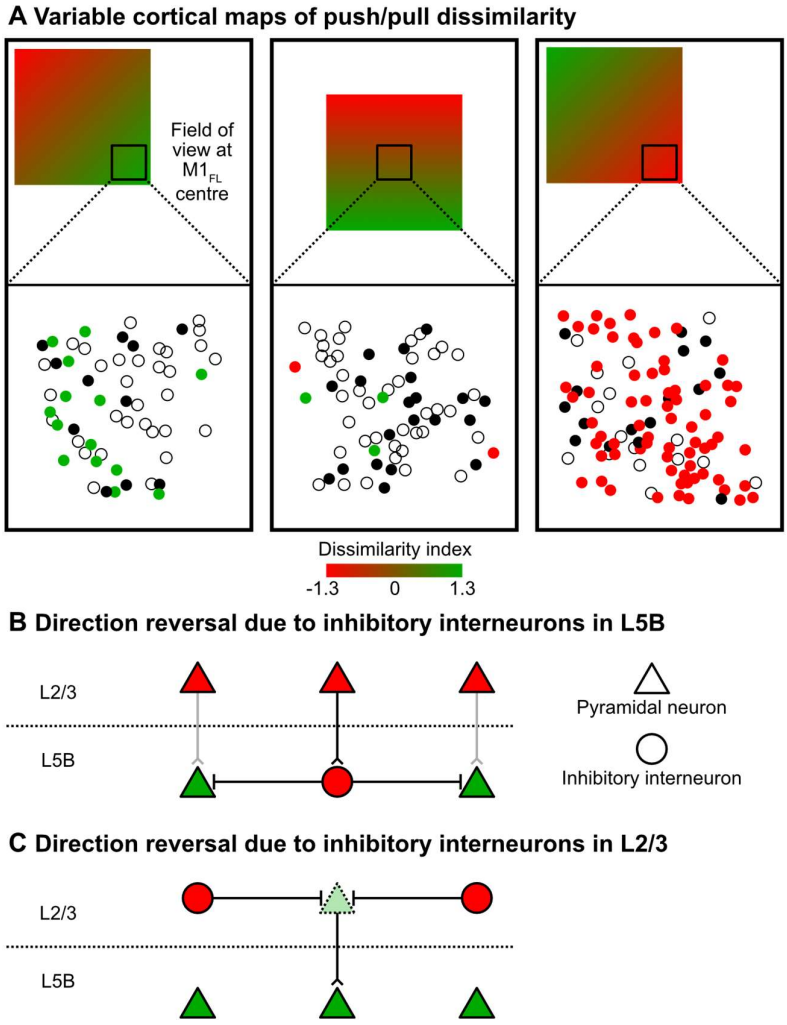

Figure 6.9: Three hypotheses which explain the disparity between L2/3 and L5B in terms of neuronal dissimilarity indices. ***A)*** *There are cortical maps corresponding to push and pull trials in $M1_{FL}$. These are variable between animals, so fields of view at the same anatomical coordinates can contain different proportions of neurons with dissimilarity index > 1.3 or < -1.3.* ***B)*** *L2/3 pyramidal neurons project to inhibitory interneurons in L5B, so higher pull-related*

activity in L2/3 results in lower pull-related activity in L5B. ***C)*** *Pyramidal neurons in L2/3 and L5B both have higher activity levels during pushes, but L2/3 pyramidal neurons have low firing rates which are not easily observed during calcium imaging, therefore L2/3 imaging mostly captures increased ΔF/F in inhibitory interneurons which behave in the opposite manner.*

Having rejected some of the hypotheses, it would appear that hypothesis A) best explains our observations of neuronal DIs in L5B and L2/3 populations. Ultimately, to understand how activity across different cortical layers of $M1_{FL}$ is integrated to produce behaviourally-relevant motor output, it will be necessary to dissect the circuits at the cellular level during the execution of directional forelimb movement. For example, by expressing a calcium-independent marker such as red fluorescent protein (RFP) specifically in the pyramidal neuron subpopulation (via an AAV construct integrating a CaMKII promoter) (Wang et al., 2013), and then repeating the experiment described in this chapter. Activity in excitatory and inhibitory neuronal subpopulations could thereby be separated and compared, to determine if differences in neuronal DI observed during task execution were related to neuron type. The expression of a calcium-independent fluorescent marker in pyramidal neurons would also reveal those which are normally silent and invisible under GCaMP6s imaging.

6.4.2 Sparseness of the population code in L2/3

Superficially, it appears that the coding of movement in L2/3 is equally as sparse as the coding of movement in L5B. Similar proportions of neurons displayed action-related activity, and dissimilarity indices > 1.3 or < -1.3. However, this might be yet another instance of silent neurons biasing population observations (Shoham et al., 2006). Considering that NeuN staining and confocal imaging accurately describe the density of neurons in each imaging plane regardless of *in vivo* activity levels, it is possible to estimate the proportion of silent neurons which were undetectable due to low baseline fluorescence levels (Figure 6.10). The actual numbers of neurons in each field of view, and the number of silent neurons, can be estimated by:

$$\text{Neuron count per FOV}_{estimated} = \text{Neuron count per FOV}_{observed} \times \frac{\text{Neuron density}_{NeuN\ labelling}}{\text{Neuron density}_{Calcium\ imaging}}$$

$$\text{Silent neuron count per FOV} = \text{Neuron count per FOV}_{estimated} - \text{Neuron count per FOV}_{observed}$$

	L2/3 observed	L5B observed	L2/3 estimated	L5B estimated
Silent neurons	-	-	1250 (48.6%)	147 (14.7%)
Non-task-related	465 (35.2%)	288 (33.8%)	465 (18.1%)	288 (28.9%)
Task-related, DI ≈ 0	598 (45.2%)	382 (44.9%)	598 (23.3%)	382 (38.3%)
Task-related, DI <-1.3 or > 1.3	259 (19.6%)	181 (21.3%)	259 (10.1%)	181 (18.1%)
Total neurons	1322 (100%)	851 (100%)	2572 (100%)	998 (100%)

Figure 6.10: Table of estimated cell numbers per FOV in L2/3 and L5B.

These estimates would suggest that L2/3 is far less active than L5B during the execution of the task, with a higher proportion of silent neurons (L2/3 48.6% vs L5B 14.7%) and a lower proportion of task-related neurons (L2/3 33.4% vs L5B 56.4%). Our findings are consistent with other studies in L2/3 and L5B of motor areas in mice. Previous findings using calcium imaging in mouse M2 during a tri-directional reaching task found that only 10% of L2/3 neurons exhibited task-related activity during any of the 3 reach directions (Galiñanes et al., 2018). Moreover, an alternative study which performed calcium imaging in L2/3 of mouse vibrissal M1 during a go/no go sensorimotor licking task found that only a small proportion of neurons were active during specific timepoints during the task (3% active during touch, 26% during whisking, 9% during licking, and 4% during more than one timepoint) (Huber et al., 2012), further suggesting that L2/3 neurons are generally inactive and display sparse activation to represent specific features of behaviour. In contrast, a study focusing on population imaging in L5B of mouse M1 during a licking task found that 58% of L5B neurons were task-related (Li et al., 2015). Another study involving multi-unit electrophysiological recordings in L5B of rat $M1_{FL}$ found that 55% of pyramidal neurons produced task-related

patterns of activity when trained animals performed reaches (Li et al., 2017). In summary, there is a general agreement across a variety of species and forelimb behavioural tasks that in M1, L2/3 neurons exhibit sparser patterns of task-related activity than L5B neurons.

While the presence of silent neurons in L2/3 would be best confirmed with the use of calcium-independent markers such as RFP, our results agree that population coding in L2/3 is indeed sparser than that in L5B. This would be consistent with a model of motor cortical coding where L2/3 neuronal populations encode more specific aspects of behaviour.

This page was intentionally left blank.

Chapter 7: Decoding population activity in forelimb motor cortex

7.1 Introduction

Having examined how neuronal populations in layer 2/3 and layer 5B of mouse $M1_{FL}$ encode two diametrically opposing movements, this chapter will examine whether behavioural outcome can be decoded from L5B population activity.

7.1.1 Neural encoding and decoding, revisited

Understanding neural encoding in the context of mammalian M1 entails the study of how known motor outputs are represented in terms of neuronal activity. Neuronal decoding is the obverse of neural coding: the prediction of motor outputs from known neuronal activity. Decoding is also an acid test for the neural coding of a particular feature in population activity, because if the feature (e.g. movement direction) can be successfully decoded, then it must have been encoded in the population activity (Averbeck et al., 2006). Neuronal decoding has become an increasingly important topic in recent years, due to the growing focus on research in brain-computer interfaces (BCIs) (Lance et al., 2012; Nicolas-Alonso and Gomez-Gil, 2012). BCIs are electronic devices that detect neural activity, either via invasive implants like microelectrodes, or using non-invasive recording techniques like functional magnetic resonance imaging (fMRI) and electroencephalograms (EEG). This measure of neural activity is then converted into digital signals which can be read into a computer. While the first BCI was developed in 1964 (Graimann et al., 2009), computer technology lacked the power to decode complex neural signals in real-time until the past two decades. Recently, there has been a large proliferation of BCI-based products (Figure 7.1), designed to assist patients with motor impairments such as paralysis, to serve as mediums to facilitate neurofeedback techniques, or just for entertainment (Chaudhary et al., 2016; Lance et al., 2012; Ray et al., 2015).

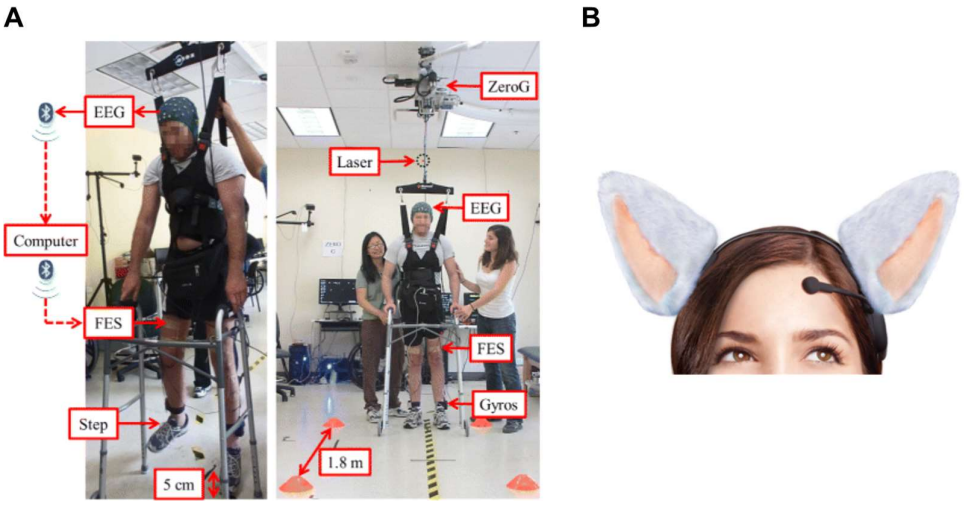

Figure 7.1: Real-world implementations of brain-computer interfaces. ***A)*** *Schematic of an electroencephalogram (EEG)-based BCI used to control a functional electrical stimulation (FES) system, designed to restore walking in paraplegic patients. Reproduced from King et al. (2015).* ***B)*** *Necomimi ears (Necomimi Store), a more frivolous application of BCI technology that converts EEG readings into the movement of cat ears attached to a headband. Image retrieved from store.necomimi.com.*

While basic research on neural coding in mice is interesting in its own right, the humanitarian and economic benefits of such research would be greatly increased if it were translated into practical applications for human use. Unfortunately, there is the common misconception among researchers that mice do not have the same aptitude to learn tasks and skills when compared to rats, let alone higher order mammals, and therefore are unsuitable as models to investigate human neural functions (Crawley, 2007; Humby and Wilkinson, 2006). This is one reason why most research on BCIs has been performed on humans and non-human primates and not rodents. While mice are undoubtedly far more limited than humans in terms of cognitive ability and manual dexterity, I believe that mice have a place in the development of BCIs. Mice are chosen as model organisms over primates in many experimental settings because they are inexpensive and genetically tractable (Humby and Wilkinson, 2006; Vandamme, 2014), and they also have relatively thin cerebral cortices which permit deep-layer calcium imaging. The same benefits apply to BCI research: the usage of mice would unlock the use of well-established mouse Cre-driver lines and deep layer calcium imaging, and a far higher throughput of experimental animals. A demonstration that population calcium activity can be used to decode motor output in mice would support the idea that the mouse is a viable model organism for research on neural decoding.

7.1.2 The linear support vector machine as a decoding algorithm

Decoding algorithms are the means by which neural population activity is decoded. Many contemporary neural decoding algorithms that are used to classify neuronal population activity function via a two-step process of machine-learning (Meyers, 2013; Vapnik, 1999). In the first step, training, the classifier is given a set of data on neuronal activity, and known experimental conditions. In the context of decoding the neural correlates of sensory input, the known conditions are stimuli, while in the context of decoding motor output, the known conditions are movements. The classifier makes assumptions on what features of neuronal activity are important, and extracts these features from the data set. It then "learns" how these features are correlated with the known conditions. For the second step, testing, the classifier is challenged with a data set of neuronal activity but with the conditions unknown, whereupon it attempts to classify the data.

To decode our calcium imaging data, we employed a linear support vector machine (LSVM). LSVMs are simple, elegant and robust methods of classifying data sets (Bennett and Campbell, 2000; Boser et al., 1992), that treat individual observations with n properties as points in n-dimensional space (Figure 7.2). In the case of decoding a neural population during the execution of a task, each neuron is considered to be a property, and each experimental trial an observation. For a task with only two categories (such as the push/pull lever task), the training stage entails the construction of a hyperplane with $n-1$ dimensions to divide the categories in n-dimensional space, while maximising separation between the categories. For the testing phase, new observations are classified based on which side of the hyperplane they lie on. The figure below graphically describes this process for a simple case of a population containing 2 neurons, i.e. $n = 2$.

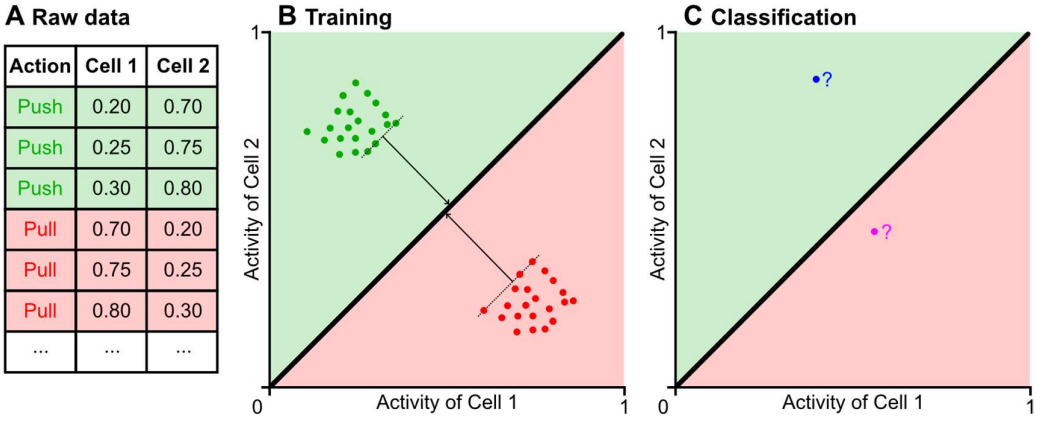

Figure 7.2: Illustration of how a linear support vector machine (LSVM) decodes neuronal population activity. ***A)*** *A hypothetical data set from a recording session with 2 neurons, classified into push trials (green) and pull trials (red). The neuronal activity of each neuron could have been measured in terms of ΔF/F, spike rate, membrane potential, etc.* ***B)*** *Each observation of population activity during a push or pull trial is represented by a point in* n*-dimensional space, where* n *is the number of neurons in the population. In this case* n *= 2. The LSVM finds a hyperplane with* n*−1 dimensions that divides the* n*-dimensional space into two volumes, while maximising the linear separation between the two classes and the hyperplane. Since there are only 2 dimensions in this case, the hyperplane is a line.* ***C)*** *The population activity during two trials of unknown classification (blue and purple points) are given to the LSVM, which classifies them based on which side of the hyperplane they lie on. In this case, the blue point is classified as a push trial, while the purple point is classified as a pull trial. For the actual data sets with dozens of neurons, the points representing single trials and the hyperplanes used to classify them exist in higher dimensional space.*

By definition, information can only be successfully decoded from neuronal population activity if it was encoded in the population activity to begin with. Therefore, the successful application of a decoding algorithm would support the idea that push/pull-specific information is encoded in $M1_{FL}$ population activity.

The data analyses described in this chapter were coded and implemented in close collaboration with Wu Yufei, a doctoral student with Dr. Aldo Faisal in the Brain & Behaviour Lab, Department of Computing, Imperial College London.

7.2 Materials and methods

7.2.1 Linear support vector machine (LSVM) implementation

The population activity used for decoding in this chapter is the same as the population activity recording via calcium imaging in Chapters 5 and 6. Posture neurons and non-task-related neurons were excluded from the analysis, and the metric of neuronal activity used for each trial was the change in mean ΔF/F from baseline to movement, as described in Section 5.2.

Each field of view (FOV) was used to train a linear support vector machine via the *fitcsvm* (train binary support vector machine classifier) function on MATLAB. Prior to training, neuronal activity (i.e. the predictor data) was standardised by scaling each neuron's ΔF/F to its mean and standard deviation, i.e.

$$\text{Standardised neuronal } \Delta F/F = \frac{\text{Neuronal } \Delta F/F - \text{Mean neuronal } \Delta F/F}{\text{Standard deviation of neuronal } \Delta F/F}$$

The accuracy of the LSVM was tested by performing *k*-fold cross-validation, with *k* = 5. This entails randomly dividing successful trials in each FOV into *k* equal-sized groups, training the LSVM on *k*−1 of the groups, and then testing the accuracy of the LSVM at predicting movement direction (i.e. push or pull) in trials within the remaining group. This is repeated *k* times, until every group has been tested as the remaining group exactly once (Figure 7.3).

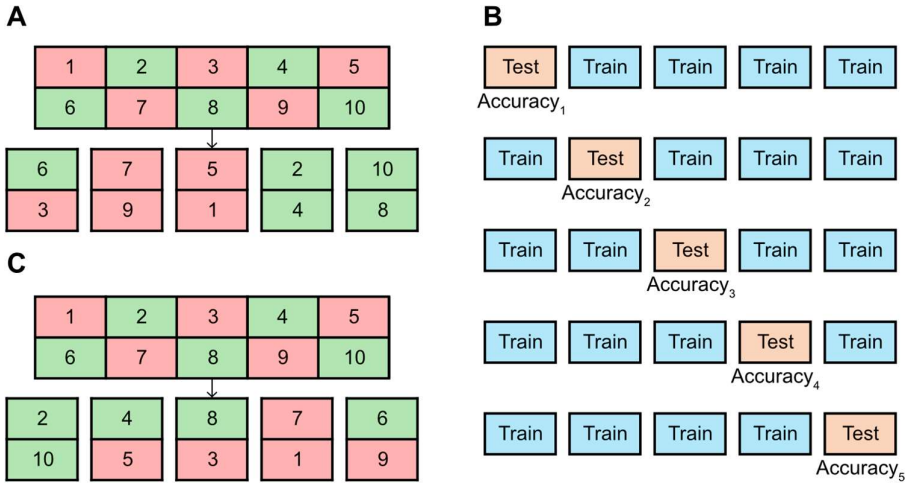

Figure 7.3: Illustration of how k*-fold cross-validation works.* ***A)*** *Assuming* k *= 5, a sample FOV with 10 successful trials (5 push trials in green, 5 pull trials in red) is randomly divided into 5 groups.* ***B)*** k*–1 groups are used to train the model, then the model is tested on the remaining group to obtain a measure of the model's accuracy.* k *measurements are made in this manner.* ***C)*** *The trials can be randomly grouped again to obtain another 5 measures of model accuracy. This can be repeated with different unique groupings.*

Since k = 5, cross-validation was performed 5 times for each random division of the population. The population was randomly divided a further 10 times for each FOV, therefore producing a total of 50 measures of LSVM accuracy for each FOV. *k*-fold cross-validation was performed using k = 5 with 10 repetitions as a balance between maximising the training data set and maximising the testing data set, thus reducing sampling bias (Rodriguez et al., 2010).

7.2.2 LSVM testing on neurons grouped by dissimilarity index

I previously hypothesised that the dissimilarity between push- and pull-related activity in neurons encodes movement direction. If this is true, then a decoding algorithm using neurons with a dissimilarity index (DI) > 1.3 or < -1.3 should decode movement direction better than a similar algorithm trained on neurons with a dissimilarity index ≈ 0. Therefore, to test this hypothesis, LSVMs were first trained and tested on the subpopulation of neurons with a DI > 1.3 or DI < -1.3 within a FOV, and then trained and tested on the remaining subpopulation of neurons with dissimilarity indices ≈ 0. Only FOVs which contained at least 10 neurons in each category were included in this analysis. When grouping FOVs by DI, if there were at least twice as many neurons with DI > 1.3 than DI < -1.5, or vice-versa, it was considered to have more neurons with that DI. If neither was true, the FOV was considered to be mixed between the DI > 1.3 and DI < -1.5 categories.

7.3 Results

7.3.1 Decoding accuracy

To determine if movement direction (i.e. push or pull) could be successfully decoded from two-photon population activity, task-related neurons from each FOV recorded (from both layer 2/3 and layer 5B) were used to train an LSVM, which was then *k*-fold cross-validated for *k* = 5, with 50 repeats. (Figure 7.4). These FOVs are the same as those described in Chapters 5 and 6. A total of N = 19 FOVs from L2/3 and a total of N = 15 FOVs from L5B were included in the analysis.

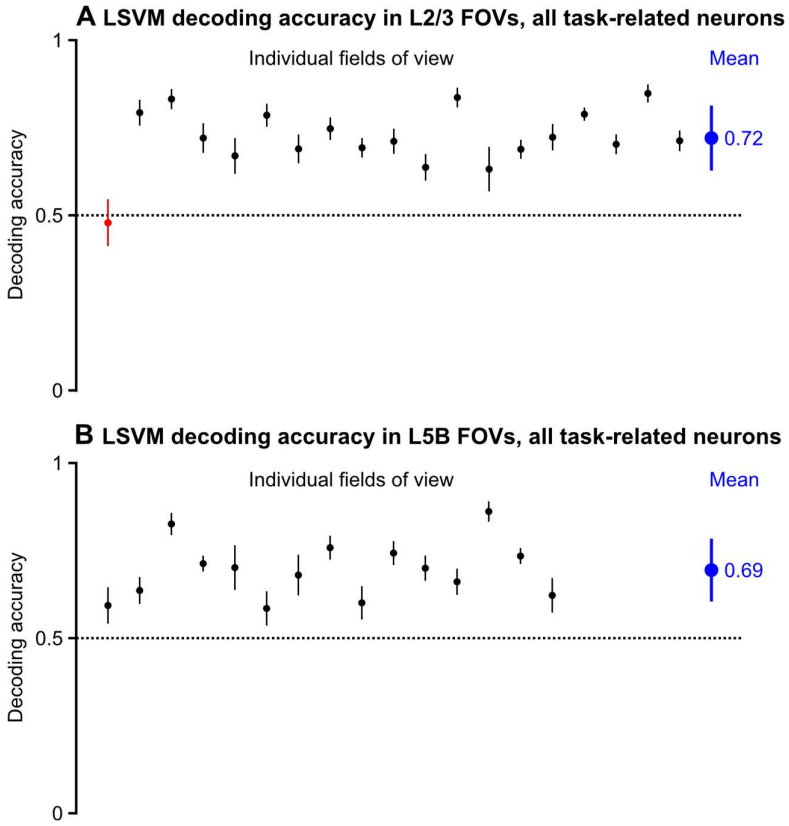

Figure 7.4: Accuracy of decoding movement direction using neuronal population activity. ***A)*** *Accuracy of LSVMs trained on L2/3 FOVs. Each black circle represents the mean decoding accuracy ± SD of an LSVM trained on each individual FOV. FOVs were sorted by increasing number of task-related neurons from left to right. The large blue circle represents the mean decoding accuracy ± SD across all L2/3 FOVs. The horizontal dotted line indicates an accuracy*

of 0.5, which represents the chance level of decoding. ***B)*** *Accuracy of LSVMs while decoding recordings of L5B neurons, presented in the same manner as A.*

In all but one FOVs in L2/3 and all FOVs in L5B, the LSVM decoded movement type significantly better than chance level (one-tailed *t*-test, d.f. = 49, $p < 0.001$) (see red symbol depicting one FOV where decoding accuracy was not significantly different to chance level). The observation that the LSVM trained on the single L2/3 FOV with the fewest number of neurons failed to decode movement direction better than chance level suggested it was necessary to test whether neuron count was an important determinant of decoding accuracy. I found that the number of neurons per FOV included in the analysis did not significantly correlate with decoding accuracy in either layer (d.f. = 36, $p = 0.63$ for L2/3 and d.f. = 28 , $p = 0.46$ for L5B, Spearman's rank correlation test).

7.3.2 Decoding accuracy in neurons grouped by dissimilarity index

To test whether neurons with significant dissimilarity index (DI) were better predictors of movement direction than neurons with dissimilarity index ≈ 0, LSVMs were separately trained and tested on each of the two subpopulations (Figure 7.5). FOVs with at least 10 neurons with DI > 1.3, DI < -1.3 and at least 10 neurons with DI ≈ 0, were included in the analysis. In total, there were N = 7 FOVs recorded in layer 2/3, and N = 4 FOVs in layer 5B.

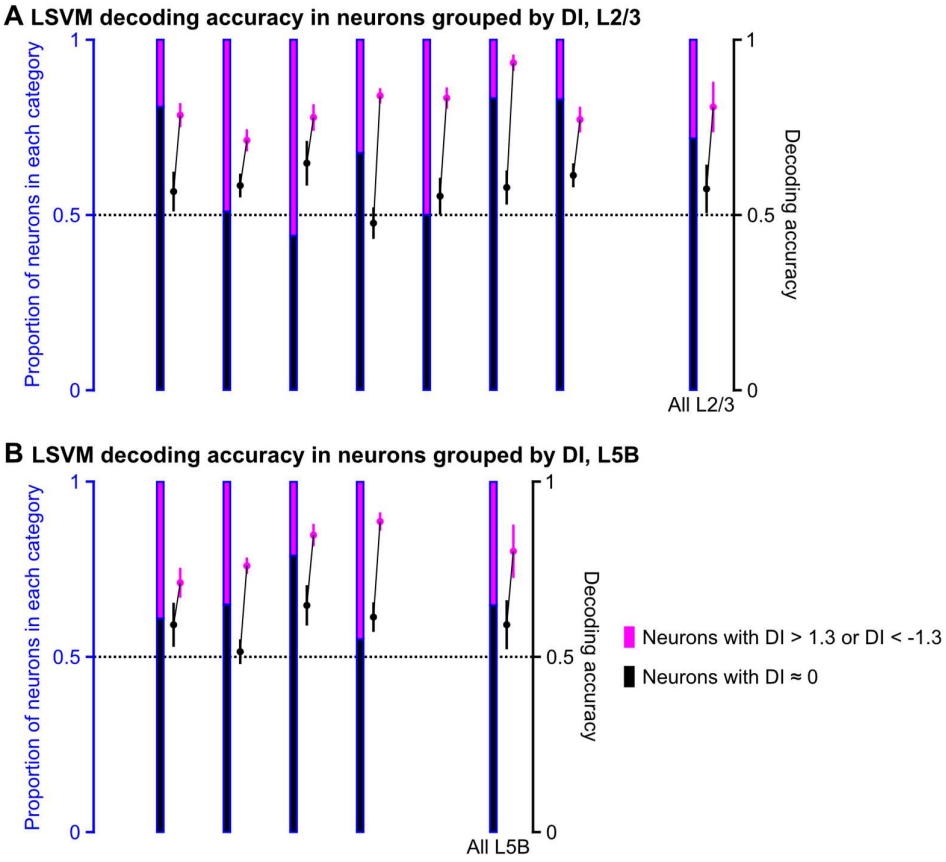

Figure 7.5: LSVM decoding accuracy in neurons grouped by DI. ***A)*** *Accuracy of LSVM models while decoding L2/3 neuron activity. For each FOV, the stacked bar graph highlighted in blue indicates the proportions of neurons with DI < -1.3 and DI > 1.3 combined (magenta) and neurons with DI ≈ 0 (black). Each circle is colour-coded in a similar manner, and depicts the mean accuracy ± SD of an LSVM trained only with neurons from that category. The rightmost group displays the overall mean statistics for all L2/3 FOVs combined. The horizontal dotted line indicates an accuracy of 0.5, which represents the chance level of decoding.* ***B)*** *Accuracy of LSVM models while decoding L5B neurons, presented in the same manner as A.*

In every FOV in both L2/3 and L5B, the LSVM trained only on neurons with DI < -1.3 or DI > 1.3, decoded movement type with a higher accuracy than the LSVM trained on neurons with DI ≈ 0 (two-tailed two-sample *t*-test, $p < 0.001$), despite the DI ≈ 0 neuronal population being larger in all but two FOVs. Next, FOVs were grouped by the direction of DI, i.e. whether there were more neurons with DI < -1.3 or DI > 1.3, to investigate whether neurons in one particular group predicted movement direction with higher accuracy (Figure 7.6).

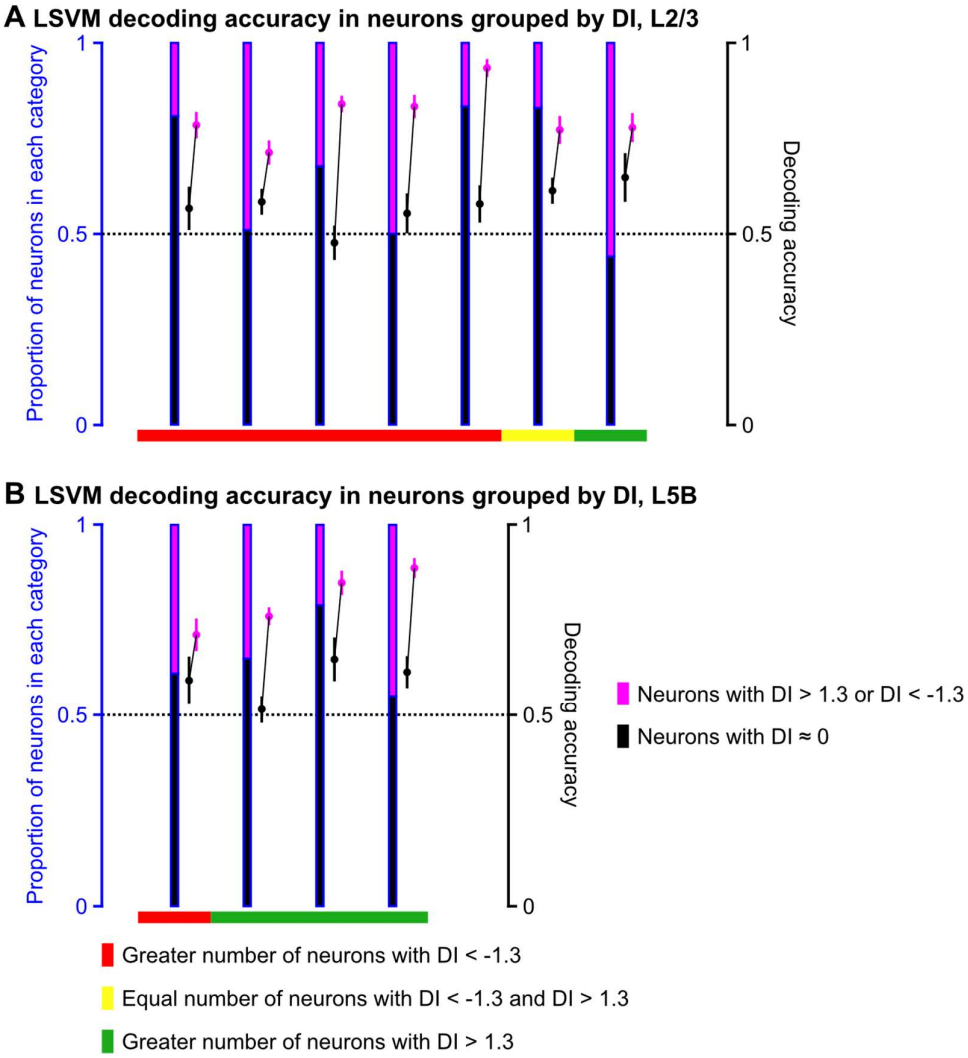

Figure 7.6: LSVM decoding accuracy in neurons, with FOVs sorted by DI. ***A)*** *Accuracy of LSVM models while decoding L2/3 neuron activity. For each FOV, the stacked bar graph highlighted in blue indicates the proportions of neurons with DI < -1.3 and DI > 1.3 combined (magenta) and neurons with DI ≈ 0 (black). Each circle is colour-coded in a similar manner and depicts the mean accuracy ± SD of an LSVM trained only with neurons from that category. The horizontal dotted line indicates an accuracy of 0.5, which represents the chance level of decoding. The horizontal coloured bar below each vertical bar depicts the distribution of DI for neurons in that FOV.* ***B)*** *Accuracy of LSVM models while decoding L5B neurons, presented in the same manner as A.*

Unfortunately there were insufficient FOVs to statistically compare whether FOV with more DI > 1.3 neurons or DI < -1.3 neurons could be decoded by LSVMs more effectively, there does not appear to be any trend of movement direction being more effectively decoded from DI > 1.3 neurons or DI < -1.3 neurons. Focusing on L2/3, LSVMs appear to decode movement

direction equally well when trained on neurons with DIs significantly different from zero, whether the DIs were positive or negative. Therefore, decoding of movement type was more accurate when LSVMs were trained using neurons which displayed significant differences between push- and pull-related ΔF/F changes, regardless of whether the push-related change or pull-related change was larger.

7.4 Discussion

7.4.1 The accuracy of decoding neuronal population activity

The mean decoding accuracy in both L2/3 and L5B FOVs was ~0.7, with almost every FOV being decoded at higher than chance level. This is remarkable, considering that several channels of task-related information were lost during the course of calcium imaging and data analysis. Neural populations encode information in several modalities, including the identity of the active neurons, their firing frequencies, spike timings, and timing correlations between neurons (Borst and Theunissen, 1999; Panzeri et al., 2015). Like all contemporary techniques of neural recording, calcium imaging is unable to fully capture all this information. Calcium imaging records neuronal activity from a population that lies in a single plane, in a limited FOV. The neurons present in that FOV constitute a small fraction of the whole neuronal population of $M1_{FL}$ and only a fraction of neurons in each L2/3 (52%) and L5B (86%) FOV display measurable changes in ΔF/F. These measurements do not contain information regarding the exact spike times or changes in timing correlations (Chen et al., 2013b). Finally, the LSVM decoding algorithm assumes that push and pull trials are independent and their associated ΔF/F values arranged in linearly separable clusters, assumptions which may not be true (Bennett and Campbell, 2000).

Despite all these sources of information loss, the LSVM models were capable of decoding neuronal activity to a high degree of precision. While the accuracy was far from perfect, the results represent a novel implementation of machine learning to decode directional motor output from two-photon population imaging datasets. Machine learning techniques have been successfully used to decode directional motor output from electrocorticographic recordings and functional magnetic resonance imaging (Bundy et al., 2016; Nam and Kim, 2017), and to decode the amplitude of whisking and frequency of licking from population calcium imaging in L2/3 of M1 (Huber et al., 2012), but to date there are no published studies that have successfully decoded movement direction from population imaging. In addition, the findings described here vindicate the theory that direction-specific information on forelimb motor output is encoded in $M1_{FL}$ both in L2/3 and L5B.

7.4.2 How many neurons does it take to decode movement from population activity?

Ultimately, a major goal of contemporary neuroscience is to "crack the neural code", that is, to successfully decode patterns of neuronal activity *in vivo*. But as mentioned in Chapter 1, decoding activity in a neuronal population can either refer to how downstream neurons interpret that activity, or how external observers can correlate that activity with known sensory stimuli or motor outputs (Borst and Theunissen, 1999; Knierim, 2014). Since neurons in the mammalian brain form densely interconnected circuits with multiple recurrent loops, cracking the neural code requires recording activity patterns from large populations of neurons rather than single units (Hopfield, 1995). Indeed, many developments in population calcium imaging and electrophysiology have been made to increase the number of neurons recoded during experiments (Kapoor et al., 2013; Kwan, 2008; Steinmetz et al., 2018). However, here I will propose a contrarian perspective, that perhaps less can be more.

Information theory predicts that neurons with lower spike rates provide information at a lower rate than neurons with higher spike rates, and non-firing neurons provide no information at all (Borst and Theunissen, 1999). It has long been known that the number of neurons identified during electrophysiological recordings is far lower than the expected neuron count, by a factor of 10 or more (Henze et al., 2000; Robinson, 1968; Shoham et al., 2006). Many of the neurons which are not identified are silent, or have low firing rates which render them difficult to identify using electrophysiological techniques (Shoham et al., 2006). In mouse M1, even neurons successfully identified during electrophysiological recordings often have low firing rates, under 5 Hz for L5B (Estebanez et al., 2017; Schiemann et al., 2015), and below 1 Hz in L2/3 Hz (Petersen and Crochet, 2013; Poulet and Petersen, 2008). Considering that for a given population, downstream neurons only receive information through action potentials, such non-firing or slow-firing neurons provide less synaptic input than highly active neurons to downstream circuits. Therefore, the sampling bias described in Chapter 4, where less active neurons are less frequently identified in FOVs, may paradoxically enhance our measurement of population activity by focusing on the highly active neurons which feed more information to downstream motor circuits.

The results described in Section 7.3.2 suggest that LSVMs trained using only neurons with DI > 1.3 or DI < -1.3 were able to predict movement type to a high degree of accuracy, while LSVMs trained on neurons with DI ≈ 0 were significantly less accurate. This observation

implies that training a machine learning algorithm with activity patterns of all recorded neurons does not necessarily lead to behaviour being decoded with the highest accuracy. In fact, decoding may be more accurate when training algorithms with activity patterns from only a subset of neurons. After all, coding in the mammalian cortex is relatively sparse in terms of how many neurons become active during a given condition, whether sensory or motor (Graham and Field, 2007; Spanne and Jörntell, 2015; Tolhurst et al., 2009). Focusing on neurons which demonstrate the greatest changes in activity during that condition, be it sensory input or motor output, may make it easier to decode the condition from activity by excluding neurons that were not encoding much condition-specific information.

In addition, the decoding of population activity described in this chapter was performed using the reliable but relatively simple technique of LSVM training. However, rapid advances in computer science during the last decade have produced far more powerful methods of machine learning, such as cluster analysis and deep learning, which are ripe for application in the field of neuroscience (LeCun et al., 2015; Marblestone et al., 2016). I believe that future studies using interdisciplinary approaches that combine neurophysiology with computer science will bring the field significantly closer to understanding the coding of activity in neuronal populations.

7.4.3 Future directions

The successful decoding of directional movements from population calcium imaging present an opportunity for more avenues of enquiry into directional coding in M1. Firstly, are there better algorithms which can be used to decode population imaging data? LSVMs are reliable and frequently used in machine learning, but there are also more sophisticated techniques which may perform better. These include non-linear support vector machines which do not assume that categories are linearly separable (Murty et al., 2006), or completely different decoding algorithms such as nearest-neighbour decoders and artificial neural networks (Quian Quiroga and Panzeri, 2009). Decoding algorithms have not been exhaustively applied to calcium imaging datasets, and there is currently no consensus on the optimal method for effectively decoding such data.

Secondly, could we decode more features of motor output from population imaging in $M1_{FL}$? During the execution of our push-pull task, there are other features of movement such as non-task-related forelimb movements (quantified in terms of motion index in Chapter 4), which are likely to be encoded in $M1_{FL}$ population activity. High-speed cameras and motion tracking software could be employed to monitor forelimb position during such movements, and then decoding algorithms used to determine how they were reflected in $M1_{FL}$ population activity. Additionally, this project describes a bidirectional push/pull lever task, but future studies could instead record population activity during the execution of a multidirectional lever task or reaching task. This would address questions related to the somatotopy of $M1_{FL}$: if $M1_{FL}$ contains a predominantly push-related region and a predominantly pull-related region as suggested by some studies (Harrison et al., 2012; Wang et al., 2017), how are forelimb movements in orthogonal directions (e.g. leftwards) represented on the cortical surface?

Finally, specific $M1_{FL}$ neuronal subpopulations could be recorded to observe how they encoded forelimb movement. How well would a decoder perform if it was trained only with the activity of L5B PT-type neurons, which can be selectively labelled *in vivo* by retrograde tracing from the brainstem (Li et al., 2015)? Or with only inhibitory interneurons, expressing GCaMP6s driven by a vesicular GABA transporter (VGAT) promoter (Chaudhry et al., 1998)? Neuronal populations at different anatomical coordinates could also be investigated, for example in different layers of $M1_{FL}$, or in different regions of the cortex, to determine how information regarding motor output is encoded in different layers and regions of the cortex.

This page was intentionally left blank.

General discussion

This thesis has focused on understanding how neuronal populations encode different movements actions in mouse $M1_{FL}$., using two-photon imaging in L2/3 and L5B during the execution of a push/pull cued lever task. We also sought to verify the reliability of the techniques used in the process, through examining the behavioural metrics of the cued lever task, the cytoarchitecture of $M1_{FL}$, and the potential confounds caused by non-task-related movement during calcium imaging. The study of population coding is of interest to the neuroscientific community in general, and myself in particular, as skilled motor output is an important method by which many mammals, including us humans, interact with the world (Sherrington, 1949). M1 is a key node in the motor system, hence elucidating neural coding in M1 is essential to understanding how the nervous system generates dextrous movements (Graziano, 2006; Hatsopoulos and Suminski, 2011).

L5B is the upper boundary of L5B in multiple mice, we were able to ensure that population imaging experiments targeted to L5B were recorded at appropriate depths from the pia. In contrast, experiments that target calcium imaging to specific layers using pial depths alone run the risk of performing calcium imaging in an adjacent layer instead, and therefore interpreting layer-specific data derived from the wrong layer, for example by including L5B-specific PT-projecting neurons in a study on L5A activity (Masamizu et al., 2014). It is my opinion that in general, studies of specific cortical layers should include similar experiments in order to clearly define layer boundaries, as these can drastically change in different cortical regions and different animal ages, even within the same species.

We also described the design and implementation of a cued push/pull task, and how we trained mice to repeatedly and reliably perform cued push and pull movements through a series of behavioural shaping stages (Chapter 3). Given our success at training mice to perform two diametrically opposed movements, we plan to extend this range of motion to a cued joystick-based task with 4 or more movement directions. Developing such a task would enable us to study directional coding in mice to a higher level of resolution, and to examine if individual neurons exhibit graded tuning curves to different directional movements, those observed in M1 neurons of non-human primates (Georgopoulos et al., 1982). It would also

allow us to map the distribution of direction preference in cortical neurons, and determine whether preferred directions are somatotopically mapped onto different cortical regions, or arranged in columns as Georgopoulos predicted, or organised in another fashion.

We also examined the potential pitfalls related to calcium imaging in experimental animals (Chapter 4). These potential pitfalls apply to neural recordings in other species as well. For example, the "dark matter problem" of recording techniques observing fewer neurons than the number of neurons physically present in a given neuronal subpopulation, exists across multiple species and neural recording techniques (Shoham et al., 2006). This problem potentially introduces sampling bias and confounds the interpretation of experimental results. By using independent histological techniques to measure layer-specific neuronal density in $M1_{FL}$, we present a novel method of estimating the number of silent "dark neurons" in two-photon fields of view. Computational models of population activity may also benefit by integrating such quantitative measurements of the number of "dark neurons" in neuronal populations.

In addition, we used a motion index to quantify the amount of non-task-related movement mice produced during task execution. This can be expanded further with the addition of high frames-per-second infrared cameras filming from multiple angles and motion tracking software, which will allow us to track features such as individual limb positions and joint angles. Population imaging data could be then correlated with these features to determine the extent to which they are encoded in cortical activity, thus furthering our understanding of cortical population coding.

The population imaging data from L5B (Chapter 5) and L2/3 (Chapter 6) generated new insights into $M1_{FL}$ population dynamics during the execution of a bidirectional forelimb task. We found that L2/3 neurons encoded task-related and directions-specific activity in a more sparse manner than L5B neurons, which matches the findings of several published studies, and suggests that motor coding may be more sparse as one goes further upstream from motor output (Galiñanes et al., 2018; Huber et al., 2012; Li et al., 2015, 2017). Our findings indicate that direction-specific population activity does not originate in L5B of $M1_{FL}$, as L2/3 of $M1_{FL}$ (which projects to L5B) also exhibits direction-specific population activity. Where then does direction-specific population activity first start to emerge in the brain? One potential candidate is the prefrontal cortex, which is involved in decision-making and action selection, and indirectly provides feedforward input to M1 via M2 (Gremel and Costa, 2013;

Ward et al., 2015; Zimmermann et al., 2017). Another is the motor thalamus, which projects to both M1 and M2, and is necessary for the production of skilled motor output (Dacre, 2016; Watson et al., 2012; Yamawaki et al., 2014). Recording neuronal populations in these regions may help us better understand how the motor system generates directional movement.

One interesting observation that we still cannot fully explain is why different fields of view in both L2/3 and L5B contained neurons with different distributions of dissimilarity indices. The most parsimonious explanation is that $M1_{FL}$ is somatotopically organised into regions which preferentially encode specific movement directions, with some degree of individual variation between mice (Harrison et al., 2012; Wang et al., 2017). To test this hypothesis, the next step would be to perform wide-field population imaging in a larger area of $M1_{FL}$. If $M1_{FL}$ is indeed organised into macro-scale regions, the boundaries of such regions would be separately observable in ~800 μm wide FOVs.

We also successfully decoded movement direction from population activity generated in both L2/3 and L5B (Chapter 7). Our ability to decode information on movement direction suggests that 'directional' information is encoded at the level of $M1_{FL}$ neuronal populations, and that the mouse is a valid model organism for studying how skilled motor output is encoded in the mammalian brain. However, the decoding method we used, the LSVM, is far from the only technique available. Support vector machines can be extended with non-linear kernels. We can further extend our analysis by implementing other decoding methods such as linear discriminant analysis or deep neural networks. Additionally, we can adjust the parameters used to train our models, such as the number of neurons included in each sample and the timing of windows used to quantify neural activity, to gain further insights into cortical coding. For example, what is the earliest time point before a movement at which we can successfully decode its direction? What is the minimum number of neurons in a population required to accuracy model population activity?

We have described a robust and reliable behavioural paradigm for producing directional forelimb movements, empirical confirmations of the validity of population imaging in deep-layer cortex, a rich dataset of population activity recorded from L2/3 and L5B of neuronal populations in $M1_{FL}$, and evidence that machine-learning algorithms are capable of decoding movement direction from such population activity. Together, these constitute a platform from which we can advance our understanding of directional coding in neuronal populations during the production of skilled motor output.

Appendix A.1

To determine if pre-action motion index had an effect on neuronal dissimilarity index (DI), the N = 11 L5B fields of view with motion index (MI) were separated by their pre-action motion index, and their distributions of neuronal DIs plotted. A two-tailed two-sample *t*-test was used to determine if each field of view had a higher pre-push MI, higher pre-pull MI, or statistically similar pre-action MIs, as described in Section 4.3.2.

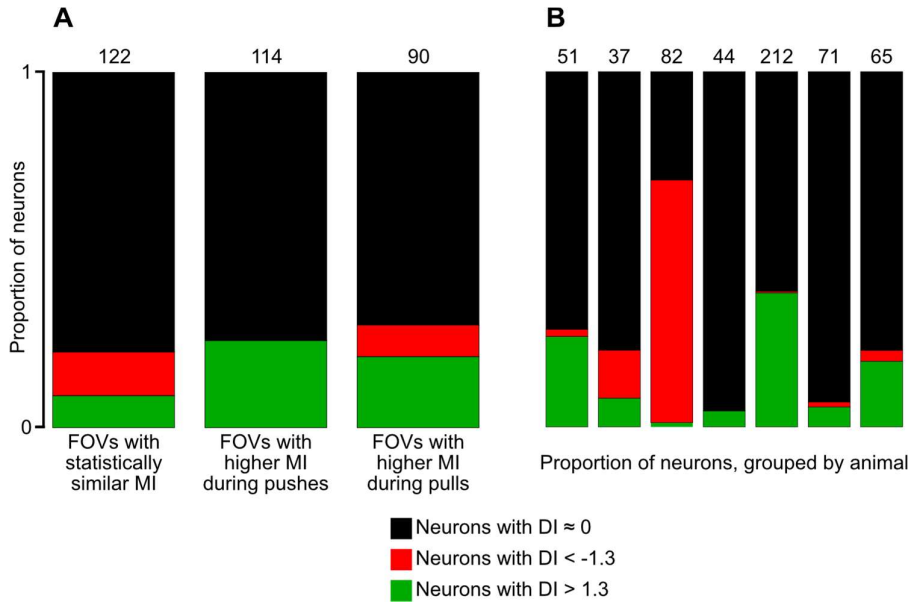

Proportions of task-related cells in L5B FOVs, classified by DI. ***A)*** *Proportions of cells from recording sessions with known motion index (MI), grouped by pre-movement MI. The numbers above each bar indicate the number of cells in that category. The distribution of cell categories was not independent from session MI (d.f. = 4, χ^2 = 22.2, p < 0.001). However, there was no clear trend between session MI and neuron DI.* ***B)*** *Proportions of cells from all recording sessions, grouped by animal. Each bar represents a single mouse. The distribution of cell categories was highly variable between mice, and not independent (d.f. = 12, χ^2 = 360, p < 0.001).*

The graphs above suggest that there is no clear trend linking MI with DI, while the distribution of neuronal DIs was highly variable across mice suggesting pre-movement MI is not the primary determinant of neuronal DI.

Bibliography

Akaike, H. (1974). A new look at the statistical model identification. IEEE Trans. Autom. Control *19*, 716–723.

Al-Juboori, S.I., Dondzillo, A., Stubblefield, E.A., Felsen, G., Lei, T.C., and Klug, A. (2013). Light Scattering Properties Vary across Different Regions of the Adult Mouse Brain. PLoS ONE *8*.

Amirikian, B., and Georgopoulos, A.P. (2003). Modular organization of directionally tuned cells in the motor cortex: Is there a short-range order? Proc. Natl. Acad. Sci. *100*, 12474–12479.

Andermann, M.L., Kerlin, A.M., and Reid, C. (2010). Chronic cellular imaging of mouse visual cortex during operant behavior and passive viewing. Front. Cell. Neurosci. *4*.

Anderson, C.T., Sheets, P.L., Kiritani, T., and Shepherd, G.M.G. (2010). Sublayer-specific microcircuits of corticospinal and corticostriatal neurons in motor cortex. Nat. Neurosci. *13*, 739–744.

Apicella, A.J., Wickersham, I.R., Seung, H.S., and Shepherd, G.M.G. (2012). Laminarly Orthogonal Excitation of Fast-Spiking and Low-Threshold-Spiking Interneurons in Mouse Motor Cortex. J. Neurosci. *32*, 7021–7033.

Averbeck, B.B., Latham, P.E., and Pouget, A. (2006). Neural correlations, population coding and computation. Nat. Rev. Neurosci. *7*, 358–366.

Babadi, B., and Sompolinsky, H. (2014). Sparseness and Expansion in Sensory Representations. Neuron *83*, 1213–1226.

Balleine, B.W., and O'Doherty, J.P. (2010). Human and Rodent Homologies in Action Control: Corticostriatal Determinants of Goal-Directed and Habitual Action. Neuropsychopharmacology *35*, 48–69.

Beloozerova, I.N., and Sirota, M.G. (1988). Role of Motor Cortex in Control of Locomotion. In Stance and Motion, (Springer, Boston, MA), pp. 163–176.

Bennett, K.P., and Campbell, C. (2000). Support Vector Machines: Hype or Hallelujah? SIGKDD Explor Newsl *2*, 1–13.

Benucci, A., Ringach, D.L., and Carandini, M. (2009). Coding of stimulus sequences by population responses in visual cortex. Nat. Neurosci. *12*, 1317–1324.

Berens, P., Ecker, A.S., Cotton, R.J., Ma, W.J., Bethge, M., and Tolias, A.S. (2012). A Fast and Simple Population Code for Orientation in Primate V1. J. Neurosci. *32*, 10618–10626.

Bernshteĭn, N.A. (1967). The co-ordination and regulation of movements (Oxford; New York: Pergamon Press).

Beul, S.F., and Hilgetag, C.C. (2015). Towards a “canonical” agranular cortical microcircuit. Front. Neuroanat. *8*.

Borst, A., and Theunissen, F.E. (1999). Information theory and neural coding. Nat. Neurosci. *2*, 947–957.

Boser, B.E., Guyon, I.M., and Vapnik, V.N. (1992). A Training Algorithm for Optimal Margin Classifiers. In Proceedings of the Fifth Annual Workshop on Computational Learning Theory, (New York, NY, USA: ACM), pp. 144–152.

Braak, H., Ludolph, A.C., Neumann, M., Ravits, J., and Del Tredici, K. (2017). Pathological TDP-43 changes in Betz cells differ from those in bulbar and spinal α-motoneurons in sporadic amyotrophic lateral sclerosis. Acta Neuropathol. (Berl.) *133*, 79–90.

Brecht, M., and Sakmann, B. (2002). Dynamic representation of whisker deflection by synaptic potentials in spiny stellate and pyramidal cells in the barrels and septa of layer 4 rat somatosensory cortex. J. Physiol. *543*, 49–70.

Brodmann, K. (2006). Brodmann’s: Localisation in the Cerebral Cortex (Springer US).

Brooks, S.P., and Dunnett, S.B. (2009). Tests to assess motor phenotype in mice: a user’s guide. Nat. Rev. Neurosci. *10*, 519–529.

Bundy, D.T., Pahwa, M., Szrama, N., and Leuthardt, E.C. (2016). Decoding three-dimensional reaching movements using electrocorticographic signals in humans. J. Neural Eng. *13*, 026021.

Caminiti, R., Johnson, P.B., and Urbano, A. (1990). Making arm movements within different parts of space: dynamic aspects in the primate motor cortex. J. Neurosci. *10*, 2039–2058.

Cannell, M.B., Berlin, J.R., and Lederer, W.J. (1987). Intracellular calcium in cardiac myocytes: calcium transients measured using fluorescence imaging. Soc. Gen. Physiol. Ser. *42*, 201–214.

Castro, A.J. (1972). The effects of cortical ablations on digital usage in the rat. Brain Res. *37*, 173–185.

Chaudhary, U., Birbaumer, N., and Ramos-Murguialday, A. (2016). Brain–computer interfaces for communication and rehabilitation. Nat. Rev. Neurol. *12*, 513–525.

Chaudhry, F.A., Reimer, R.J., Bellocchio, E.E., Danbolt, N.C., Osen, K.K., Edwards, R.H., and Storm-Mathisen, J. (1998). The Vesicular GABA Transporter, VGAT, Localizes to Synaptic Vesicles in Sets of Glycinergic as Well as GABAergic Neurons. J. Neurosci. *18*, 9733–9750.

Chen, C.-C., Gilmore, A., and Zuo, Y. (2014). Study Motor Skill Learning by Single-pellet Reaching Tasks in Mice. J. Vis. Exp. JoVE.

Chen, J.L., Andermann, M.L., Keck, T., Xu, N.-L., and Ziv, Y. (2013a). Imaging Neuronal Populations in Behaving Rodents: Paradigms for Studying Neural Circuits Underlying Behavior in the Mammalian Cortex. J. Neurosci. *33*, 17631–17640.

Chen, T.-W., Wardill, T.J., Sun, Y., Pulver, S.R., Renninger, S.L., Baohan, A., Schreiter, E.R., Kerr, R.A., Orger, M.B., Jayaraman, V., et al. (2013b). Ultrasensitive fluorescent proteins for imaging neuronal activity. Nature *499*, 295–300.

Chen, T.-W., Li, N., Daie, K., and Svoboda, K. (2017). A Map of Anticipatory Activity in Mouse Motor Cortex. Neuron *94*, 866-879.e4.

Chen, X., Leischner, U., Varga, Z., Jia, H., Deca, D., Rochefort, N.L., and Konnerth, A. (2012). LOTOS-based two-photon calcium imaging of dendritic spines in vivo. Nat. Protoc. *7*, 1818–1829.

Churchland, M.M., Afshar, A., and Shenoy, K.V. (2006). A central source of movement variability. Neuron *52*, 1085–1096.

Classen, J., Liepert, J., Wise, S.P., Hallett, M., and Cohen, L.G. (1998). Rapid Plasticity of Human Cortical Movement Representation Induced by Practice. J. Neurophysiol. *79*, 1117–1123.

Collinger, J.L., Wodlinger, B., Downey, J.E., Wang, W., Tyler-Kabara, E.C., Weber, D.J., McMorland, A.J., Velliste, M., Boninger, M.L., and Schwartz, A.B. (2013). High-performance neuroprosthetic control by an individual with tetraplegia. The Lancet *381*, 557–564.

Courtine, G., Bunge, M.B., Fawcett, J.W., Grossman, R.G., Kaas, J.H., Lemon, R., Maier, I., Martin, J., Nudo, R.J., Ramon-Cueto, A., et al. (2007). Can experiments in nonhuman primates expedite the translation of treatments for spinal cord injury in humans? Nat. Med. *13*, 561–566.

Crawley, J.N. (2007). What's Wrong With My Mouse?: Behavioral Phenotyping of Transgenic and Knockout Mice (John Wiley & Sons).

Crawley, J.N., and Paylor, R. (1997). A Proposed Test Battery and Constellations of Specific Behavioral Paradigms to Investigate the Behavioral Phenotypes of Transgenic and Knockout Mice. Horm. Behav. *31*, 197–211.

Cuccia, D.J., Abookasis, D., Frostig, R.D., and Tromberg, B.J. (2009). Quantitative In Vivo Imaging of Tissue Absorption, Scattering, and Hemoglobin Concentration in Rat Cortex Using Spatially Modulated Structured Light. In In Vivo Optical Imaging of Brain Function, R.D. Frostig, ed. (Boca Raton (FL): CRC Press/Taylor & Francis), p.

Dacre, J. (2016). Thalamic control of motor behaviour. Doctoral thesis. University of Edinburgh.

Darling, W.G., Pizzimenti, M.A., and Morecraft, R.J. (2011). Functional recovery following motor cortex lesions in non-human primates: experimental implications for human stroke patients. J. Integr. Neurosci. *10*, 353–384.

Deacon, R.M.J. (2009). Digging in Mice: Marble Burying, Burrowing, and Direct Observation Reveal Changes in Mouse Behavior. In Mood and Anxiety Related Phenotypes in Mice, (Humana Press, Totowa, NJ), pp. 37–45.

Denk, W., and Svoboda, K. (1997). Photon Upmanship: Why Multiphoton Imaging Is More than a Gimmick. Neuron *18*, 351–357.

Denk, W., Strickler, J.H., and Webb, W.W. (1990). Two-photon laser scanning fluorescence microscopy. Science *248*, 73–76.

Denk, W., Delaney, K.R., Gelperin, A., Kleinfeld, D., Strowbridge, B.W., Tank, D.W., and Yuste, R. (1994). Anatomical and functional imaging of neurons using 2-photon laser scanning microscopy. J. Neurosci. Methods *54*, 151–162.

Dombeck, D.A., Khabbaz, A.N., Collman, F., Adelman, T.L., and Tank, D.W. (2007). Imaging Large-Scale Neural Activity with Cellular Resolution in Awake, Mobile Mice. Neuron *56*, 43–57.

Douglas, R.J., and Martin, K.A.C. (2007). Recurrent neuronal circuits in the neocortex. Curr. Biol. *17*, R496–R500.

Douglas, R.J., Martin, K.A.C., and Whitteridge, D. (1989). A Canonical Microcircuit for Neocortex. Neural Comput. *1*, 480–488.

Dow, B.M. (2002). Orientation and Color Columns in Monkey Visual Cortex. Cereb. Cortex *12*, 1005–1015.

Doyle, A., McGarry, M.P., Lee, N.A., and Lee, J.J. (2012). The Construction of Transgenic and Gene Knockout/Knockin Mouse Models of Human Disease. Transgenic Res. *21*, 327–349.

Dräger, U.C. (1975). Receptive fields of single cells and topography in mouse visual cortex. J. Comp. Neurol. *160*, 269–290.

Eisenberg, M., Shmuelof, L., Vaadia, E., and Zohary, E. (2010). Functional Organization of Human Motor Cortex: Directional Selectivity for Movement. J. Neurosci. *30*, 8897–8905.

Ellenbroek, B., and Youn, J. (2016). Rodent models in neuroscience research: is it a rat race? Dis. Model. Mech. *9*, 1079–1087.

Espuny-Camacho, I., Michelsen, K.A., Gall, D., Linaro, D., Hasche, A., Bonnefont, J., Bali, C., Orduz, D., Bilheu, A., Herpoel, A., et al. (2013). Pyramidal neurons derived from human pluripotent stem cells integrate efficiently into mouse brain circuits in vivo. Neuron *77*, 440–456.

Estebanez, L., Hoffmann, D., Voigt, B.C., and Poulet, J.F.A. (2017). Parvalbumin-Expressing GABAergic Neurons in Primary Motor Cortex Signal Reaching. Cell Rep. *20*, 308–318.

Evarts, E.V. (1974). Precentral and postcentral cortical activity in association with visually triggered movement. J. Neurophysiol. *37*, 373–381.

Fabbri, S., Caramazza, A., and Lingnau, A. (2010). Tuning Curves for Movement Direction in the Human Visuomotor System. J. Neurosci. *30*, 13488–13498.

Faisal, A.A., Selen, L.P.J., and Wolpert, D.M. (2008). Noise in the nervous system. Nat. Rev. Neurosci. *9*, 292–303.

Farr, T.D., and Whishaw, I.Q. (2002). Quantitative and Qualitative Impairments in Skilled Reaching in the Mouse (Mus musculus) After a Focal Motor Cortex Stroke. Stroke *33*, 1869–1875.

Fertig, D.S., and Edmonds, V.W. (1969). The Physiology of the House Mouse. Sci. Am. *221*, 103–113.

Frank, L.M., Brown, E.N., and Wilson, M. (2000). Trajectory Encoding in the Hippocampus and Entorhinal Cortex. Neuron *27*, 169–178.

Fritsch, G., and Hitzig, E. (2009). Electric excitability of the cerebrum (Über die elektrische Erregbarkeit des Grosshirns). Epilepsy Behav. *15*, 123–130.

Fu, Q.G., Flament, D., Coltz, J.D., and Ebner, T.J. (1995). Temporal encoding of movement kinematics in the discharge of primate primary motor and premotor neurons. J. Neurophysiol. *73*, 836–854.

Galiñanes, G.L., Bonardi, C., and Huber, D. (2018). Directional Reaching for Water as a Cortex-Dependent Behavioral Framework for Mice. Cell Rep. *22*, 2767–2783.

Gandolfo, F., Li, C.-S.R., Benda, B.J., Schioppa, C.P., and Bizzi, E. (2000). Cortical correlates of learning in monkeys adapting to a new dynamical environment. Proc. Natl. Acad. Sci. *97*, 2259–2263.

Georgopoulos, A.P., and Carpenter, A.F. (2015). Coding of movements in the motor cortex. Curr. Opin. Neurobiol. *33*, 34–39.

Georgopoulos, A.P., Kalaska, J.F., Caminiti, R., and Massey, J.T. (1982). On the relations between the direction of two-dimensional arm movements and cell discharge in primate motor cortex. J. Neurosci. *2*, 1527–1537.

Georgopoulos, A.P., Kettner, R.E., and Schwartz, A.B. (1988). Primate motor cortex and free arm movements to visual targets in three- dimensional space. II. Coding of the direction of movement by a neuronal population. J. Neurosci. *8*, 2928–2937.

Georgopoulos, A.P., Merchant, H., Naselaris, T., and Amirikian, B. (2007). Mapping of the preferred direction in the motor cortex. Proc. Natl. Acad. Sci. *104*, 11068–11072.

Graham, D., and Field, D. (2007). Sparse Coding in the Neocortex. Evol. Nerv. Syst. *3*.

Graimann, B., Allison, B., and Pfurtscheller, G. (2009). Brain–Computer Interfaces: A Gentle Introduction. In Brain-Computer Interfaces, (Springer, Berlin, Heidelberg), pp. 1–27.

Graziano, M. (2006). The Organization of Behavioral Repertoire in Motor Cortex. Annu. Rev. Neurosci. *29*, 105–134.

Gremel, C.M., and Costa, R.M. (2013). Orbitofrontal and striatal circuits dynamically encode the shift between goal-directed and habitual actions. Nat. Commun. *4*, 2264.

Grienberger, C., and Konnerth, A. (2012). Imaging Calcium in Neurons. Neuron *73*, 862–885.

Gu, Z., Kalambogias, J., Yoshioka, S., Han, W., Li, Z., Kawasawa, Y.I., Pochareddy, S., Li, Z., Liu, F., Xu, X., et al. (2017). Control of species-dependent cortico-motoneuronal connections underlying manual dexterity. Science *357*, 400–404.

Guo, J.-Z., Graves, A.R., Guo, W.W., Zheng, J., Lee, A., Rodríguez-González, J., Li, N., Macklin, J.J., Phillips, J.W., Mensh, B.D., et al. (2015). Cortex commands the performance of skilled movement. ELife *4*, e10774.

Guo, Z.V., Hires, S.A., Li, N., O'Connor, D.H., Komiyama, T., Ophir, E., Huber, D., Bonardi, C., Morandell, K., Gutnisky, D., et al. (2014). Procedures for Behavioral Experiments in Head-Fixed Mice. PLoS ONE *9*, e88678.

Gusel'nikova, V.V., and Korzhevskiy, D.E. (2015). NeuN As a Neuronal Nuclear Antigen and Neuron Differentiation Marker. Acta Naturae *7*, 42–47.

Hallett, M. (2001). Plasticity of the human motor cortex and recovery from stroke. Brain Res. Rev. *36*, 169–174.

Hansel, D., and van Vreeswijk, C. (2012). The mechanism of orientation selectivity in primary visual cortex without a functional map. J. Neurosci. Off. J. Soc. Neurosci. *32*, 4049–4064.

Hara-Kuge, S., Nishihara, T., Matsuda, T., Kitazono, T., Teramoto, T., Nagai, T., and Ishihara, T. (2018). An improved inverse-type Ca2+ indicator can detect putative neuronal inhibition in Caenorhabditis elegans by increasing signal intensity upon Ca2+ decrease. PLOS ONE *13*, e0194707.

Harrison, T.C., Ayling, O.G.S., and Murphy, T.H. (2012). Distinct Cortical Circuit Mechanisms for Complex Forelimb Movement and Motor Map Topography. Neuron *74*, 397–409.

Hatsopoulos, N.G., and Suminski, A.J. (2011). Sensing with the Motor Cortex. Neuron *72*, 477–487.

Hattox, A.M., and Nelson, S.B. (2007). Layer V Neurons in Mouse Cortex Projecting to Different Targets Have Distinct Physiological Properties. J. Neurophysiol. *98*, 3330–3340.

Hay, E., Hill, S., Schürmann, F., Markram, H., and Segev, I. (2011). Models of Neocortical Layer 5b Pyramidal Cells Capturing a Wide Range of Dendritic and Perisomatic Active Properties. PLOS Comput. Biol. *7*, e1002107.

Henze, D.A., Borhegyi, Z., Csicsvari, J., Mamiya, A., Harris, K.D., and Buzsáki, G. (2000). Intracellular features predicted by extracellular recordings in the hippocampus in vivo. J. Neurophysiol. *84*, 390–400.

Herculano-Houzel, S., Watson, C., and Paxinos, G. (2013). Distribution of neurons in functional areas of the mouse cerebral cortex reveals quantitatively different cortical zones. Front. Neuroanat. *7*.

Hira, R., Ohkubo, F., Ozawa, K., Isomura, Y., Kitamura, K., Kano, M., Kasai, H., and Matsuzaki, M. (2013a). Spatiotemporal Dynamics of Functional Clusters of Neurons in the Mouse Motor Cortex during a Voluntary Movement. J. Neurosci. *33*, 1377–1390.

Hira, R., Ohkubo, F., Tanaka, Y.R., Masamizu, Y., Augustine, G.J., Kasai, H., and Matsuzaki, M. (2013b). In vivo optogenetic tracing of functional corticocortical connections between motor forelimb areas. Front. Neural Circuits *7*.

Hira, R., Terada, S.-I., Kondo, M., and Matsuzaki, M. (2015). Distinct Functional Modules for Discrete and Rhythmic Forelimb Movements in the Mouse Motor Cortex. J. Neurosci. *35*, 13311–13322.

Hluštík, P., Solodkin, A., Gullapalli, R.P., Noll, D.C., and Small, S.L. (2001). Somatotopy in Human Primary Motor and Somatosensory Hand Representations Revisited. Cereb. Cortex *11*, 312–321.

Holscher, C., and Munk, M. (2008). Information Processing by Neuronal Populations (Cambridge University Press).

Holt, G.R., Softky, W.R., Koch, C., and Douglas, R.J. (1996). Comparison of discharge variability in vitro and in vivo in cat visual cortex neurons. J. Neurophysiol. *75*, 1806–1814.

Hooks, B.M., Hires, S.A., Zhang, Y.-X., Huber, D., Petreanu, L., Svoboda, K., and Shepherd, G.M.G. (2011). Laminar Analysis of Excitatory Local Circuits in Vibrissal Motor and Sensory Cortical Areas. PLoS Biol. *9*.

Hooks, B.M., Mao, T., Gutnisky, D.A., Yamawaki, N., Svoboda, K., and Shepherd, G.M.G. (2013). Organization of cortical and thalamic input to pyramidal neurons in mouse motor cortex. J. Neurosci. Off. J. Soc. Neurosci. *33*, 748–760.

Hopfield, J.J. (1995). Pattern recognition computation using action potential timing for stimulus representation. Nature *376*, 33–36.

Hubel, D.H., and Wiesel, T.N. (1959). Receptive fields of single neurones in the cat's striate cortex. J. Physiol. *148*, 574–591.

Hubel, D.H., and Wiesel, T.N. (1963). Shape and arrangement of columns in cat's striate cortex. J. Physiol. *165*, 559-568.2.

Huber, D., Gutnisky, D.A., Peron, S., O'Connor, D.H., Wiegert, J.S., Tian, L., Oertner, T.G., Looger, L.L., and Svoboda, K. (2012). Multiple dynamic representations in the motor cortex during sensorimotor learning. Nature *484*, 473–478.

Humby, T., and Wilkinson, L. (2006). If Only They Could Talk. In Transgenic and Knockout Models of Neuropsychiatric Disorders, (Humana Press), pp. 69–83.

Hussar, C., and Pasternak, T. (2010). Trial-to-trial variability of the prefrontal neurons reveals the nature of their engagement in a motion discrimination task. Proc. Natl. Acad. Sci. U. S. A. *107*, 21842–21847.

Isomura, Y., Harukuni, R., Takekawa, T., Aizawa, H., and Fukai, T. (2009). Microcircuitry coordination of cortical motor information in self-initiation of voluntary movements. Nat. Neurosci. *12*, 1586–1593.

Jelitai, M., Puggioni, P., Ishikawa, T., Rinaldi, A., and Duguid, I. (2016). Dendritic excitation–inhibition balance shapes cerebellar output during motor behaviour. Nat. Commun. *7*, 13722.

Kaas, J.H. (2004). Evolution of somatosensory and motor cortex in primates. Anat. Rec. A. Discov. Mol. Cell. Evol. Biol. *281A*, 1148–1156.

Kaifosh, P., Zaremba, J.D., Danielson, N.B., and Losonczy, A. (2014). SIMA: Python software for analysis of dynamic fluorescence imaging data. Front. Neuroinformatics *8*.

Kakei, S., Hoffman, D.S., and Strick, P.L. (1999). Muscle and Movement Representations in the Primary Motor Cortex. Science *285*, 2136–2139.

Kandel, E.R., and Tauc, L. (1965). Heterosynaptic facilitation in neurones of the abdominal ganglion of Aplysia depilans. J. Physiol. *181*, 1–27.

Kang, Y. (1995). Differential paired pulse depression of non-NMDA and NMDA currents in pyramidal cells of the rat frontal cortex. J. Neurosci. *15*, 8268–8280.

Kapoor, V., Krampe, E., Klug, A., Logothetis, N.K., and Panagiotaropoulos, T.I. (2013). Development of tube tetrodes and a multi-tetrode drive for deep structure electrophysiological recordings in the macaque brain. J. Neurosci. Methods *216*, 43–48.

Karl, J.M., and Whishaw, I.Q. (2011). Rodent Skilled Reaching for Modeling Pathological Conditions of the Human Motor System. In Animal Models of Movement Disorders, (Humana Press), pp. 87–107.

Katz, L.C., Burkhalter, A., and Dreyer, W.J. (1984). Fluorescent latex microspheres as a retrograde neuronal marker for in vivo and in vitro studies of visual cortex. Nature *310*, 498.

Kawai, R., Markman, T., Poddar, R., Ko, R., Fantana, A.L., Dhawale, A.K., Kampff, A.R., and Ölveczky, B.P. (2015). Motor Cortex Is Required for Learning but Not for Executing a Motor Skill. Neuron *86*, 800–812.

Keemink, S.W., Lowe, S.C., Pakan, J.M.P., Dylda, E., van Rossum, M.C.W., and Rochefort, N.L. (2018). FISSA: A neuropil decontamination toolbox for calcium imaging signals. Sci. Rep. *8*, 3493.

Kim, T.H., Zhang, Y., Lecoq, J., Jung, J.C., Li, J., Zeng, H., Niell, C.M., and Schnitzer, M.J. (2016). Long-Term Optical Access to an Estimated One Million Neurons in the Live Mouse Cortex. Cell Rep. *17*, 3385–3394.

King, C.E., Wang, P.T., McCrimmon, C.M., Chou, C.C., Do, A.H., and Nenadic, Z. (2015). The feasibility of a brain-computer interface functional electrical stimulation system for the restoration of overground walking after paraplegia. J. NeuroEngineering Rehabil. *12*, 80.

Knierim, J.J. (2014). Chapter 19 - Information Processing in Neural Networks. In From Molecules to Networks (Third Edition), (Boston: Academic Press), pp. 563–589.

Ko, K.H. (2016). Origins of human intelligence: The chain of tool-making and brain evolution. Anthropol. Noteb. *22*, 5–22.

Kobat, D., Durst, M.E., Nishimura, N., Wong, A.W., Schaffer, C.B., and Xu, C. (2009). Deep tissue multiphoton microscopy using longer wavelength excitation. Opt. Express *17*, 13354–13364.

Krubitzer, L., and Dooley, J.C. (2013). Cortical plasticity within and across lifetimes: how can development inform us about phenotypic transformations? Front. Hum. Neurosci. *7*, 620.

Kwan, A.C. (2008). What can population calcium imaging tell us about neural circuits? J. Neurophysiol. *100*, 2977–2980.

Lance, B.J., Kerick, S.E., Ries, A.J., Oie, K.S., and McDowell, K. (2012). Brain-Computer Interface Technologies in the Coming Decades. Proc. IEEE *100*, 1585–1599.

Lashley, K.S. (1924). Studies of Cerebral Function in Learning (VI). Psychol. Rev. *31*, 369–375.

Lawrence, D.G., and Kuypers, H.G.J.M. (1968). THE FUNCTIONAL ORGANIZATION OF THE MOTOR SYSTEM IN THE MONKEYI. THE EFFECTS OF BILATERAL PYRAMIDAL LESIONS. Brain *91*, 1–14.

LeCun, Y., Bengio, Y., and Hinton, G. (2015). Deep learning. Nature *521*, 436–444.

Levi, R., and Camhi, J.M. (2000). Population Vector Coding by the Giant Interneurons of the Cockroach. J. Neurosci. *20*, 3822–3829.

Lewis, J.E., and Jr, W.B.K. (1998). A neuronal network for computing population vectors in the leech. Nature *391*, 76–79.

Li, N., Chen, T.-W., Guo, Z.V., Gerfen, C.R., and Svoboda, K. (2015). A motor cortex circuit for motor planning and movement. Nature *advance online publication*.

Li, Q., Ko, H., Qian, Z.-M., Yan, L.Y.C., Chan, D.C.W., Arbuthnott, G., Ke, Y., and Yung, W.-H. (2017). Refinement of learned skilled movement representation in motor cortex deep output layer. Nat. Commun. *8*, 15834.

Lillicrap, T.P., and Scott, S.H. (2013). Preference Distributions of Primary Motor Cortex Neurons Reflect Control Solutions Optimized for Limb Biomechanics. Neuron *77*, 168–179.

Linden, S. (2003). The Alchemy Reader: From Hermes Trismegistus to Isaac Newton (Cambridge: Cambridge University Press).

Lock, J.T., Parker, I., and Smith, I.F. (2015). A comparison of fluorescent Ca2+ indicators for imaging local Ca2+ signals in cultured cells. Cell Calcium *58*, 638–648.

Lorenz, K. (1961). King Solomon's ring: new light on animal ways (New York: Crowell).

Macleod, G.T. (2012). Imaging and Analysis of Nonratiometric Calcium Indicators at the Drosophila Larval Neuromuscular Junction. Cold Spring Harb. Protoc. *2012*, pdb.prot070110.

Makino, H., Ren, C., Liu, H., Kim, A.N., Kondapaneni, N., Liu, X., Kuzum, D., and Komiyama, T. (2017). Transformation of Cortex-wide Emergent Properties during Motor Learning. Neuron *94*, 880-890.e8.

Malkki, H.A.I., Donga, L.A.B., Groot, D., E, S., Battaglia, F.P., and Pennartz, C.M. (2010). Appetitive operant conditioning in mice: heritability and dissociability of training stages. Front. Behav. Neurosci. *4*.

Marblestone, A.H., Wayne, G., and Kording, K.P. (2016). Toward an Integration of Deep Learning and Neuroscience. Front. Comput. Neurosci. *10*.

Masamizu, Y., Tanaka, Y.R., Tanaka, Y.H., Hira, R., Ohkubo, F., Kitamura, K., Isomura, Y., Okada, T., and Matsuzaki, M. (2014). Two distinct layer-specific dynamics of cortical ensembles during learning of a motor task. Nat. Neurosci. *17*, 987–994.

Mehring, C., Nawrot, M.P., de Oliveira, S.C., Vaadia, E., Schulze-Bonhage, A., Aertsen, A., and Ball, T. (2004). Comparing information about arm movement direction in single channels of local and epicortical field potentials from monkey and human motor cortex. J. Physiol.-Paris *98*, 498–506.

Mendoza-Halliday, D., and Martinez-Trujillo, J.C. (2017). Neuronal population coding of perceived and memorized visual features in the lateral prefrontal cortex. Nat. Commun. *8*, 15471.

Meyers, E. (2013). The neural decoding toolbox. Front. Neuroinformatics *7*.

Mitsuda, T., and Onorati, P. (2002). Three-dimensional tuning profile of motor cortical activity during arm movements. Neuroreport *13*, 1477–1480.

Mittmann, W., Wallace, D.J., Czubayko, U., Herb, J.T., Schaefer, A.T., Looger, L.L., Denk, W., and Kerr, J.N.D. (2011). Two-photon calcium imaging of evoked activity from L5 somatosensory neurons in vivo. Nat. Neurosci. *14*, 1089–1093.

Miyawaki, A., Llopis, J., Heim, R., McCaffery, J.M., Adams, J.A., Ikura, M., and Tsien, R.Y. (1997). Fluorescent indicators for Ca2+based on green fluorescent proteins and calmodulin. Nature *388*, 882–887.

Möller, C., Lücke, J., Zhu, J., Faustmann, P.M., and von der Malsburg, C. (2007). Glial cells for information routing? Cogn. Syst. Res. *8*, 28–35.

Montijn, J.S., Goltstein, P.M., and Pennartz, C.M. (2015). Mouse V1 population correlates of visual detection rely on heterogeneity within neuronal response patterns.

Morandell, K., and Huber, D. (2017). The role of forelimb motor cortex areas in goal directed action in mice. Sci. Rep. *7*, 15759.

Morgan, T.J.H., Uomini, N.T., Rendell, L.E., Chouinard-Thuly, L., Street, S.E., Lewis, H.M., Cross, C.P., Evans, C., Kearney, R., Torre, I. de la, et al. (2015). Experimental evidence for the co-evolution of hominin tool-making teaching and language. Nat. Commun. *6*, 6029.

Moroz, L.L. (2011). Aplysia. Curr. Biol. CB *21*, R60–R61.

Mullen, R.J., Buck, C.R., and Smith, A.M. (1992). NeuN, a neuronal specific nuclear protein in vertebrates. Development *116*, 201–211.

Murty, M.N., Shevade, S.K., Asharaf, S., Murty, M.N., Shevade, S.K., and Asharaf, S. (2006). Scalable non-linear Support Vector Machine using hierarchical clustering. In 18th International Conference on Pattern Recognition (ICPR'06), pp. 908–911.

Nam, S., and Kim, D.-S. (2017). Reconstruction of Arm Movement Directions from Human Motor Cortex Using fMRI. Front. Neurosci. *11*.

Naselaris, T., Merchant, H., Amirikian, B., and Georgopoulos, A.P. (2006). Large-Scale Organization of Preferred Directions in the Motor Cortex. I. Motor Cortical Hyperacuity for Forward Reaching. J. Neurophysiol. *96*, 3231–3236.

Neumann, M., Wang, Y., Kim, S., Hong, S.M., Bilgen, M., and Liu, J. (2009). Assessing gait impairment following experimental traumatic brain injury in mice. J. Neurosci. Methods *176*, 34–44.

Nicolas-Alonso, L.F., and Gomez-Gil, J. (2012). Brain Computer Interfaces, a Review. Sensors *12*, 1211–1279.

Niell, C.M., and Stryker, M.P. (2008). Highly Selective Receptive Fields in Mouse Visual Cortex. J. Neurosci. *28*, 7520–7536.

Nudo, R.J. (2013). Recovery after brain injury: mechanisms and principles. Front. Hum. Neurosci. *7*.

Nudo, R.J., Milliken, G.W., Jenkins, W.M., and Merzenich, M.M. (1996). Use-dependent alterations of movement representations in primary motor cortex of adult squirrel monkeys. J. Neurosci. *16*, 785–807.

Oby, E.R., Ethier, C., and Miller, L.E. (2012). Movement representation in the primary motor cortex and its contribution to generalizable EMG predictions. J. Neurophysiol. *109*, 666–678.

Ogden, R., and Franz, S.I. (1917). On cerebral motor control: The recovery from experimentally produced hemiplegia. Psychobiology *1*, 33–49.

Oheim, M., Beaurepaire, E., Chaigneau, E., Mertz, J., and Charpak, S. (2001). Two-photon microscopy in brain tissue: parameters influencing the imaging depth. J. Neurosci. Methods *111*, 29–37.

Ohki, K., and Reid, R.C. (2007). Specificity and randomness in the visual cortex. Curr. Opin. Neurobiol. *17*, 401–407.

Ohki, K., Chung, S., Ch'ng, Y.H., Kara, P., and Reid, R.C. (2005). Functional imaging with cellular resolution reveals precise micro-architecture in visual cortex. Nature *433*, 597–603.

Oswald, M.J., Tantirigama, M.L.S., Sonntag, I., Hughes, S.M., and Empson, R.M. (2013). Diversity of layer 5 projection neurons in the mouse motor cortex. Front. Cell. Neurosci. *7*.

Otchy, T.M., Wolff, S.B.E., Rhee, J.Y., Pehlevan, C., Kawai, R., Kempf, A., Gobes, S.M.H., and Ölveczky, B.P. (2015). Acute off-target effects of neural circuit manipulations. Nature *528*, 358–363.

Otsuka, T., and Kawaguchi, Y. (2009). Cortical Inhibitory Cell Types Differentially Form Intralaminar and Interlaminar Subnetworks withExcitatory Neurons. J. Neurosci. *29*, 10533–10540.

Otten, E. (2001). The Motor System: The Whole and its Parts. Neural Plast. *8*, 111–119.

Panzeri, S., Macke, J.H., Gross, J., and Kayser, C. (2015). Neural population coding: combining insights from microscopic and mass signals. Trends Cogn. Sci. *19*, 162–172.

Park, K., You, J., Du, C., and Pan, Y. (2015). Cranial window implantation on mouse cortex to study microvascular change induced by cocaine. Quant. Imaging Med. Surg. *5*, 97–107.

Passini, M.A., Watson, D.J., and Wolfe, J.H. (2004). Gene Delivery to the Mouse Brain with Adeno-Associated Virus. In Gene Delivery to Mammalian Cells, (Humana Press), pp. 225–236.

Paxinos, G., and Franklin, K. (2001). The Mouse Brain in Stereotaxic Coordinates - 2nd Edition (San Diego: Academic Press).

Penfield, W., and Boldrey, E. (1937). SOMATIC MOTOR AND SENSORY REPRESENTATION IN THE CEREBRAL CORTEX OF MAN AS STUDIED BY ELECTRICAL STIMULATION. Brain *60*, 389–443.

Peters, A.J., Chen, S.X., and Komiyama, T. (2014). Emergence of reproducible spatiotemporal activity during motor learning. Nature *510*, 263–267.

Petersen, C.C.H., and Crochet, S. (2013). Synaptic Computation and Sensory Processing in Neocortical Layer 2/3. Neuron *78*, 28–48.

Plautz, E.J., Milliken, G.W., and Nudo, R.J. (2000). Effects of Repetitive Motor Training on Movement Representations in Adult Squirrel Monkeys: Role of Use versus Learning. Neurobiol. Learn. Mem. *74*, 27–55.

Poulet, J.F.A., and Petersen, C.C.H. (2008). Internal brain state regulates membrane potential synchrony in barrel cortex of behaving mice. Nature *454*, 881–885.

Puggioni, P. (2015). Input-output Transformations in the Awake Mouse Brain using Whole-cell Recordings and Probabilistic Analysis. Doctoral thesis. University of Edinburgh.

Quian Quiroga, R., and Panzeri, S. (2009). Extracting information from neuronal populations: information theory and decoding approaches. Nat. Rev. Neurosci. *10*, 173–185.

Rabl, R., Horvath, A., Breitschaedel, C., Flunkert, S., Roemer, H., and Hutter-Paier, B. (2016). Quantitative evaluation of orofacial motor function in mice: The pasta gnawing test, a voluntary and stress-free behavior test. J. Neurosci. Methods *274*, 125–130.

Rathelot, J.-A., and Strick, P.L. (2009). Subdivisions of primary motor cortex based on cortico-motoneuronal cells. Proc. Natl. Acad. Sci. *106*, 918–923.

Ray, A.M., Sitaram, R., Rana, M., Pasqualotto, E., Buyukturkoglu, K., Guan, C., Ang, K.-K., Tejos, C., Zamorano, F., Aboitiz, F., et al. (2015). A subject-independent pattern-based Brain-Computer Interface. Front. Behav. Neurosci. *9*, 269.

Reep, R.L., Goodwin, G.S., and Corwin, J.V. (1990). Topographic organization in the corticocortical connections of medial agranular cortex in rats. J. Comp. Neurol. *294*, 262–280.

Rioult-Pedotti, M.-S., Friedman, D., Hess, G., and Donoghue, J.P. (1998). Strengthening of horizontal cortical connections following skill learning. Nat. Neurosci. *1*, 230–234.

Rivara, C.-B., Sherwood, C.C., Bouras, C., and Hof, P.R. (2003). Stereologic characterization and spatial distribution patterns of Betz cells in the human primary motor cortex. Anat. Rec. A. Discov. Mol. Cell. Evol. Biol. *270A*, 137–151.

Robinson, D.A. (1968). The electrical properties of metal microelectrodes. Proc. IEEE *56*, 1065–1071.

Rodriguez, J.D., Perez, A., and Lozano, J.A. (2010). Sensitivity Analysis of k-Fold Cross Validation in Prediction Error Estimation. IEEE Trans. Pattern Anal. Mach. Intell. *32*, 569–575.

Rossi, M.A., and Yin, H.H. (2012). Methods for studying habitual behavior in mice. Curr. Protoc. Neurosci. Editor. Board Jacqueline N Crawley Al *CHAPTER*, Unit8.29.

Saiki, A., Kimura, R., Samura, T., Fujiwara-Tsukamoto, Y., Sakai, Y., and Isomura, Y. (2014). Different Modulation of Common Motor Information in Rat Primary and Secondary Motor Cortices. PLOS ONE *9*, e98662.

Salganik, M., Hirsch, M.L., and Samulski, R.J. (2015). Adeno-associated Virus as a Mammalian DNA Vector. Microbiol. Spectr. *3*.

Salinas, E. (2006). Noisy neurons can certainly compute. Nat. Neurosci. *9*, 1349–1350.

Sanger, T.D. (1994). Theoretical Considerations for the Analysis of Population Coding in Motor Cortex. Neural Comput. *6*, 29–37.

Scaglione, A., Moxon, K.A., Aguilar, J., and Foffani, G. (2011). Trial-to-trial variability in the responses of neurons carries information about stimulus location in the rat whisker thalamus. Proc. Natl. Acad. Sci. U. S. A. *108*, 14956–14961.

Schendel, A.A., Thongpang, S., Brodnick, S.K., Richner, T.J., Lindevig, B.D.B., Krugner-Higby, L., and Williams, J.C. (2013). A cranial window imaging method for monitoring vascular growth around chronically implanted micro-ECoG devices. J. Neurosci. Methods *218*.

Schiemann, J., Puggioni, P., Dacre, J., Pelko, M., Domanski, A., van Rossum, M.C.W., and Duguid, I. (2015). Cellular Mechanisms Underlying Behavioral State-Dependent Bidirectional Modulation of Motor Cortex Output. Cell Rep. *11*, 1319–1330.

Schoch, S., Cibelli, G., and Thiel, G. (1996). Neuron-specific Gene Expression of Synapsin I MAJOR ROLE OF A NEGATIVE REGULATORY MECHANISM. J. Biol. Chem. *271*, 3317–3323.

Schofield, B.R. (2001). Retrograde Axonal Tracing with Fluorescent Markers. In Current Protocols in Neuroscience, (John Wiley & Sons, Inc.), p.

Schüz, A., and Palm, G. (1989). Density of neurons and synapses in the cerebral cortex of the mouse. J. Comp. Neurol. *286*, 442–455.

Schwartz, A.B. (1994). Direct Cortical Representation of Drawing. Science *265*, 540–542.

Schwarz, C., Hentschke, H., Butovas, S., Haiss, F., Stüttgen, M.C., Gerdjikov, T.V., Bergner, C.G., and Waiblinger, C. (2010). The head-fixed behaving rat—Procedures and pitfalls. Somatosens. Mot. Res. *27*, 131–148.

Scott, S.H. (2000). Population vectors and motor cortex: neural coding or epiphenomenon? Nat. Neurosci. *3*, 307–308.

Shepherd, G.M.G. (2009). Intracortical cartography in an agranular area. Front. Neurosci. *3*.

Shepherd, G.M.G. (2013). Corticostriatal connectivity and its role in disease. Nat. Rev. Neurosci. *14*, 278–291.

Shepherd, G.M.G. (2014). Diversity and complexity in the pyramidal tract projectome. Nat. Rev. Neurosci. *15*, 63–63.

Shepherd, G.M., and Rowe, T.B. (2017). Neocortical Lamination: Insights from Neuron Types and Evolutionary Precursors. Front. Neuroanat. *11*.

Sherrington, C. (1949). Man and His Nature: Broadcast Talks in Religion and Philosophy (CUP Archive).

Sherrington, S.C.S. (1906). The Integrative action of the nervous system (Yale University Press).

Sherwood, C.C., Lee, P.W.H., Rivara, C.-B., Holloway, R.L., Gilissen, E.P.E., Simmons, R.M.T., Hakeem, A., Allman, J.M., Erwin, J.M., and Hof, P.R. (2003). Evolution of Specialized Pyramidal Neurons in Primate Visual and Motor Cortex. Brain. Behav. Evol. *61*, 28–44.

Shoham, S., O'Connor, D.H., and Segev, R. (2006). How silent is the brain: is there a "dark matter" problem in neuroscience? J. Comp. Physiol. A *192*, 777–784.

Skinner, B.F. (1951). How to teach animals. Sci. Am. *185*, 26–29.

Skottun, B.C., De Valois, R.L., Grosof, D.H., Movshon, J.A., Albrecht, D.G., and Bonds, A.B. (1991). Classifying simple and complex cells on the basis of response modulation. Vision Res. *31*, 1078–1086.

Slotnick, B. (2009). A simple 2-transistor touch or lick detector circuit. J. Exp. Anal. Behav. *91*, 253–255.

Spanne, A., and Jörntell, H. (2015). Questioning the role of sparse coding in the brain. Trends Neurosci. *38*, 417–427.

Steinmetz, N.A., Koch, C., Harris, K.D., and Carandini, M. (2018). Challenges and opportunities for large-scale electrophysiology with Neuropixels probes. Curr. Opin. Neurobiol. *50*, 92–100.

Stroemer, R.P., Kent, T.A., and Hulsebosch, C.E. (1995). Neocortical Neural Sprouting, Synaptogenesis, and Behavioral Recovery After Neocortical Infarction in Rats. Stroke *26*, 2135–2144.

Svoboda, K., Denk, W., Kleinfeld, D., and Tank, D.W. (1997). In vivo dendritic calcium dynamics in neocortical pyramidal neurons. Nature *385*, 161–165.

Takase, H., Kurihara, Y., Yokoyama, T., Kawahara, N., and Takei, K. (2017). LOTUS overexpression accelerates neuronal plasticity after focal brain ischemia in mice. PLoS ONE *12*.

Tam, D.C. (2003). Real-time estimation of predictive firing rate. Neurocomputing *52–54*, 637–641.

Taylor, D.M., Tillery, S.I.H., and Schwartz, A.B. (2002). Direct Cortical Control of 3D Neuroprosthetic Devices. Science *296*, 1829–1832.

Tennant, K.A., Adkins, D.L., Donlan, N.A., Asay, A.L., Thomas, N., Kleim, J.A., and Jones, T.A. (2011). The Organization of the Forelimb Representation of the C57BL/6 Mouse Motor Cortex as Defined by Intracortical Microstimulation and Cytoarchitecture. Cereb. Cortex *21*, 865–876.

Theer, P., and Denk, W. (2006). On the fundamental imaging-depth limit in two-photon microscopy. JOSA A *23*, 3139–3149.

Tolhurst, D.J., Smyth, D., and Thompson, I.D. (2009). The Sparseness of Neuronal Responses in Ferret Primary Visual Cortex. J. Neurosci. *29*, 2355–2370.

Toxopeus, C.M., Jong, B.M. de, Valsan, G., Conway, B.A., Leenders, K.L., and Maurits, N.M. (2011). Direction of Movement Is Encoded in the Human Primary Motor Cortex. PLOS ONE *6*, e27838.

Tucci, V., Hardy, A., and Nolan, P.M. (2006). A comparison of physiological and behavioural parameters in C57BL/6J mice undergoing food or water restriction regimes. Behav. Brain Res. *173*, 22–29.

Vandamme, T.F. (2014). Use of rodents as models of human diseases. J. Pharm. Bioallied Sci. *6*, 2–9.

Vapnik, V.N. (1999). An overview of statistical learning theory. IEEE Trans. Neural Netw. *10*, 988–999.

Walker, T. (2014). Cell Magic Wand. Retrieved from https://www.maxplanckflorida.org/fitzpatricklab/softwarecell/MagicWand.

Wang, L., Conner, J.M., Rickert, J., and Tuszynski, M.H. (2011). Structural plasticity within highly specific neuronal populations identifies a unique parcellation of motor learning in the adult brain. Proc. Natl. Acad. Sci. *108*, 2545–2550.

Wang, X., Zhang, C., Szábo, G., and Sun, Q.-Q. (2013). Distribution of CaMKIIα expression in the brain in vivo, studied by CaMKIIα-GFP mice. Brain Res. *1518*, 9–25.

Wang, X., Liu, Y., Li, X., Zhang, Z., Yang, H., Zhang, Y., Williams, P.R., Alwahab, N.S.A., Kapur, K., Yu, B., et al. (2017). Deconstruction of Corticospinal Circuits for Goal-Directed Motor Skills. Cell *171*, 440-455.e14.

Ward, R.D., Winiger, V., Kandel, E.R., Balsam, P.D., and Simpson, E.H. (2015). Orbitofrontal cortex mediates the differential impact of signaled-reward probability on discrimination accuracy. Front. Neurosci. *9*.

Watson, C., and Harrison, M. (2012). The Location of the Major Ascending and Descending Spinal Cord Tracts in all Spinal Cord Segments in the Mouse: Actual and Extrapolated. Anat. Rec. *295*, 1692–1697.

Watson, C., Paxinos, G., and Puelles, L. (2012). The mouse nervous system (Amsterdam ; Boston: Elsevier Academic Press).

Watson, S.S., Riordan, T.J., Pryce, B.A., and Schweitzer, R. (2009). The Tendons and Muscles of the Mouse Forelimb during Embryonic Development. Dev. Dyn. Off. Publ. Am. Assoc. Anat. *238*, 693–700.

Weiler, N., Wood, L., Yu, J., Solla, S.A., and Shepherd, G.M.G. (2008). Top-down laminar organization of the excitatory network in motor cortex. Nat. Neurosci. *11*, 360–366.

Willmore, B., and Tolhurst, D.J. (2001). Characterizing the sparseness of neural codes. Netw. Bristol Engl. *12*, 255–270.

Yacoub, E., Harel, N., and Uğurbil, K. (2008). High-field fMRI unveils orientation columns in humans. Proc. Natl. Acad. Sci. *105*, 10607–10612.

Yamawaki, N., Borges, K., Suter, B.A., Harris, K.D., and Shepherd, G.M.G. (2014). A genuine layer 4 in motor cortex with prototypical synaptic circuit connectivity.

Young, M.P., and Yamane, S. (1992). Sparse Population Coding of Faces in the Inferotemporal Cortex. Science *256*, 1327–1331.

Yu, J., Anderson, C.T., Kiritani, T., Sheets, P.L., Wokosin, D.L., Wood, L., and Shepherd, G.M.G. (2008). Local-Circuit Phenotypes of Layer 5 Neurons in Motor-Frontal Cortex of YFP-H Mice. Front. Neural Circuits *2*.

Zimmermann, K.S., Yamin, J.A., Rainnie, D.G., Ressler, K.J., and Gourley, S.L. (2017). Connections of the Mouse Orbitofrontal Cortex and Regulation of Goal-Directed Action Selection by Brain-Derived Neurotrophic Factor. Biol. Psychiatry *81*, 366–377.